OUKA
The University of Osaka
Institutional Knowledge Archive

Title	Computational fluid dynamics study on ship maneuvering in calm water and waves
Author(s)	Roychoudhury, Seemontini
Citation	大阪大学, 2021, 博士論文
Version Type	VoR
URL	https://doi.org/10.18910/85408
rights	
Note	

The University of Osaka Institutional Knowledge Archive : OUKA

https://ir.library.osaka-u.ac.jp/

The University of Osaka

Doctoral Dissertation

Computational fluid dynamics study on ship maneuvering in calm water and waves

(数値流体力学を用いた平水中および波浪中の船舶操縦性に関する研究)

RoyChoudhury Seemontini

June 2021

Department of Naval Architecture and Ocean Engineering
Division of Global Architecture
Graduate School of Engineering
Osaka University, Japan

ACKNOWLEDGEMENTS

I express my sincere gratitude to my supervisor Professor Yasuyuki Toda for accepting me as a Ph.D. student at his laboratory. I am thankful to him to have introduced me to the community of naval research. He has been a wonderful mentor to me during my tenure in this esteemed institution. The valuable advices and technical inputs obtained from him during this period have been clinical in the successful completion of the thesis.

I gratefully acknowledge Assistant Professor Ping-Chen Wu of National Cheng Kung University for his help, support, and advice from the beginning of this work. His regular counsel, during his stay at Toda Laboratory, has helped me understand the computational methods from the very early stages of this research.

I address special thanks to Dr. Yugo Sanada and Professor Frederick Stern at IIHR-Hydroscience & Engineering, University of Iowa, for their precious contributions in experiments and computational support for the successful completion of this study. I am lucky and honoured to have worked with them.

I address special thanks to Kodai Kawamoto, a former member of Toda Laboratory for his precious contributions to the completion of the thesis. I am grateful for his sincere efforts in helping me complete the thesis.

I would like to express my gratitude to all members of the Toda laboratory for their constant assistance and kind help.

I express my deep gratitude to the Ministry of Education, Culture, Sports, Science and Technology, Japan (MEXT) for supporting me with the scholarship that enabled me to study in content.

Of utmost importance, I am indebted to my parents, Mr. Dipak RoyChoudhury and Mrs. Meera Roy Choudhury for their patience, love, and unconditional encouragement to pursue my goal. I would also like to express my gratitude towards Dr. Manjakavahoaka Razanoelina, who has been a constant support for me in Japan. Last but certainly not least, I would like to thank all of my friends, in India and Japan, for all their support and presence.

ABSTRACT

Over the years, dependable estimates of maneuvering performance have been obtained using mathematical model for equations of motion and model testing to get the hydrodynamic force coefficient but are costly, time-consuming and the flow field to understand the propeller-hull-rudder interaction is rarely measured. Alternatively, Computational fluid dynamics (CFD) provides answers to the pitfalls of model testing but it has its challenges. One of the major factors affecting the accuracy of computational studies of ship hydrodynamics is the propeller modelling. Several researches have focused on using fully discretized propeller modelling for maneuvering simulations. However, it requires elaborate modelling and is computationally exhaustive especially in maneuvering studies. Alternatively, a body force propeller model capable of capturing the hull-propeller-rudder interaction efficiently is advantageous. In this study, we propose an approach of using Unsteady Reynolds Averaged Navier Stokes (RANS) solver coupled with the Osaka University (OU) propeller model for Korean Research Institute for Ships and Ocean Engineering (KRISO) Container Ship (KCS) free maneuvering studies. The model uses the total inflow velocity at the propeller plane thus eliminating the need of assuming the direction and path of the free vortex, critical to maneuvering simulations. The model is thus efficient in unsteady/asymmetric flow. This is one of the first attempts to use the RANS solver coupled with the OU body force propeller model in free-running 6 Degrees of Freedom (DOF) simulations simulations with moving rudder. The time-series results of self-propulsion, zigzag maneuvers, and turning circle maneuvers were validated against experimental data of Iowa Institute of Hydraulic Research (IIHR), The University of Iowa for motions, neutral rudder angle and propeller performance data. The test conditions for both computations and experiments were maintained same as the Tokyo 2015: A Workshop on CFD in Ship Hydrodynamics. The results were also compared against other propeller models to understand its effectiveness. The study was further extended to studying course-keeping ability of KCS in waves (λ/L=0.65, 1.00, 1.15, and 1.37). Fourier series analysis was conducted for unsteady time series in wave conditions and compared with data from various institutes to ensure reliable prediction. Additionally, the velocity profile and pressure plots around the moving rudder were studied and compared with OU-PIV measurements. The general forecast of motions was promising and quantitative values of maneuvering characteristic was reasonable.

TABLE OF CONTENTS

ACKNOWLEDGEMENTS ..... **i**

ABSTRACT ..... **ii**

LIST OF TABLES ..... **vi**

LIST OF FIGURES ..... **vii**

LIST OF ABBREVIATIONS ..... **x**

LIST OF SYMBOLS ..... **xii**

PAGE NO.

CHAPTER 1 INTRODUCTION **1-11**

1.1 General Background 1
1.2 Motivation 4
1.3 Objective 9
1.4 Organization of the thesis 10

CHAPTER 2 COMPUTATIONAL METHOD **12-22**

2.1 Dynamic Overset Grid 12
2.2 Overview of CFDShip-Iowa V4.5 12
2.2.1 *Governing Equations* 13
2.2.2 *Kinematic of Motions* 14
2.2.3 *Forces and Moments* 15
2.2.4 6 *DOF Motions* 15
2.3 Osaka University Propeller Model 16

CHAPTER 3 GEOMETRY AND TEST CONDITIONS **23-26**

3.1 Geometry 23
3.2 Simulation Test Matrix 25

CHAPTER 4 GRID SYSTEMS 27-32

4.1 Grid Generation 27
4.2 Hierarchy of Overset Grid 31

CHAPTER 5 SIMULATION DESIGN 33-39

5.1 Computational Domain and Boundary Conditions 33
5.2 Numerical Schemes 35
5.3 Controllers 36
5.4 Adopted Coordinate System 37
5.5 High Performance Computing 38
5.6 Propeller Open Water Coefficients 38

CHAPTER 6 MANEUVERING IN CALM WATER 40-87

6.1 Hydrostatics 40
6.2 Self-Propulsion under Course-Keeping Control 41
6.2.1 *PID Controlled Variable* 44
6.2.2 *Propeller Forces* 44
6.2.3 *Motions* 45
6.2.4 *Neutral Rudder Angle* 46
6.2.4 *Local Flow Prediction* 47
6.3 Calm Water Maneuvering 50
6.3.1 *Turning Circle Maneuver* 50
(a) *Portside Turning* 52
(b) *Starboard Turning* 55
(c) *Sensitivity Test* 58
6.3.2 *Zigzag Maneuver* 61
(a) *Zigzag Maneuver Characteristics* 62
(b) *Free-Surface Analysis* 73
(c) *Axial Velocity Contours* 75

CHAPTER 7 MANEUVERING IN HEAD WAVES.....88-103

7.1 Course-Keeping in waves 88
7.1.1 *Time Histories* 89
(a) *Propeller Rotational Speed* 89
(b) *Motions* 90
(c) *Thrust and Torque* 90
(d) *Neutral Rudder Angle* 91
7.1.2 *Harmonic Analysis* 92
7.1.3 *Local Flow Predictions* 99

CHAPTER 8 CONCLUSION AND FUTURE SCOPE.....104-107

8.1 Summary 104
8.2 Future Work 106

REFERENCES.....108

LIST OF TABLES

TABLE NO.	TABLE TITLE	PAGE NO.
3.1	Main particulars of KCS with its appendages	24
3.2	OU-CFD Test Matrix	26
4.1	Details of grid system-G1	30
4.2	Details of grid system-G2	32
5.1	Detailed Boundary conditions	35
5.2	Processor allocation for grid system G1	39
5.3	Thrust and Torque Coefficients	39
6.1	Comparison of self-propulsion parameters	45
6.2	Comparison of portside turning circle parameters	54
6.3	Comparison of starboard side turning circle parameters	57
6.4	Comparison of 1st and 2nd overshoot for -20°/20° maneuver	64
6.5	Comparison of 1st and 2nd overshoot for 20°/20° maneuver	66
6.6	Comparison of 1st and 2nd overshoot for -10°/10° maneuver	68
6.7	Comparison of 1st and 2nd overshoot for 10°/10° maneuver	70
7.1	Comparison of propeller revolution in varying wavelengths	90

LIST OF FIGURES

FIGURE NO.	FIGURE TITLE	PAGE NO.
1.2	Overview of maneuvering prediction methods.	3
2.1	Earth-fixed inertial and ship-fixed coordinate system.	14
2.2	Blade element for inviscid code.	18
2.3	Blade element using total velocity.	19
3.1	KCS model geometry with propeller.	23
4.1	A1: Surface grid of bare hull for grid system-G1. A2: Surface grid of bare hull for grid system-G2. B1: Enlarged view of Grid system G1 showing original underhung rudder geometry. B2: Enlarged view of Grid system G2 showing simplified rudder geometry.	29
4.2	Overset grid system-G1, six blocks: bare hull, rudder-fixed, rudder-movable, propeller, refinement and background.	31
4.3	Overset grid system-G2, six blocks: boundary layer, hub, propeller, rudder, wake refinement and background.	32
5.1	Adopted computation domain along with imposed boundary conditions for grid system G1.	34
5.2	Adopted computation domain along with imposed boundary conditions for grid system G2.	34
5.3	Adopted coordinate system.	38
6.1	Comparison of time histories of PID controls and trajectories during the self-propulsion simulation.	42
6.2	Comparison of time histories of motions and forces during the self-propulsion simulation.	43
6.3	Dynamic pressure and Streamlines and (Right) Velocity contours at various p_z/R sections.	46
6.4	Axial Velocity Contours at various x/L sections.	48

6.5	Comparison of flow field at *x/L*=1.025 (a) OU S-PIV (b) IIHR-CFD AP (c) OU-CFD G2 (d) OU-CFD G1.	49
6.6	A typical example of motion path of centre of gravity during a turning circle test defining the terminologies involved.	51
6.7	Comparison of time histories of motions, motion rates, velocities, rudder and heading angle during the portside turning maneuvering simulation.	53
6.8	Comparison of time histories of motions, motion rates, velocities, rudder and heading angle during the starboard turning maneuvering simulation.	56
6.9	(a) Time histories of Ship Forces for -35°; (b) Time histories of Ship Forces for -30°; (1) Time histories of Rudder Forces for -35°; (2) Time histories of Rudder Forces for -30°.	60
6.10	A typical example of time histories of rudder angle and yaw response during zigzag maneuver.	61
6.11	Comparison of time histories of motions, motion rates, velocities, rudder and heading angle during the -20°/20° maneuvering simulation.	63
6.12	Comparison of time histories of motions, motion rates, velocities, rudder and heading angle during the 20°/20° maneuvering simulation.	65
6.13	Comparison of time histories of motions, motion rates, velocities, rudder and heading angle during the -10°/10° maneuvering simulation.	67
6.14	Comparison of time histories of motions, motion rates, velocities, rudder and heading angle during the 10°/10° maneuvering simulation.	69
6.15	Time histories of rudder forces and moment (below) corresponding to the yaw response and rudder angle (top) during the (a) 10°/10° and (b) 20°/20° maneuvering simulation.	72
6.16	Free surface elevation for different stages of the 20°/20° maneuver.	73
6.17	Free surface coloured with U-velocity for different stages of the 20°/20° maneuver.	74
6.18	Axial Velocity Contours at x/L=0.975 at various time steps of 20°/20° maneuver.	76-81
6.19	Axial Velocity Contours at *x/L*=1.01 at various time steps of 20°/20° maneuver.	82-87
7.1	Time history comparison for course-keeping simulation at λ/L=0.65.	93
7.2	Time history comparison for course-keeping simulation at λ/L=1.00.	94
7.3	Time history comparison for course-keeping simulation at λ/L=1.15.	95

7.4	Time history comparison for course-keeping simulation at λ/L=1.37.	96
7.5	Harmonic amplitude of heave and pitch in head waves with varying λ/L.	97
7.6	Harmonic amplitude of thrust and torque coefficients in head waves with varying λ/L.	99
7.7	Harmonic amplitude of rudder and yaw angle in head waves with varying λ/L.	99
7.8	Local flow comparison behind rudder (*x/L*=1.025) for course-keeping simulation at λ/L=0.65. (Left) OU S-PIV (Mid) OU-CFD G2 (PID) (Right) OU-CFD G1 (PID).	101
7.9	Local flow comparison behind rudder (*x/L*=1.025) for course-keeping simulation at λ/L=1.15. (Left) OU S-PIV (Mid) OU-CFD G2 (PID) (Right) OU-CFD G1 (PID).	102
7.10	Local flow comparison behind rudder (*x/L*=1.025) for course-keeping simulation at λ/L=1.37. (Left) OU S-PIV (Mid) OU-CFD G2 (PID) (Right) OU-CFD G1 (PID).	103

LIST OF ABBREVIATIONS

AP	Aft Perpendicular
BF	Body Force
BKW	Blended k-ε/k-ω
CFD	Computational Fluid Dynamics
CMT	Circular Motion Test
DCI	Domain connectivity information
DES	Detached Eddy Simulation
DOF	Degree of freedom
DP	Discretized Propeller
EASM	Explicit algebraic stress model
EFD	Experimental Fluid Dynamics
FP	Fore Perpendicular
IIHR	Iowa Institute of Hydraulic Research
IMO	International Maritime Organization
IITC	International Towing Tank Conference
KCS	KRISO Container Ship
KRISO	Korean Research Institute for Ships and Ocean Engineering
KVLCC	KRISO Very Large Crude Carrier
LCG	Longitudinal centre of gravity
MARIN	Maritime Research Institute Netherlands
MPI	Message passing interface
OSA	Overshoot angle

OU	Osaka University
PID	Proportional-Derivative-Integral
PISO	Pressure-Implicit Split-Operator
PMM	Planar Motion Mechanism
RANS	Reynolds' Averaged Navier Stokes
SBS	System Based Simulations
SNAME	Society of Naval Architects and Marine Engineers
SPIV	Stereo Particle Image Velocimetry
SST	Shear Stress Transport
URANS	Unsteady Reynolds' Averaged Navier Stokes
VLCC	Very Large Crude Carriers
V&V	Verification and Validation

LIST OF SYMBOLS

A	Wave amplitude
A_d /L	Non-dimensionalised advance
A_W	Wetted area without rudder
a_0	Zeroth harmonic amplitude
a_n, b_n	Fourier coefficients
B	Beam at the waterline
c	Chord length
C_B	Block coefficient
C_D	Drag coefficient
D	Experimental data
D_t	Depth of ship
D_p	Diameter of propeller
dD	Segmental drag
dL	Segmental lift
dT	Segmental thrust
dQ	Segmental torque
E	Error
$E\%D$	Error normalized using the experimental data
f_e	Wave encounter frequency
Fn	Froude Number
F_n	nth harmonic amplitude
F_{bx}, F_{by}, F_{bz}	Body force in x-direction, y-direction and z-direction

g	Acceleration due to gravity
$G1$	Grid system generated using the original semi-balanced horn rudder geometry
$G2$	Grid system generated using a simplified spade rudder
h	Advancing distance for one radian of helical vortex
H	Wave Height
H_p	Pitch of helical vortex
i_{max}, j_{max}, k_{max}	Total number of grid points in the i, j and k-direction
I_x, I_y, I_z	Moment of Inertia around x-axis, y-axis and z-axis respectively
J	Advance coefficient
k	Wave number
k_t	Turbulent kinetic energy
KG	Vertical Centre of Gravity from ship keel
K_T	Propeller thrust coefficient
K_{T0}, K_{T1}	Zeroth and First harmonic amplitude of propeller thrust coefficient
K_Q	Propeller torque coefficient
K_{Q0}, K_{Q1}	Zeroth and First harmonic amplitude of propeller torque coefficient
K_{XX}, K_{YY}, K_{ZZ}	Radius of gyration around x-axis, y-axis and z-axis respectively
$L = L_{pp}$	Length between perpendiculars
L_f	Lift force
m	Mass of the ship
Ne	Time step number
N_p	Number of blades of the propeller
n	Non-dimensional propeller revolutions
$n_{self\text{-}propulsion}$	Predicted propeller revolution from self-propulsion simulation

$n(t)$	Instantaneous propeller revolutions
p	Pressure
p	Piezometric pressure coefficient
p_{abs}	Absolute pressure
p_d	Dynamic pressure
p_x/L	Non-dimensionalised position of propeller centre along x-direction
p_z/L	Non-dimensionalised position of propeller centre along z-direction
$\Delta p(t, y, z)$	Pressure jump in the x-direction
$\Delta p(t, r, \theta)$	Pressure jump in the propeller plane
Δp_{SA}	Short-term averaged pressure jump
P	Geometric propeller pitch
P_e	Effective propeller pitch
P_n, I_n, D_n	Parameters of feedback controller 'cruise'
$P_\delta, I_\delta, D_\delta$	Parameters of feedback controller 'cruise'
Q	Torque
r	Yaw rate
r_x/L	Non-dimensionalised position of rotational axis of rudder in the x-direction
Rn	Reynolds Number
Rn_{eff}	Effective Reynold Number
S	Computed data
S_i	Source term
S_1	OU computed data using grid system G1
S_2	OU computed data using grid system G2
t	Time

Δt	Time step
T_d	Ship draft in fully loaded condition
Te	Non-dimensionalised wave encounter period
T_D/L	Non-dimensionalised tactical diameter
T_r/L	Non-dimensionalised transfer
T	Thrust
U	Ship Service speed
U_0	Predicted ship velocity corresponding to prescribed Fn achieved in the self-propulsion simulation
U_T	Target non-dimensionalised speed
$U(t)$	Instantaneous ship speed
u, v, w, p, q and r	Surge, sway, heave, roll, pitch and yaw velocities in ship co-ordinate
$\bar{u}, \bar{v}, \bar{w}, \bar{p}, \bar{q}$ and $\bar{r}$	Surge, sway, heave, roll, pitch and yaw accelerations in ship co-ordinate
u_∞, v_∞, w_∞	Free-stream velocity component in x-direction, y-direction and z-direction respectively
u_{ip}	Induced velocity component in the axial direction
u_{total} and $v_{\theta total}$	Total velocity
u_e and $v_{\theta e}$	Effective velocity
$v_{\theta ip}$	Induced velocity component in the tangential direction
W	Total inflow velocity
x, y, z	Independent Cartesian co-ordinate directions
$\bar{x}, \bar{y}, \bar{z}, \bar{\phi}, \bar{\theta}$ and $\bar{\psi}$	Times rate of change in the translations and Euler angles
X, Y, Z, K, M, N	Surge, sway, heave, roll, pitch, yaw forces in ship co-ordinate
X_0, Y_0	Initial ship position in the earth-fixed coordinate system at the start of maneuvering
x_G, y_G, and z_G	The distance of centre of gravity from the centre of rotation of the ship

Δx	Propeller grid spacing in axial direction
$y+$	Dimensionless wall distance
z_w	Water depth
z_0, z_1	Zeroth and First harmonic amplitude of heave
$\Gamma(r)$	Circulation at radius = r
α	Angle of attack
α_g	Geometric pitch angle
α_{g1}	Effective pitch angle
β	Drift angle
γ_n	n^{th} harmonic phase
δ	Rudder deflection angle
δ_0	Predicted rudder deflection angle achieved in the calm water self-propulsion simulation
δ_1	First harmonic amplitude of rudder angle
$\delta(t)$	Instantaneous rudder angle
ζ	Wave elevation
θ	Pitch angle
θ_0, θ_1	Zeroth and First harmonic amplitude of pitch angle
θ_p	Angular position of the generator line
∇	Displaced volume of ship
λ	Wavelength
λ_s	Scale
ν_t	Eddy viscosity
ρ	Fluid density
υ	Kinematic viscosity

υ_t	Turbulent viscosity
Φ, φ	Roll angle
ϕ_s	Level set function
χ	Encounter Angle
ψ_T	Target yaw/heading angle
$\psi(t)$	Instantaneous yaw angle
ψ_1	First harmonic amplitude of yaw angle
ω	Wave frequency
ω_e	Wave encounter frequency (rad/s)
ω_t	Specific dissipation rate

CHAPTER 1

INTRODUCTION

1.1 General Background

The classic work of Euler's equation of motion opened up scientific work in the field of maneuvering as early as 1749, yet maneuverability assessment was not a key consideration in ship performance except for naval vessels for many following years. The terminology of maneuvering referred to just turning ability in the case of merchant ships. With increasing worldwide demands of increased transport efficiency, oil tankers started to increase their size altogether, and eventually, Very Large Crude Carriers (VLCC) came into the scene in the late 1960s. The entry of VLCC, with remarkable growth in ship size, led (with lower L/B ratio) to problems in the ship maneuverability because of its inherent unstable course-keeping features. Many maritime accidents of oil tankers were apprehended to have been caused by its poor course-keeping ability but not solely because of it. The objectionable features on the course-keeping ability of VLCCs brought in an opportunity for designers and handlers to fathom the importance of ship maneuverability at the initial ship design stage, the first time in history. Thereon, increased attention has been paid to this field of ship hydrodynamics. In recent years, international organizations such as the International Maritime Organization (IMO), the International Towing Tank Conference (ITTC), and the Society of Naval Architects and Marine Engineers (SNAME) have become more functioning in stimulating numerical and experimental research on ship maneuverability critical for safer shipping and cleaner oceans.

Appropriate prediction of maneuvering performance has a substantial influence on:

- Avoidance of marine accidents.
- Dynamic stability and ship motions.
- Operational costs.

No simple criteria exist to judge the maneuvering performance of a ship. The flow phenomenon associated with maneuvering is complex and often associated with other phenomena. Further complications could arise with restricted water depths, side banks in the

vicinity, or the presence of another hull nearby, by influencing hydrodynamic forces and moments acting on the hull.

As abstracted in the reports by the Maneuvering Committee of the International Towing Tank Conference [1, 2], for ship maneuverability, modern prediction tools mainly include, but not limited to, empirical formulae, full-scale trials, model tests (also quoted as a technique of Experimental Fluid Dynamics, EFD), System Based Simulations (SBS) and Computational Fluid Dynamics (CFD) simulation. Figure 1.1 gives the overview of maneuvering prediction.

Model tests are divided into *free-running model tests or Open-Loop Maneuvers* (model's path is not controlled) and *captive model tests* or *Closed-Loop Maneuvers* (model's path is controlled). Standard maneuvers (such as turning, zig-zag, spiral, stopping, pull-out maneuvers, etc.), in free-running model test, are performed and the resultant trajectory is recorded. With the measured trajectory, the maneuvering performance is assessed. On the other hand, captive model tests provide forces and moments acting on the hull through prescribed motions. The conventional prediction mechanism for ship maneuvering is model testing. Even though the method provides a direct and reliable assessment of the hydrodynamic characteristics for a maneuvering ship due to its closeness to the real performance, its usage is limited to the final stages of design primarily because:

(a) High cost and time-consuming.
(b) The flow field to understand the propeller-hull-rudder interaction is rarely measured.

System based simulations (SBS) and potential flow methods are fast and require fewer resources to predict the maneuvering and seakeeping performances. SBS approach is dependent on the integral coefficients obtained from experimental or CFD methods. The reliability of the approach is, thus, dependent on the accuracy of the predicted coefficients. On the other hand, potential/inviscid flow theory is less reliant on models as it solves the flow equations. The approach, however, is limited by the assertion of the non-viscous hypothesis critical in maneuvering studies.

CFD provides answers to the limitations of various maneuvering prediction tools. With the advent of supercomputers and improvement in numerical algorithms, the use of CFD in ship hydrodynamics simulations has gained momentum. To investigate the ship

maneuvering problem in practice, at present, the Unsteady Reynolds Averaged Navier Stokes (URANS**)** technique is the most common viscous flow method. Reproducing specific maneuvers or course-keeping by direct CFD simulations using actual rotating propeller and moving rudder solves the complex hull-propeller-rudder interaction and provides accurate maneuvering prediction. Information on the hydrodynamic load and local flow field is easily accessible. Such information is valuable to understand the mechanism. The method, however, is computationally expensive. Alternatively, coupled CFD/Potential method approach reduces the computational expense. A sophisticated potential flow propeller code coupled interactively with a flow solver capable of capturing the hull-propeller-rudder interaction precisely is advantageous. CFD approach has many advantages compared to its counterpart but its accuracy in predicting the maneuvering performance of a ship is dependent on but not limited to, grid quality, propeller model, and computational resources.

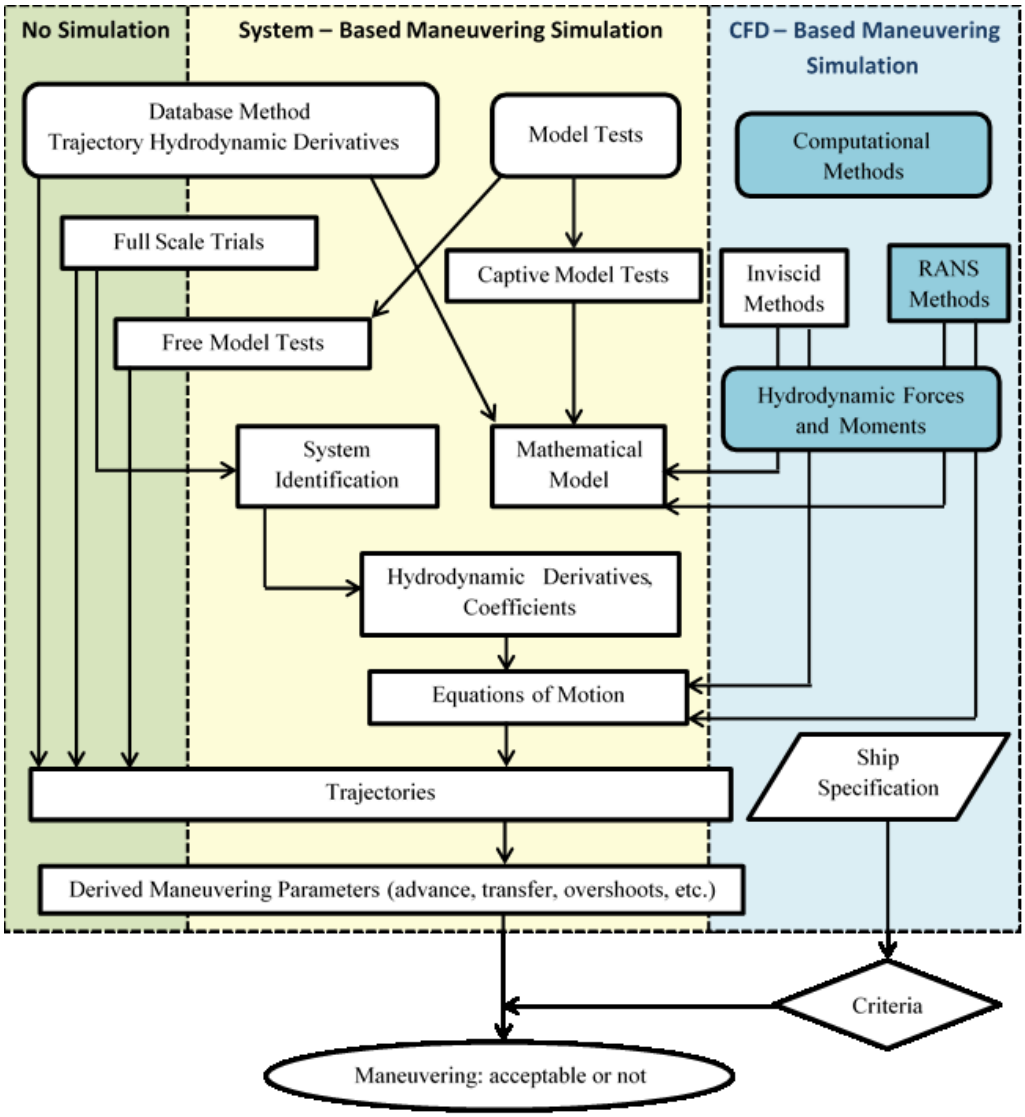

Figure 1.1 Overview of maneuvering prediction methods [reproduced from 1].

1.2 MOTIVATION

Traditionally, the seakeeping and maneuvering behaviour of free-running ships has been analysed using experiments. Kim *et al.* [3] performed towing tank experiments at KRISO to obtain resistance, mean flow data, and free surface waves for KRISO Very Large Crude Carrier (KVLCC), KVLCC2, and KCS. Thereafter, the hull forms have been benchmarked for the validation of numerical and computational approaches for various ship applications. Extensive experimental studies have been conducted at IIHR by Araki *et al.* [4] and Sanada *et al.* [5] in various conditions for free-running models. The experimental data are available through Tokyo 2015: A Workshop on CFD in Ship Hydrodynamics (T2015). The experimental results are invaluable as it helps in validating the computational results for various test conditions. Owing to the limiting factors of model testing as pointed out earlier, CFD provides a favourable approach in maneuvering studies. Various CFD applications in the past have concentrated on numerically simulating captive maneuvering tests. However, only a few free-running simulations have been reported in the literature, especially in waves, owing to higher computational costs.

One of the first attempts to numerically simulate captive model experiments was presented in [6]. Numerical methods were developed for steady oblique tow replicating oblique towing test and steady yawing simulations replicating the Circular Motion Test (CMT) and Planar Motion Mechanism (PMM) tests. The method was then extended to unsteady forced motion. Various hull forms were deployed for the simulations. Hydrodynamic forces and the moment, the longitudinal distribution of the hydrodynamic lateral force, and the pressure distribution on the hull surface were presented. The work was remarkable as it introduced the capability of CFD in the maneuvering field of ship hydrodynamics. Similar studies to numerically replicate captive maneuvering tests were presented by Turnock *et al.* [7], Toxopeus *et al.* [8, 9], and Zou *et al.* [10, 11]. A detailed study on the Verification and Validation (V&V) of CFD solutions for an unappended tanker maneuvering at varying drift angles and water depths having three degrees of freedom (DOF)-free to surge, sway, and yaw, was presented by [10, 11]. SHIPFLOW®, a steady state RANS solver, was employed to solve the viscous flow. The effect of free-surface, sinkage, and trim was not considered in the study. Of utmost importance, the numerical uncertainties were computed through a grid convergence, turbulence modelling error studies.

Simulating captive maneuvering tests has its advantages, as the approach requires less computational resources. The integral coefficients derived from the captive test are then fed into a mathematical model to predict the trajectories of the standard maneuvers. The accuracy of the approach is, however, dependent on the mathematical model itself. Also, complex flow around a rotating propeller and moving rudder are not solved due to simplified mathematical modelling. With the rapid development of computer technology, CFD simulations progressed from captive to free-running 6DOF conditions. The advantage of solving RANS with 6DOF capabilities is the elimination of mathematical models and analytical formulas for the prediction of trajectories of definitive maneuvers with increased flow-field detailing of maneuvering ships.

One of the first steps in simulating free maneuvers is to precisely predict the self-propulsion point. Experimentally, this is achieved by standard towing tank procedure where the propeller revolution that yields zero towing force (i.e., the propeller thrust and the total resistance of the ship are balanced) is the self-propulsion point. However, the procedure involves multiple runs at various propeller revolutions. The propeller revolution that zeroes the towing force, thereafter, is interpolated from the runs that recorded negative and positive towing forces. The method is time and resource-consuming. In this regard, Carrica *et al.* [12] presented a detailed procedure for the direct prediction of self-propulsion point in a single run using a speed controller and a discretized propeller with an overset grid using the Detached Eddy Simulation (DES) turbulence model. Three hull forms were evaluated: the single screw single rudder KVLCC1 tanker, twin-propeller, fully-appended surface combatant model DTMB 5613, and the KCS without a rudder. The results were compared with model scale experimental data. Though resource-intensive, the approach provided promising results and suggested that the methodology could be used in direct computations of self-propelled ships. Compared to the experimental method, however, the procedure showed reduced time requirement. The approach was further utilized by Castro et al. [13] for full-scale self-propulsion simulations of KCS.

6DOF motion solvers coupled with dynamic overset grids with a hierarchy of body, first introduced in self-propulsion studies, are now the most robust and reliable proposition in free-running simulations. Standard maneuvering simulations (35° steady turn and zigzag 20°/20°) were conducted using Unsteady Reynolds-averaged Navier Stokes (URANS) code CFDShip-IOWA v4 for MARIN 7967 (European version of US Navy DTMB 5415) at the

model and full scale by Carrica *et al.* [14]. The results were benchmarked against experimental time histories of motion and motion rates and also compared against available integral variables. The error was within 10% of experimental data, highly satisfactory considering the degree of complexity involved. The full-scale case produced a thinner boundary layer profile compared to the model scale with different turbulence scales needed for maneuvering. The computations showed the feasibility of URANS computation in full-scale maneuvering, though the issue of adequate propeller modelling remained. Mofidi and Carrica [15] used CFDShip-IOWA V4.5 to compute zigzag maneuvers: 10°/10° and modified 15°/1° of KCS. The direct simulation was performed with an active rudder with a fully discretized propeller using the Delayed Detached Eddy simulation. The study revealed the feasibility of using a moving rudder and rotating propeller in a CFD environment. It was found that a strong correlation exists between the axisymmetric behavior of the rudder and the asymmetry introduced by the single rotating propeller. The approach provided a good agreement with experimental data but the authors stressed on the high computational cost in direct maneuvering simulations. Shen *et al.* [16] applied dynamic overset grids (SUGGAR ++) to OpenFOAM known as naoe-FOAM-SJTU to predict 6DOF self-propulsion and zigzag maneuvers of KCS. In contrast to previous studies, an unstructured overset grid with a rotating propeller and movable semi-balanced horn rudder was implemented. The technique provided flexibility in mesh generation of complex geometries and provided satisfactory agreement with experimental data with coarse unstructured grids. The same solver was used by Wang *et al.* [17] to predict the turning circle maneuver of the ONR tumblehome model and the results agreed well with the experimental data set.

Foregoing studies in the free-running ship with discretized propeller and moving rudder were, for the most part, focused on calm water. Few studies have concentrated on free-running simulations in waves. The performance of a ship is strongly affected by the sea environment. In waves, the propulsion efficiency decreases, and added powering is required for efficient ship operation. Additionally, the waves affect the path of an advancing ship and may cause the vessel to deviate from its original course. To maintain straight-line stability, course control is advocated. Sailing straight forward in a real sea state is advantageous as it amounts to lower operational costs. Thus, the accurate evaluation of course-keeping behaviour and propulsive factors is crucial. On this topic, Wang *et al.* [18] presented numerical studies of fully appended ONR Tumblehome under course-keeping control in various head waves using naoe-FOAM-SJTU a CFD solver, developed on open source

platform OpenFOAM. Fully appended hull with discretized real propeller and moving rudders applying the overset grid technique and 6DOF module with a hierarchy of bodies were adopted to handle the free-running ship motions A proportional-integral controller was employed for self-propulsion computation in calm water at Fn=0.2 The obtained self-propulsion model point was then frozen and used for the course keeping computations in regular waves: head wave, bow quartering wave, and beam wave. A newly developed feedback controller was used in the CFD solver naoe-FOAM-SJTU to meet the demands of course keeping. The estimated results were compared with the benchmark data of Tokyo 2015: A Workshop on CFD in Ship Hydrodynamics [19]. The approach provided good agreements with available experimental data and showed that the newly developed controller coupled with the CFD solver could be effectively used in these computations. Detailed flow visualization was also presented to explain the hydrodynamic performance of ship hull-propeller-rudder interaction in waves under course-keeping conditions. The authors again stressed on high computational costs in direct simulations.

Sanada *et al.* [20] compared experimental data of IIHR 6DOF motions (Sanada *et al.*, [21]), OU towing tank 3DOF motions (Wu *et al.*, [22]), and other institutions with computational study of appended KCS for added powering and maneuvering performance in calm water and waves. The simulations were performed using a fully discretized propeller and an axisymmetric body force (BF) propeller model coupled with CFDShip-IOWA V4.5. The fully discretized propeller method was implemented using coarser grids compared to the BF model. The BF model in fine grids performed better than the actual rotating propeller in coarse grids. The study revealed that a low fidelity model was capable of producing good agreement with experimental data compared to a high fidelity model provided the grid has a good resolution to capture the highly turbulent flow in maneuvering ship. However, the authors stressed that the propeller performance was not predicted accurately by the BF model. The BF model itself is based on ship speed and not on the propeller inflow velocity leading to inaccuracies in propeller performance. Various other studies have been conducted in waves, including, Carrica *et al.* [23], Simonsen *et al.* [24], Sadat-Hosseini *et al.* [25], and Sadat-Hosseini *et al.* [26] for added-resistance/added-powering studies under the sea-keeping domain. The studies showed the effect of thrust oscillation and viscous ship wake in waves for propulsion prediction.

The above-reviewed studies showed that an actual rotating propeller solves the complex hull-propeller-rudder interaction. The major drawback involved in using a fully discretized propeller in a self-propelled ship is the dissimilarity in timescale between the ship and the propeller. To capture the turbulence of the flow around the propeller accurately, the resolution demands a very small time step compared to that of the ship. Alternately, body force propeller models reduce computational expense as detailed propeller modelling is not required. The complexity of the body force model varies. Thus, it is advantageous to use sophisticated body force propeller models capable of capturing the hull-propeller-rudder interaction precisely by working interactively with the CFD solver. The use of body force propeller models in various ship hydrodynamics applications has been studied in the literature. One of the earliest attempts, in this regard, was presented by Simonsen and Stern [27]. The hull-propeller-rudder interaction was determined by coupling the RANS code with a simplified propeller model. The propeller model was based on potential flow theory and detailed modelling of the propeller was not necessary. The computations were performed for an open water test, series 60 ships sailing straight ahead, and appended Esso Osaka tanker in various maneuvers. The effect of the various maneuvers on the flow field was reflected in the velocity distribution and propeller loading. The approach achieved a reasonable agreement with the experimental data and showed that using a propeller model is feasible in maneuvering simulations. Sadat-Hosseini *et al*. [28] coupled URANS CFD solver with a fully discretized rotating propeller and two BF propeller models: interactive Yamazaki and non-iterative axisymmetric to study self-propulsion and free-running maneuvers. The strengths and weaknesses of each approach were identified as the study provided a good basis for comparison.

A new simplified quasi-steady body force propeller model, named OU propeller model, based on blade element theory was proposed by Tokgoz *et al.* [29]. The model was coupled with a RANS CFD solver to study the propeller performance. This study aimed at reducing the computational and modelling efforts while maintaining the effect of ship motion. Traditionally, potential flow based propeller codes work with induced velocities (sum of the bound vortex and free vortex) whereas RANS solver works with total velocities. The total velocities are the summation of inflow velocity (effective wake) and the propeller-induced velocities. Thus, when the propeller code is coupled with the RANS solver, the induced velocities are required to be subtracted from the total velocity to accurately yield the propeller inflow velocity. The induced velocity is computed using various established

techniques. Traditionally, these methods assume the path and direction of the free vortex. This assumption leads to inaccurate predictions of propeller performance, especially in maneuvering simulations, where, the motion of propeller wake (free vortex) is relative to the ship and is not fixed. Using the total velocity eliminates the need for the subtraction of induced velocity and the free vortex is directly provided by the RANS solver. The only unknown term is bound vortex (on the body surface) that is computed in the propeller code. The method is also easy to couple with free-surface models already present in the RANS solver. Unlike the Yamazaki propeller model, in the OU propeller model, the direction and path of the free vortex is not fixed but moves relative to ship motions, critical to maneuvering studies. The approach incorporates the blade profile and the propeller side forces and yaw moment, unlike the axisymmetric propeller model. The propeller model was further used by Wu *et al.* [29] and Wu *et al.* [30] to analyse self-propelled KVLCC2 and KCS respectively in calm water and regular waves, primarily in sea-keeping studies. Both studies reported good agreement with experimental data, which showed the use of the OU propeller model in self-propelled ships in waves is feasible.

In light of the preceding, this work aims to overcome the limitations of numerical and experimental predictions of maneuvering characteristics. Here, we present an alternative or eventually a complementary method when the traditional maneuvering prediction tool tends to be a hard task for proper estimation. In this context, the intent was to propose an approach that maintained the advantages of experimental prediction but also addressed the following conditions:

(a) Higher accuracy and reliability of the numerical prediction

(b) Compatibility with any standard maneuver

(c) Proper complex parameters extraction.

(d) Reduced computational expense.

1.3 OBJECTIVE

The main objective of this research was to assess the applicability of the OU propeller model coupled with RANS solver, CFDShip-Iowa, in free-maneuvering studies. Briefly, the advantages of our approach can be outlined as follows:

(i) Reduced computational expense.

(ii) As the model is based on total velocity at the propeller plane, it eliminates the need for induced velocity deduction. Therefore, any other inviscid code can be modified by removing the induced velocity subroutine, making the approach robust.

(iii) Effective in predicting propeller performance in unsteady or asymmetric flow.

The present study extends the previous researches to maneuvering in unrestricted calm water and waves, including added powering for a ship with a high Froude number (Fn) and low block coefficient (C_B). This work states the use of numerical tools in studying the motions, motion rates, propeller thrust and torque, and hydrodynamic forces and moment acting on a maneuvering ship in calm water and head waves. In addition, this study also focused on the reliable prediction of flow field during maneuvering thereby understanding the complex hull-propeller-rudder interactions. Velocity profile at various sections across the hull and streamlines and pressure plots around the rotating rudder were studied. In this study, the results from CFD computation were validated with the available model experiments data to ensure reliable prediction. The results were also compared against other propeller models to understand the limitations and effectiveness of OU propeller model. The sensitivity of our approach was investigated with an eye for possible modelling errors.

1.4 OVERVIEW OF THE THESIS

The whole thesis is organized as an essay containing eight chapters as follows:

– Chapter 1 provides a general background about the available prediction technologies to assess the maneuverability of a ship - their advantages and disadvantages. In the following part, a literature review providing an insight into the status of numerical assessment capabilities of maneuvering characteristics is added. The objective and motivation of this study are described thereafter.

– Chapter 2 describes the computational methodology used during this work. In the first part, details of the generated grid will be given. This is followed by a review of the basic framework of the adopted computational solver. We extend the review to the propeller model used. Details of the governing equations will be shown. The numeral computations are based on these characteristic equations.

– Chapter 3 presents the simulation conditions along with the geometry data used in all computations.

– Chapter 4 describes reports the adopted grid systems used in this computational study.

– Chapter 5 reports the adopted computational domain and boundary conditions used in this study. The various numerical schemes are then presented. This followed by the description of the controller system. The last part of this chapter is focused on the propeller open water coefficients used.

– Chapter 6 furnishes the computational results in calm water. Detailed explanations of the simulated results-self propulsion, zigzag maneuvers, and turning circle maneuver are provided along with an analysis of flow field.

– Chapter 7 the computational results of maneuvering in head waves. The harmonic analysis of the unsteady series has also been added. The last part of this chapter is focused on the local flow prediction.

– Chapter 8 concludes this work by summarizing and reviewing our main findings. Here, we emphasize the importance of the work. Some perspectives and extensions of the work are also provided.

CHAPTER 2

COMPUTATIONAL METHOD

2.1. DYNAMIC OVERSET GRID

When replicating complex ship motions numerically with irregularly shaped and moving components, such as propeller and rudder, a dynamic overset grid is the essence. An overset simulation requires three steps, namely, grid generation, hole cutting, and determination of interpolation weights. Two or more blocks of an independent, overlapping, structured, or unstructured grid in a computational domain are first integrated together, to form a composite grid. Following this, all exterior or unused points that are outside the domain of interest are identified. The grid is divided into several categories depending on their location, like donor cell, orphan, active cell, hole cell, fringe cell. Adjacent grid points to the hole or the boundaries of each component grid are called the fringe point. Information on a flow variable is obtained by fringe cells through interpolation from the appropriate donor cells that overlap the region. The various cell type that are identified along with their associated interpolation weights a called domain connectivity information (DCI) for the composite overset grid.

2.2. OVERVIEW OF CFDSHIP-IOWA V4.5

CFDShip-Iowa v4.5 [31-33], developed by IIHR, The University of Iowa, was employed for the ship hydrodynamics computations in this study. It is an overset, multi-block structured (with parent/child hierarchy), incompressible URANS, higher-order finite-difference motion solver with capabilities of handling interactive or prescribed body-force propeller model, or an actual rotating propeller. The flow equations are capable of being solved in an either absolute or relative inertial non-orthogonal curvilinear coordinate system for arbitrary moving but non-distorted control volumes. Two turbulence models available in the CFD solver include: the blended k-ε/k-ω (BKW) based isotropic with an option for shear stress transport (SST) model [34] and the Explicit Algebraic Stress Model (EASM) based anisotropic RANS and DES. Both the approaches can be used simultaneously with near-wall or no wall functions. For free-surface capturing, single-phase level-set method [35] tracking approach is available. Pressure-Implicit Split-Operator (PISO) algorithm or projection

method can be employed to solve incompressible RANS equations to achieve pressure-velocity coupling. For attaining parallel computing, a message passing interface (MPI) based on breakdown or disintegration of domain approach is included, where each disintegrated block is projected to one processor.

2.2.1. *Governing Equations*

Conservation of momentum and mass is described by a system of equations consisting of the Continuity equation (2.1) and the momentum equation (2.2) governing the fluid motion around a ship. Assuming the fluid to be incompressible, the governing equations given in a Cartesian coordinate system in the non-dimensional tensor form are:

$$\frac{\partial u_i}{\partial x_i} = 0 \tag{2.1}$$

$$\frac{\partial u_i}{\partial t} + u_j \frac{\partial u_i}{\partial x_j} = -\frac{\partial p}{\partial x_i} + \frac{\partial}{\partial x_j}\left[\frac{1}{Rn_{\text{eff}}}\frac{\partial u_i}{\partial x_j} - \frac{\partial u_j}{\partial x_i}\right] + S_i \tag{2.2}$$

where, $u_{i(j)} = (u,v,w)$ represents Reynolds-averaged velocity components

$x_{i(j)} = (x,y,z)$ denotes independent coordinates directions

S_i = Source term, for instance, body force due to a propeller model

$p =$ Piezometric pressure coefficient defined as: $\frac{p_{abs}}{\rho U_0^2} + \frac{z_w}{Fn^2} + \frac{2}{3}k$ (2.3)

In Equation 2.2 and 2.3, Fn is the Froude number, Rn_{eff} is the effective Reynolds number, and p_{abs} is the absolute pressure and is defined as:

$$Rn_{\text{eff}} = \frac{U_0 L}{\upsilon + \upsilon_t} \text{ and } Fn = \frac{U_0}{\sqrt{gL}} \tag{2.4}$$

where υ is the kinematic viscosity, z_w is the water depth, ρ is the fluid density, U_0 is the characteristic velocity, and L is the characteristic length. υ_t is the turbulent viscosity and k being the turbulent kinetic energy obtained from the applied turbulence model.

The location of the free-surface is provided by the level set function (ϕ_s) with the interface set at zero value of the level-set function, positive in water and negative in air. The interface is defined as Equation 2.5.

$$\frac{\partial \phi_s}{\partial t} + \frac{\partial (\phi_s u_i)}{\partial x_i} = 0 \tag{2.5}$$

2.2.2. *Kinematic of Motions*

Figure 2.1 shows the two coordinate systems: the inertial or Earth-fixed system (denoted with subscript E) and the non-inertial or ship-fixed system (denoted with subscript S) that are used to define the motions of a ship. The flow equations are solved in the inertial coordinate system. Using the linear translations (x, y, and z are the surge, sway, and heave translations, respectively) and Euler angles of roll (ϕ), pitch (θ), and yaw rotations (ψ), the position and orientation of the ship is described with respect to the inertial frame. The linear and angular velocities (u, v, and w are the surge, sway, and heave velocities, respectively; p, q, and r are the roll, pitch, and yaw angular velocities, respectively) are computed with respect to the ship-fixed reference frame. Force and moments are described with respect to the ship-fixed reference frame.

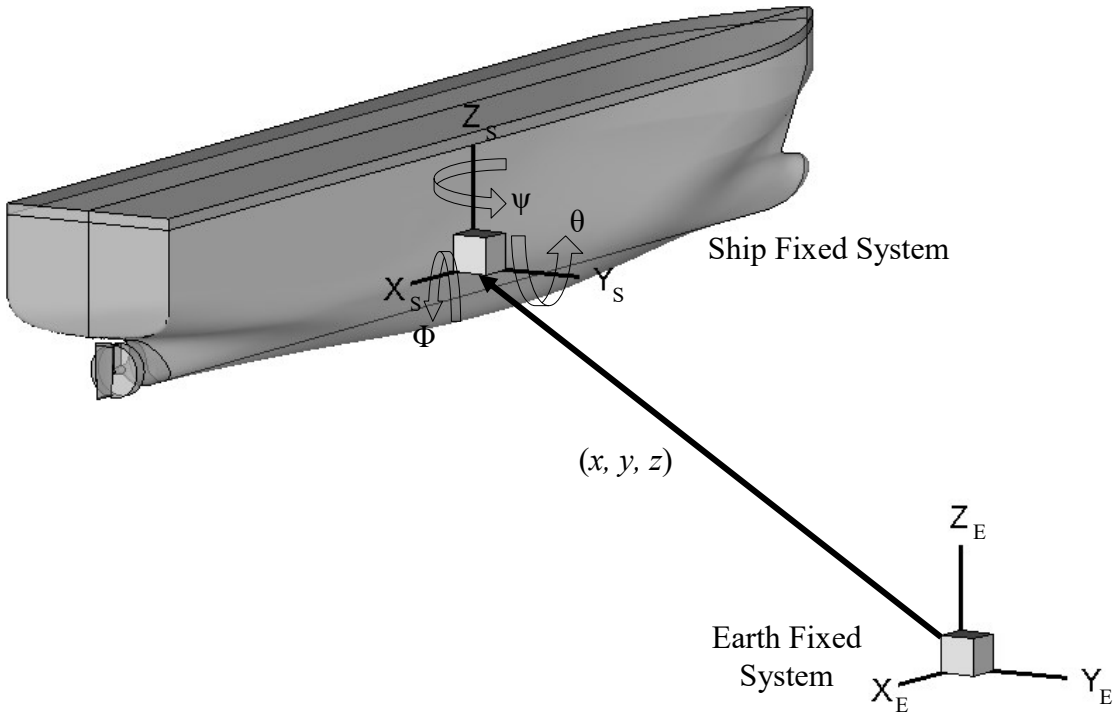

Figure 2.1 Earth-fixed inertial and ship-fixed coordinate system.

The linear and angular velocities in the ship-fixed reference system can be expressed as a relation to the time rate of change in the translations and Euler angles using Equation 2.5 and Equation 2.6 respectively.

$$\begin{bmatrix} u \\ v \\ w \end{bmatrix} = J_1^{-1} \begin{bmatrix} \overline{x} \\ \overline{y} \\ \overline{z} \end{bmatrix} \tag{2.5}$$

$$\begin{bmatrix} p \\ q \\ r \end{bmatrix} = J_2^{-1} \begin{bmatrix} \dot{\phi} \\ \dot{\theta} \\ \dot{\psi} \end{bmatrix} \tag{2.6}$$

where, J_1^{-1} and J_2^{-1} are transformation matrices defined by Equation 2.7 and Equation 2.8 respectively. The transformation matrix, J_1^{-1}, projects the vector from earth-fixed to the ship-fixed reference system.

$$J_1^{-1} = \begin{bmatrix} \cos\psi\cos\theta & \sin\psi\cos\theta & -\sin\theta \\ -\sin\psi\cos\phi + \sin\phi\sin\theta\cos\psi & \cos\psi\cos\phi + \sin\phi\sin\theta\sin\psi & \sin\phi\cos\theta \\ \sin\phi\sin\psi + \cos\phi\sin\theta\cos\psi & -\sin\phi\cos\psi + \cos\phi\sin\theta\sin\psi & \cos\theta\cos\phi \end{bmatrix} \tag{2.7}$$

$$J_2^{-1} = \begin{bmatrix} 1 & 0 & -\sin\theta \\ 0 & \cos\phi & \sin\phi\cos\theta \\ 0 & -\sin\phi & \cos\theta\cos\phi \end{bmatrix} \tag{2.8}$$

2.2.3. *Forces and Moments*

As a pre-processing step, Usurp [36] is used to provide weights to each grid point to compute the area, forces, and moment accurately. As the flow solutions are available in the inertial frame system, the forces and moments are calculated in the inertial frame where the gravitational force acts vertically. In the inertial frame, forces are calculated as a summation of hydrostatic and piezometric pressure and viscous force. On integrating the elemental forces with the distance to the centre of gravity, the total moment is calculated [12]. The forces and moments are then projected to the ship-fixed system using Equation 2.9, where the propeller forces and moments are added. On integrating forces along the ship hull, appendages, and propeller, the forces (X, Y, Z are surge, sway, and heave forces) and moments (K, M, N are the roll, pitch, and yaw moment) are calculated in the ship-fixed reference system.

$$\begin{aligned} F &= J_1^{-1} F_e = \{X, Y, Z\} \\ O &= J_1^{-1} O_e = \{K, M, N\} \end{aligned} \tag{2.9}$$

2.2.4. *6 DOF Motions*

A predictor-corrector scheme is used to solve the equation of motions. As defined in Equation 2.10, the rigid body equations are framed on the assumption that the principal axes of inertia align with the ship's axis system. Solving Equation 2.10, the velocities are obtained in the ship-fixed reference system which is then projected onto the earth-fixed system to

obtain the rate of change of Euler angles and translations. Integrating them over time provides the new position and orientation of the ship. The new position and attitude from the motion solver along with the angular position of the rudder based on its controller are obtained. Accordingly, the grids are moved.

$$
\begin{aligned}
&m\left\{\frac{du}{dt}-vr+wq-x_G\left(q^2+r^2\right)+y_G\left(pq-\frac{dr}{dt}\right)+z_G\left(pr+\frac{dq}{dt}\right)\right\}=X\\
&m\left\{\frac{dv}{dt}-wp+ur-y_G\left(r^2+p^2\right)+z_G\left(qr-\frac{dp}{dt}\right)+x_G\left(qp+\frac{dr}{dt}\right)\right\}=Y\\
&m\left\{\frac{dw}{dt}-uq+vp-z_G\left(p^2+q^2\right)+x_G\left(rp-\frac{dq}{dt}\right)+y_G\left(rq+\frac{dp}{dt}\right)\right\}=Z\\
&I_x\frac{dp}{dt}+\left(I_z-I_y\right)qr+m\left\{y_G\left(\frac{dw}{dt}-uq+vp\right)-z_G\left(\frac{dv}{dt}-wp+ur\right)\right\}=K\\
&I_y\frac{dq}{dt}+\left(I_x-I_z\right)rp+m\left\{z_G\left(\frac{du}{dt}-vr+wq\right)-x_G\left(\frac{dw}{dt}-uq+vp\right)\right\}=M\\
&I_z\frac{dr}{dt}+\left(I_y-I_x\right)pq+m\left\{x_G\left(\frac{dv}{dt}-wp+ur\right)-y_G\left(\frac{du}{dt}-vr+wq\right)\right\}=N
\end{aligned}
\tag{2.10}
$$

where, (I_x, I_y, and I_z) are defined as the moment of inertia with respect to the centre of rotation, m being the mass of the ship, (x_G, y_G, and z_G) being the distance of centre of gravity from centre of rotation of the ship.

2.3. OSAKA UNIVERSITY PROPELLER MODEL

In this approach, the propulsion was incorporated into the simulation using a body-force propeller model, named the Osaka University propeller model that interactively works with CFDShip-Iowa V4.5. The model was developed at Toda lab, Osaka University. The model is based on quasi-steady blade element theory. As the propeller is replaced by a disk, detailed propeller modelling is not required. This reduces computational expense. The total output velocity predicted at the propeller plane by CFD is used to compute the propeller performance. The propeller thrust and torque are predicted using the total velocities and short period (blade to blade period) average. Using total velocities has its advantages, namely:

1. Eliminates the need for subtraction of induced velocity.
2. Free vortex is not assumed or fixed.

When the body force distribution based on the inviscid propeller code is used in the RANS solver to capture the hull-propeller interaction, the induced velocity is required to be subtracted from the total velocity. The body force distribution should converge in every time step, which necessitates multiple iterations per time step during the usual velocity-pressure

solver iteration. The induced velocity deduction is required because the effect of shed vortices is automatically accounted for by the body force field on the wing surface, etc. This effect is well explained by the linearized wing theory based on acceleration potential. If the pressure jump is specified on the wing surface in Euler equations of motion, the acceleration potential can be expressed by the doublet distribution (density is pressure jump) on the surface position. The integration of acceleration potential provides the velocity potential equation, expressed by the doublet distribution on the surface and wake surface. It means that if the pressure jump (body force distribution is embedded) is stated in the linearized Euler equation, the effect of the shed vortices on wake can be automatically accounted for. If the locally linearized RANS equation is considered, the vortices from the force distribution are observed to move with the local velocity and diffused by the viscous term. Therefore, both in the RANS solver and in the inviscid propeller code, induced velocity by shed vortices is computed. The induced velocity, thus, should be subtracted from the total velocity and then added in the inviscid propeller code, to consider the boundary condition, to obtain the force distribution. The basic idea of the Osaka University (OU) Propeller Model is that the induced velocity by automated shed vortices is not added in the inviscid propeller theory to obtain the force distribution by considering the boundary condition if the total velocity from the RANS code is used. So, any inviscid propeller code can be used similarly.

In this paragraph, the simple averaged body force in a short time (blade to blade time) based on the lifting line (blade element theory) is explained in uniform flow. First, the inviscid code in uniform flow with simple induced velocity computation is described. The induced velocity can be calculated as the function of circulation distribution. Here, the induced velocity is calculated in a time-averaged manner or by an infinite blade assumption. For example, (refer to Figure 2.2), the induced velocity components in the axial direction (u_{ip}) and the tangential direction ($v_{\theta ip}$) in uniform flow can be expressed by Equation 2.11.

$$u_{ip} = \frac{N_p \Gamma(r,\theta)}{4\pi h}, \quad v_{\theta ip} = \frac{N_p \Gamma(r,\theta)}{4\pi r}, \quad H_p = 2\pi h \tag{2.11}$$

where. $\Gamma(r)$ is the circulation at radius = r, N_p is the number of blades of the propeller, H_p is the pitch of helical vortex, h is the advancing distance for one radian of helical vortex, and (r,θ) represents the polar coordinates of the origin of propeller centre.

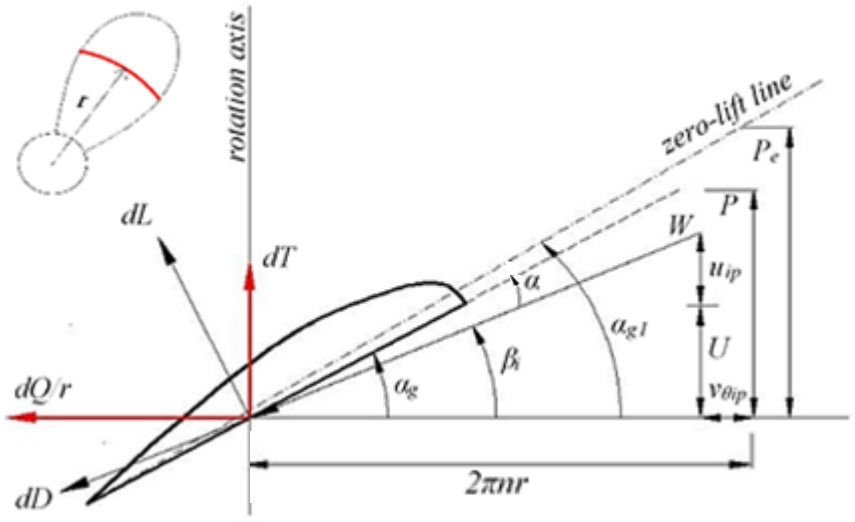

Figure 2.2 Blade element for inviscid code.

Computing the lift force (L_f) acting on the blade element using the two methods shown in Equation 2.3.2, the fundamental equation of circulation can be formulated. Many corrections (finite number of the blades, blade to blade interaction: cascade effect and tip effect, and so on) are used in real theory. Here, the simplest expression is shown for better understanding.

$$L_f = \rho W \Gamma = \frac{1}{2}\rho W^2 c 2\pi \sin\alpha \tag{2.12}$$

$$\Gamma = \pi W c \sin\alpha \tag{2.13}$$

where, α is the angle of attack, ρ is the fluid density, W represents the total inflow velocity, c is the chord length and $2\pi sin\alpha$ is the lift coefficient.

Using Figure 2.2 and Equations 2.11 to 2.13, Equations 2.14 and 2.15 can be formulated to compute the circulation.

$$\begin{aligned} W\sin\alpha &= W\sin(\alpha_g - \beta_i) \\ &= W\sin\alpha_g\cos\beta_i - W\cos\alpha_g\sin\beta_i \\ &= (2\pi nr - v_{\theta ip})\sin\alpha_g - (U + u_{ip})\cos\alpha_g \end{aligned} \tag{2.14}$$

$$where,\ \cos\beta_i = \frac{2\pi nr - v_{\theta ip}}{W},\ \sin\beta_i = \frac{U + u_{ip}}{W}$$

$$\begin{aligned} \Gamma &= \pi c(2\pi nr - v_{\theta ip})\sin\alpha_g - \pi c(U + u_{ip})\cos\alpha_g \\ &= \pi c(2\pi nr - \frac{N\Gamma}{4\pi r})\sin\alpha_g - \pi c(U + \frac{N\Gamma}{4\pi h})\cos\alpha_g \end{aligned} \tag{2.15}$$

where, n is the number of propeller revolutions, α_g is the geometric pitch angle (mathematically determined as Equation 2.16), α_{gI} represents the effective pitch angle (mathematically expressed as Equation 2.17), P stands for the geometric propeller pitch and P_e is the effective propeller pitch.

$$\tan \alpha_g = \frac{P}{2\pi r} \tag{2.16}$$

$$\tan \alpha_{g1} = \frac{P_e}{2\pi r} \tag{2.17}$$

Once the circulation is computed, the lift force is obtained. If the above equations are used, the induced velocity should be subtracted to acquire effective inflow. The effective inflow should be used to obtain the thrust and torque. But for uniform flow, effective inflow is the same as nominal inflow since the vortices do not exist. Sometimes converged effective inflow is slightly different from the nominal wake for uniform flow due to the difference of induced velocity in the propeller code and RANS solver. Therefore, in the OU propeller model (refer to Figure 2.3), the total velocity is used to obtain the force distribution.

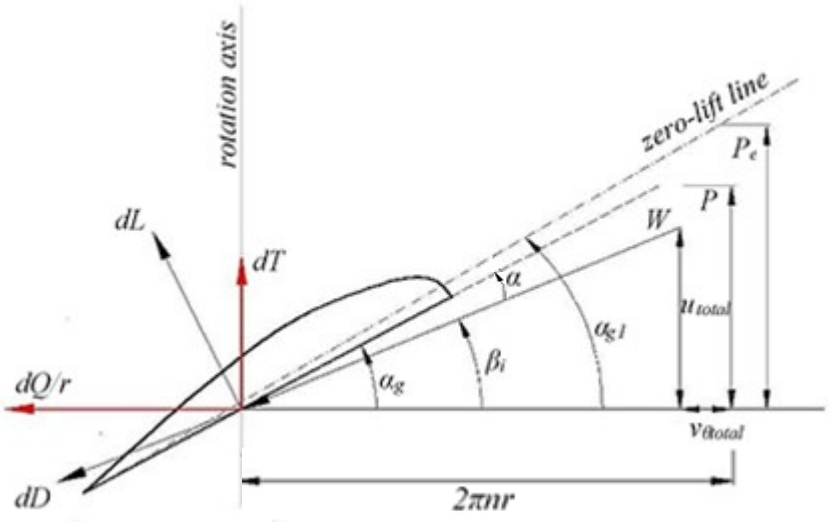

Figure 2.3 Blade element using total velocity.

The segmental lift (dL) and drag (dD) are expressed as Equation 2.18. The drag force is added similarly to the inviscid propeller code. The segmental thrust (dT) and torque (dQ) are computed using Equation 2.19 and 2.20 respectively

$$dL = \frac{1}{2}\rho W^2 c 2\pi \sin\alpha \quad \left(\alpha = \alpha_{g1} - \beta_i\right)$$

$$\tan\beta_i = \frac{u_{total}}{2\pi nr - v_{\theta total}} \tag{2.18}$$

$$dD = \frac{1}{2}\rho W^2 c C_D \quad \left(\text{drag coefficient}, C_D = 0.01\right)$$

$$dT = dL\cos\beta_i - dD\sin\beta_i \tag{2.19}$$

$$dQ = (dL\sin\beta_i + dD\cos\beta_i)r \tag{2.20}$$

The total velocity (u_{total} and $v_{\theta total}$) can be determined by rotating force distribution and the forces can be calculated using equations presented in Hasegawa *et al*. [37] that implement the rotating lifting line theory. In uniform flow, u_{total} and $v_{\theta total}$ can be expressed as $U+u_{ip}$ and $v_{\theta ip}$ respectively. When the propeller inflow velocity field is not axisymmetric or unsteady, the quasi-steady assumption is used. The total velocities can be expressed by Equation 2.21. *e* stands for effective velocity.

$$\begin{aligned} u_{total} &= u_e(r,\theta) + u_{ip} \\ v_{\theta total} &= v_{\theta e}(r,\theta) + v_{\theta ip} \end{aligned} \tag{2.21}$$

In order to obtain the short-term (blade to blade) averaged force, the pressure jump at the fixed space point is averaged. First, the pressure jump in the x-direction (Δp(t, y, z)) is projected to the propeller plane (Δp(t, r, θ)). Thus, the pressure jump exists in the propeller plane. This can be expressed mathematically by Equation 2.22. If the point is outside the propeller circle, the pressure jump is zero.

$$\begin{aligned} &\Delta p(t,y,z) = \Delta p(t,r,\theta) \\ &\quad \text{if } r_B \le r \le R \qquad r = \sqrt{y^2+z^2} \;\; \cos\theta = \frac{y}{r} \;\; \sin\theta = \frac{z}{r} \end{aligned} \tag{2.22}$$

At the fixed special point, the pressure jump is averaged over the blade to blade time using Equation 2.23. *SA* stands for short-term average.

$$\Delta p_{SA}(y,z) = nN_p \int_{t_1}^{t_1+\frac{1}{nN_p}} \Delta p(t,y,z)dt \tag{2.23}$$

The time integration can be changed to rotating angle integration if the rotating velocity is constant and the average pressure is considered, as shown in Equation 2.24. The blade coordinate and rotating angle of the generator line is presented in Stern *et al*. [38].

$$\begin{aligned}
&\Delta p(average) = nN_p \int_{t_1}^{t_1+\frac{1}{nN_p}} \Delta p(t,y,z)dt \\
&\Delta p(t,y,z) = \Delta p(r,\varphi,\theta_p) \quad \varphi = \theta - \theta_p \\
&\Delta p(r,\varphi,\theta_p) = 0 \qquad\qquad if\ \varphi_{TE} \le \varphi \le \varphi_{TE}
\end{aligned} \tag{2.24}$$

where, θ_p is the angular position of the generator line and φ represents the angle from the generator line on the projected blade.

Thus, the short-term averaged pressure jump at a fixed point (Δp_{SA} (t, y, z)) can be calculated using Equation 2.25.

$$\begin{aligned}
\Delta p_{SA}(t,y,z) &= \frac{1}{\frac{2\pi}{N_p}} \int_{\theta-\frac{\pi}{N_p}}^{\theta+\frac{\pi}{N_p}} \Delta p(r,\varphi,\theta_p)d\theta_p \\
&= \frac{1}{\frac{2\pi r}{N_p}} \int_{\theta-\theta_{LE}}^{\theta+\theta_{TE}} \Delta p(r,\varphi,\theta_p) r d\theta_p \\
&\approx \frac{1}{\frac{2\pi r}{N_p}} \int_{-\theta_{LE}}^{\theta_{TE}} \Delta p(r,\varphi,\theta_p) r d\theta_p \\
&= \frac{N_p}{2\pi r} dT(r,\theta)
\end{aligned} \tag{2.25}$$

The approximation in Equation 2.25 is valid for small expanded area ratio propellers such as KVLCC2 propeller or JBC propeller. Consequently, Hasegawa *et al*. [37] used the rotating body force distribution for KCS and obtained better results. However, for the purpose of this study, the averaged model was used as a shorter computational time is desired for maneuvering computation. As the blade frequency is considered much higher compared to maneuvering motion, the short-term averaged body force is observed to show the trend of special distribution of body force. The body force distribution (F_{bx}, F_{by}, F_{bz} are body forces in x, y, and z-direction, respectively) at the propeller plane is obtained using Equation 2.26-2.28.

$$F_{bx} = \frac{N_p}{2\pi r \Delta x} dT(r,\theta) \tag{2.26}$$

$$F_{by} = \frac{dQ\cos\theta}{2\pi r^2 \Delta x} \tag{2.27}$$

$$F_{bz} = \frac{dQ\sin\theta}{2\pi r^2 \Delta x} \tag{2.28}$$

where, Δx is the grid spacing in the axial direction

The force distributions are specified in the RANS solver as source terms in the momentum equation. The total velocities are calculated using the RANS solver and iterated during every time step in CFD computation. The integrated thrust (T) and torque (Q) in x, y, and z-direction are computed using the individual contribution of each body force element.

As stated at the beginning, any other inviscid code can be modified by removing the induced velocity subroutine. Although the computation load increases, the boundary layer on the blade surface is not required to be solved using a very fine resolution. Thus, in addition to being cost-effective for an end-to-end maneuvering simulation, the OU propeller model is effective in predicting propeller performance in unsteady or asymmetric flow. The model has been extensively validated for 2DOF motions in the previous work [29, 30, 39].

CHAPTER 3

GEOMETRY AND TEST CONDITIONS

3.1. GEOMETRY

The present study was conducted on KRISO Container Ship (KCS). The benchmark geometry, KCS, has been used at various international workshops such as SIMMAN 2008, 2014, and 2019, and A Workshop on CFD in Ship Hydrodynamics: Gothenburg (G2010) and Tokyo 2015 (T2015) for computational validation. The lines plan of KCS along with the propeller is shown in Figure 3.1. The principal characteristics of KCS at full scale, IIHR, OU, and CFD models are placed in Table 3.1.

The similarity in test conditions across facilities is desired. In this present study, as mentioned in Table 3.1, the values are close to each other. In most aspects, experimental data from IIHR, The University of Iowa was used in the computations for direct comparison.

Five bladed, single screw, clockwise rotating propeller KP505 propeller, as recommended by KRISO, was used. The propeller centre was positioned along x-direction at $p_x/L=0.9825$ (from the fore perpendicular) and along z-direction at $p_z/L=0.02913$ (below the waterline). A rotating hub was not included in the computations.

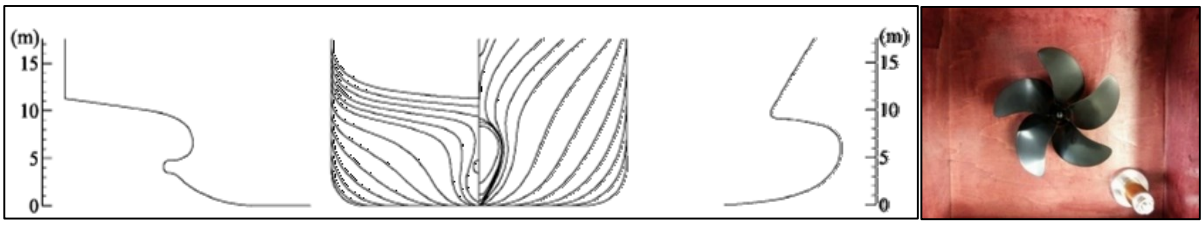

Figure 3.1 KCS model geometry with propeller.

Semi-balanced horn type rudder with its rotational axis positioned in the x-direction at $r_x/L=1.00$ was used. The rudder consists of two parts: fixed and movable. The fixed portion is attached to the bare hull and is not allowed to move. The movable part of the rudder is allowed to rotate along its vertical axis. The rate of rudder turn was maintained at a value of 21.5deg/s (model scale) same as the IIHR, The University of Iowa experiments unless otherwise mentioned. The maximum rudder angle deflection was limited to 35°. To reduce

Table 3.1 Main particulars of KCS with its appendages

Parameter	Full Scale	IIHR	OU-EFD	OU-CFD
Hull Particulars				
Scale: λ_s	1	85.19	71.88	85.19
Length b/w perpendiculars: L [m]	230.0	2.7	3.2	2.7
Depth: D_t[m]	19	0.223	0.264	0.223
Beam: B [m)	32.2	0.378	0.448	0.378
Draft: T_d [m] full loaded condition	10.8	0.127	0.150	0.127
Displacement: ∇ [m^3]	52030	0.0842	0.140	0.0842
Block coefficient: C_B	0.651	0.651	0.651	
Test Conditions				
Wetted area without rudder: A_W/L^2	0.1802	0.1802	0.1802	0.1805
Longitudinal centre of gravity: LCG/L (from Fore Perpendicular)	0.5148	0.5148	0.5147	0.5152
Vertical Centre of Gravity: KG/L (from keel)		0.0623	0.0622	0.0623[(a)]
X axis radius of gyration: K_{XX}/B	0.40	0.39	0.40	0.39[(a)]
Y axis radius of gyration: K_{YY}/L	0.25	0.25	0.25	0.25[(a)]
Z axis radius of gyration: K_{ZZ}/L	0.25	0.25	0.25	0.25[(a)]
Propeller particulars (KP505)				
Type	Fixed Pitch	Fixed Pitch	Fixed Pitch	Fixed Pitch
Diameter [m]: D_P	7.9	0.093	0.11	0.093
Pitch ratio (P/D_p) (0.7R)	0.997	0.997	0.997	0.997
Section	NACA66	NACA66	NACA66	NACA66
Expanded blade area ratio (ER)	0.80	0.80	0.80	0.80
Rotation Direction (from Stern to bow)	Clock-wise	Clock-wise	Clock-wise	Clock-wise
Boss ratio	0.18	0.18	0.18	0.18
Number of blades: N_p	5	5	5	5
Propeller centre along x-direction (from Fore Perpendicular): p_x/L	-	0.9825	0.9825	0.9825
Propeller centre along z-direction (below waterline.): p_z/L	-	-0.02913	-0.02913	-0.02913
Rudder				
Type	Horn	Horn	Spade	Horn and Spade
Wetted area of rudder [m^2]	115	0.0158	0.0223	
Lateral area of rudder [m^2]	54.45	0.0075	0.0105	
Maximum rate of rudder turn [deg/s]	2.32	21.5	-	21.5
Rudder axis along x-direction: r_x/L	1.00	1.00	1.00	1.00
Ship Speed				
Ship speed in x-direction [m/s]: U	12.35	1.34	1.456	1.34
Froude Number (Fn)	0.26	0.26	0.26	0.26
Reynolds Number (Rn)[(b)]	2.84×10^9	3.61×10^6	4.66×10^6	3.61×10^6

[(a)] Experimental data from IIHR, The university of Iowa was used.
[(b)] Reynolds Number is calculated using U and L

modelling and computational expense, a simplified spade rudder was also generated. To analyse the effect of rudder modelling, both the rudder systems were used in the computations.

3.2. SIMULATION TEST MATRIX

The free-running experiments were conducted at IIHR, The University of Iowa for a target Froude number (Fn) of 0.26 and Reynolds Number (Rn) of 3.61×10^6. The details of the experimental setup along with the obtained data are presented in [20] and [21]. Experiments were also conducted at Osaka University to analyse the added powering requirements of 3.2m KCS model along with flow field velocity measurements using Stereo Particle Image Velocimetry (SPIV) for calm water and head waves. The detailed OU experimental setup is presented in [30]. The summary of all simulated conditions, as recommended in [40], are listed in Table 3.2. The cases include:

Case 1: Self-propulsion under course-keeping control in calm water;

Case 2: Turning circle maneuver in calm water;

Case 3: Zigzag maneuver in calm water

Case 4: Self-propulsion under course-keeping control in head waves

The simulations were compared with experimental data from IIHR, The University of Iowa, and the flow field data was compared with SPIV data from Osaka University.

Table 3.2 OU-CFD Test Matrix

Test	DOF	Fn	Rn	H/λ	λ/L	χ [deg]	δ [deg]	Ψ_T [deg]
Calm water								
Self-Propulsion with Course Keeping	6	0.26	3.61×10^6	-	-	-	PID control	0
Turning circle	6	0.26	3.61×10^6	-	-	-	35	NA
							-35	
Zigzag Maneuver	6	0.26	3.61×10^6	-	-	-	10	10
							-10	10
							20	20
							-20	20
Head Wave								
Self-Propulsion with Course Keeping	6	0.26	$3.61x10^6$	1/60	0.65	0	PID control	0
					1.00			
					1.15			
					1.37			

δ: Rudder angle , ψ_T: Target yaw angle,
χ: Encounter angle, λ: Wavelength, H:Wave Height

CHAPTER 4

GRID SYSTEMS

4.1. GRID GENERATION

With a Finite Difference Method, the partial differential equations are approximated into algebraic equations requiring the flow domain to be discretized. Proper discretization is the first step to avoid large numerical errors and is fundamentally an engineering judgement. Various factors are taken into consideration at the discretization stage such as element size, number of elements, types of elements, and simplification of the physical geometry. When dealing with complex geometries of rudder, bulbous bow, and stern, domain extrusion is a bottleneck. To overcome the difficulties in grid generation, several simple overlapping grids are used to decompose the complex geometry. The technique is known as the multi-block overset grid technique and it increases the flexibility in grid generation. The multi-block overset gridding technique allows for local refinement wherever needed.

In this research, the generation of the grid was executed using Gridgen V15 – Pointwise [41]. The grid set was arranged in a regular pattern i.e., structured grid. To account for the asymmetry introduced by the propeller and moving rudder, the entire ship (port and starboard) along with its computational domain was modelled. A curvilinear structured grid was used for the solid surfaces (O-grid topology). Cartesian grid (H-H grid topology) was used to resolve the flow far from the hull with a refinement block closer to the hull.

In this study, two grid systems, G1 and G2, were generated as shown in Figure 4.1-A1 and Figure 4.1-A2, respectively. Grid system G1 was generated using the original semi-balanced horn rudder geometry (see Figure 4.1-B1) as recommended in [19] and [40]. The original rudder geometry is complicated and leads to multiple bottlenecks in the extrusion stage. To increase the flexibility in grid generation, the rudder grid was broken down into multiple simpler grids. Separate processors were allocated to each block of the rudder grid, leading to higher computational expense. To reduce this computational expense, grid stem G2 was generated using a simplified spade rudder (see Figure 4.1-B2). 38 grids required to define the rudder geometry in G1 were reduced to only 2 grids in the G2 system.

In connection with grid system G1, six blocks with independent grids for the bare hull, rudder-fixed, rudder-movable, propeller, refinement (ship and wake), and background were generated. Each block is comprised of multiple smaller blocks of grids. The details of each grid part are listed in Table 4.1. The ruder geometry was divided into two blocks, namely, rudder-fixed and rudder-movable. Local refinement (refinement 1-6) was also modelled for the rudder gap to provide smoother connectivity between the fixed and movable portions of the rudder. The adopted overset grid topology at the solid surface, for the grid system G1, is shown in Figure 4.2. The same grid combination of G1 was used for all the cases defined in Chapter 3 except for the background grid. The number of grid points for each wave condition was modified in all three directions to better resolve the wave. The total number of grid points, for Case 1-3 (defined in Chapter 3), was around 10.8 million. In the case of course-keeping studies in waves, the total number of grid points was 21.9million, 13.7 million, 13.7 million, and 12.5million for λ/L=0.65, 1.00, 1.15, and 1.37 respectively. Grid system G1 (except the propeller and background block) was modelled by IIHR, The University of Iowa [42].

In grid system G2, six blocks with independent grids for boundary layer (hull and its cover), hub, rudder, propeller, wake refinement, and background, were used to describe the geometry and the domain. The adopted overset grid topology at the solid surface, for the grid system G2, is shown in Figure 4.3. The rudder block was further subdivided into two blocks rudder-body block and a small overlapping region on the top known as the rudder-cover block. The total grid number was around 14 million across all the free-running simulations. The details of each grid part are listed in Table 4.2.

In both the grid systems, the wake refinement block was positioned at the stern of the hull to better resolve the vortical structures and flow features and capture the interaction of the hull-propeller-rudder critical to maneuvering and course-keeping studies. An additional ship refinement block was also modelled, for grid system G1, to provide higher resolution for the free-surface. This facilitated the usage of a coarser background block. The five-bladed propeller was transformed into a disk conforming to the propeller model explained in the following chapter. Detailed propeller modelling was not required. $y+\leq 1$ was achieved by limiting the minimum size of the grid at 1×10^{-6} normal to the surface. In course-keeping studies in waves, to capture the propagating waves, 20-25 grid points per wave amplitude and 65-195 grid points per λ/L were used in grid system G2.

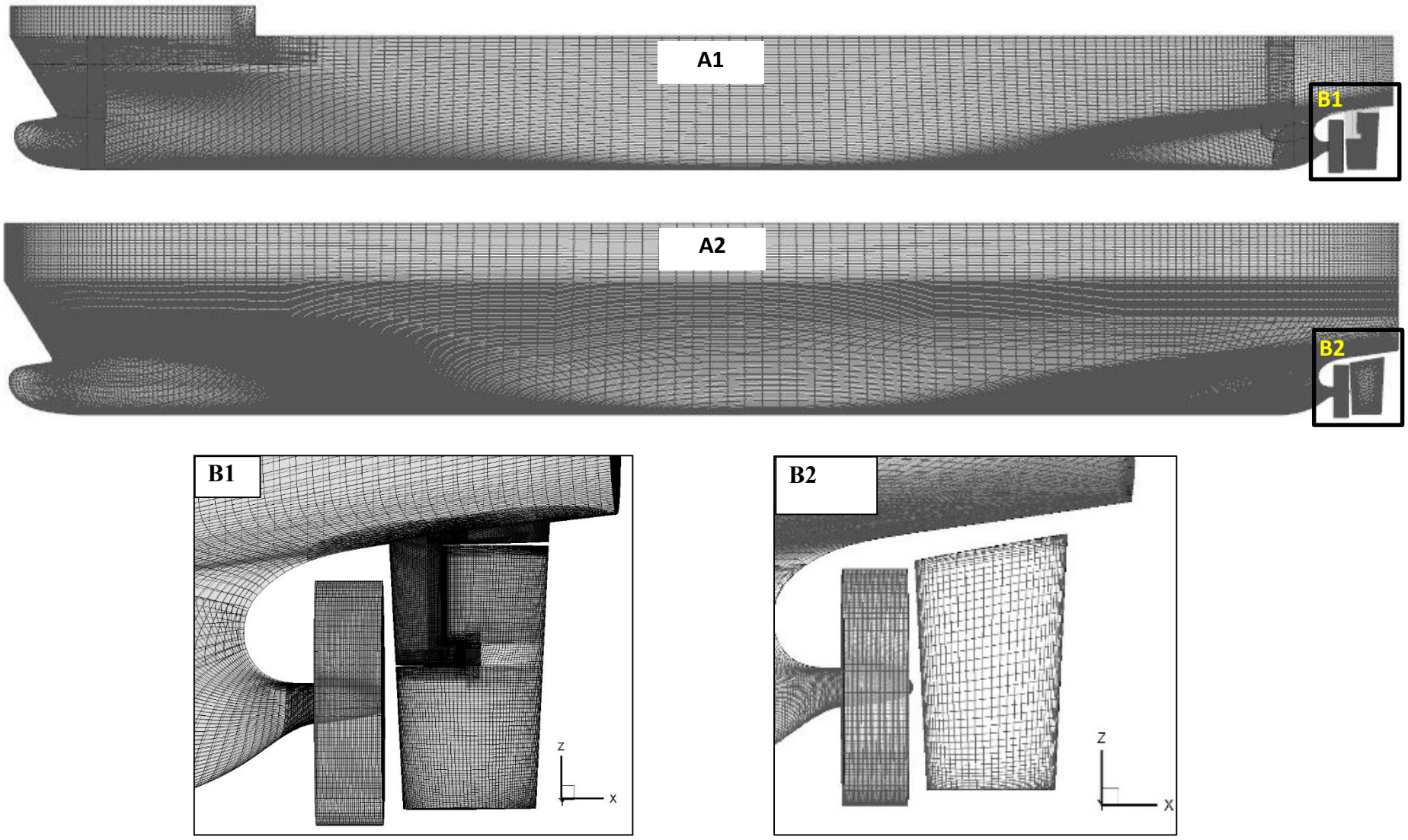

Figure 4.1- A1: Surface grid of bare hull for grid system-G1; A2: Surface grid of bare hull for grid system-G2
B1: Enlarged view of Grid system G1 showing original underhung rudder geometry.
B2: Enlarged view of Grid system G2 showing simplified rudder geometry.

Table 4.1 Details of grid system-G1

Block Name		Topology	$i_{max} \times j_{max} \times k_{max}$	Level
Bare Hull	Mid	O-grid	126×47×105×(2)*	Parent
	Wave Break		97×46×43×(2)*	
	Bow Upper		36×49×58×(2)*	
	Bulbous bow		36×47×483×(2)*	
	Stern		41×48×75×(2)*	
	Stern Cap		17×49×75×(2)*	
	Stern Cap cover		26×49×26×(2)*	
	Hub		26×44×51×(2)*	
	Hub Cap		34×40×61×(2)*	
	Hub Cap cover		16×33×26×(2)*	
Rudder-Fixed	Front	O-grid	37×38×92×(2)*	
	Back Upper		61×34×52×(2)*	
	Mid		35×38×126×(2)*	
	Mid Upper		26×38×30×(2)*	
	Down		91×38×38×(2)*	
	Down Upper		41×26×35×(2)*	
	Refinement 1	H-grid	71×29×29×(2)*	
	Refinement 2		29×29×71×(2)*	
	Refinement 3		35×29×29×(2)*	
Rudder-Movable	Upper	O-grid	81×41×46×(2)*	Child
	Upper 2		81×41×31×(2)*	
	Down		66×40×56×(2)*	
	Mid		47×43×28×(2)*	
	Mid Front		36×37×39×(2)*	
	Mid Front Upper		66×30×36×(2)*	
	Mid Front Down		81×27×36×(2)*	
	Refinement 4	H-grid	42×57×57×(2)*	
	Refinement 5		42×57×51×(2)*	
	Refinement 6		41×57×57×(2)*	
Propeller		O-grid	35×111×105	Parent
Refinement	Wake	H-grid	128×72×126	
	Ship		158×66×161	Root (surge, sway and yaw only)
Background	Calm Water	H-grid	125×181×151	
	λ/L=0.65		385×273×117	
	λ/L=1.00		219×157×117	
	λ/L=1.15		219×157×117	
	λ/L=1.37		183×131×117	

* represents port and starboard

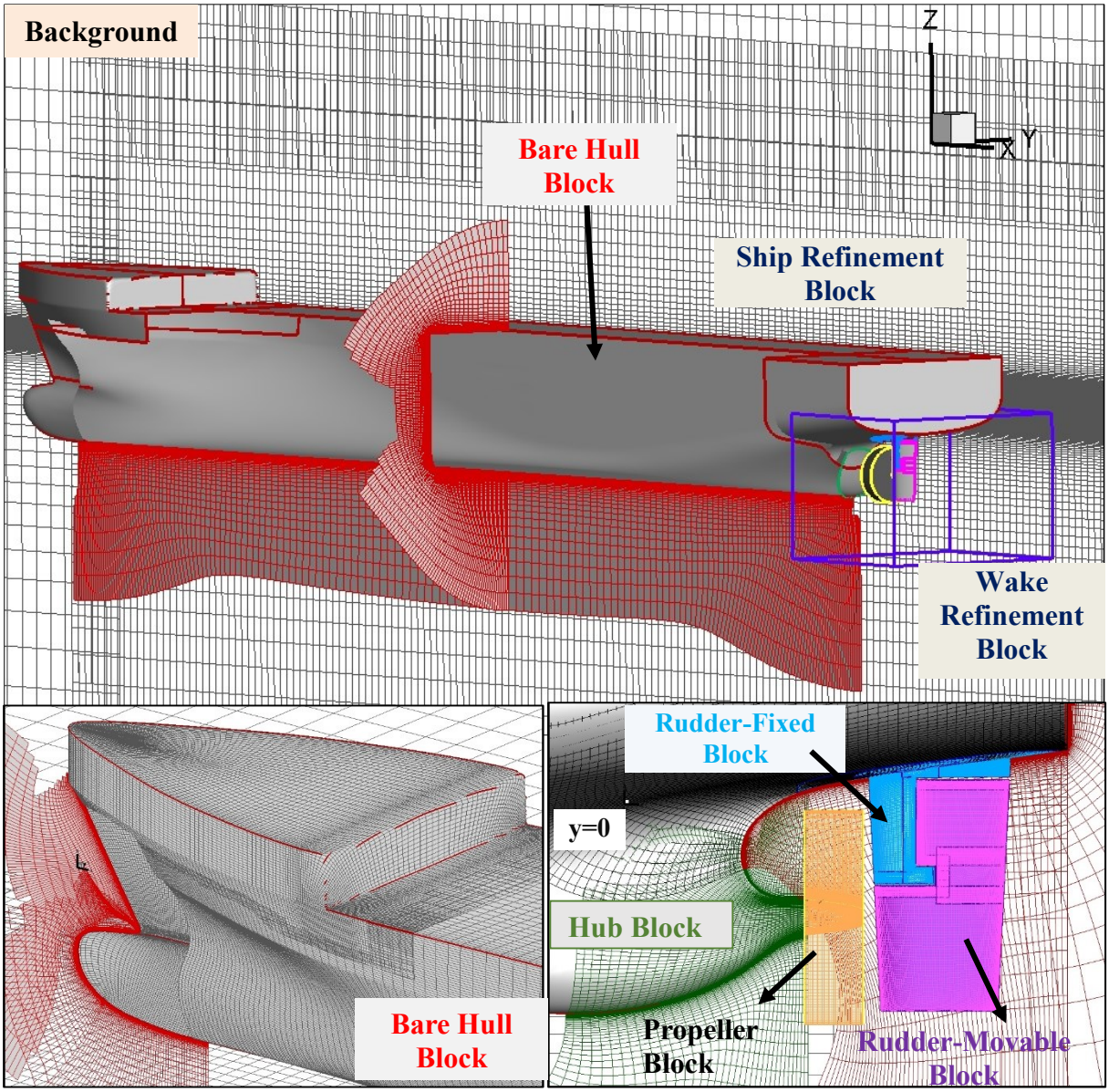

Figure 4.2 Overset grid system-G1, six blocks: bare hull, rudder-fixed, rudder-movable, propeller, refinement and background.

4.2. HIERARCHY OF OVERSET GRID

An overset grid with a hierarchical relationship was used at runtime. Grids defining the geometry and the refinement were translated and rotated according to the 6DOF solutions and formed the parent level for the motions. The rudder was treated as a child to the ship grids. It followed the ship but was permitted to rotate about an axis fixed on the ship according to the heading controller. The background grid (root level) connecting the ship to the boundary condition followed the ship but was restricted in its heave, pitch, or roll motions. This enabled to maintain the free surface horizontally. The detailed hierarchy of each grid is listed in Table 4.1 and Table 4.2.

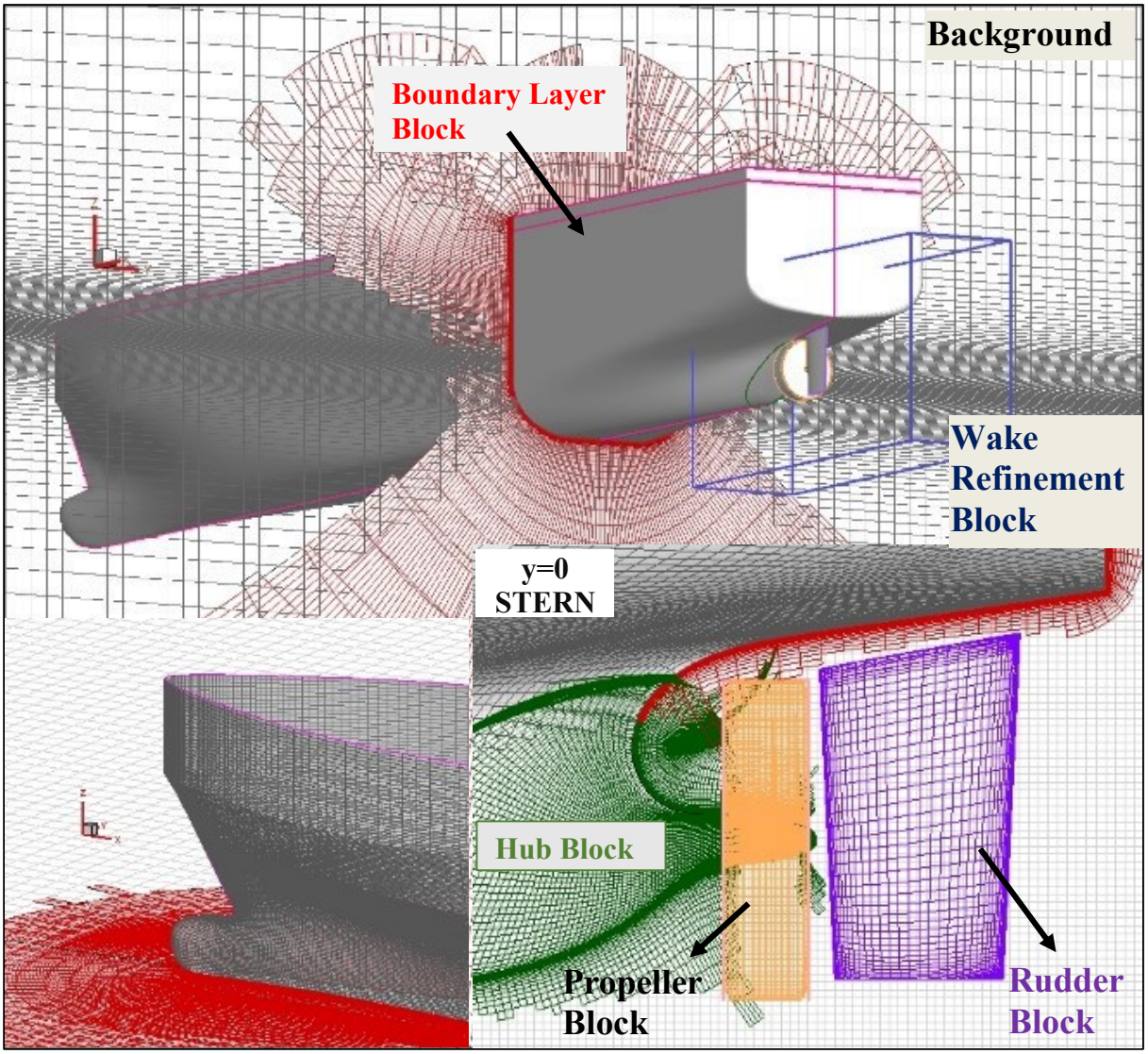

Figure 4.3 Overset grid system-G2, six blocks: boundary layer, hub, propeller, rudder, wake refinement and background.

Table 4.2 Details of grid system-G2

Block Name		Topology	$i_{max} \times j_{max} \times k_{max}$	Level
Boundary Layer	**Hull**	O-grid	206×61×141×(2)*	Parent
	Cover	O-grid	206×30×25×(2)*	
Hub		O-grid	101×41×51×(2)*	
Rudder	**Body**	O-grid	85×64×53	Child
	Cover	O-grid	85×44×21	
Propeller		O-grid	35×111×105	Parent
Wake Refinement		H-grid	201×81×141	Parent
Background		H-grid	253×181×151	Root
Total grid number			**14,260,143**	

* represents both port and starboard

CHAPTER 5

SIMULATION DESIGN

5.1. Computational Domain and Boundary Conditions

The computational domain requires to envelop the flow field (covering both port and starboard) around the whole hull as the flow is asymmetric due to maneuvering motions. Therefore, fore perpendicular (FP) was located at (0,0,0) and the aft perpendicular (AP) at (1,0,0). Figure 5.1 and Figure 5.2 show the computational domain along with the applied boundary conditions for grid systems G1 and G2 respectively. The adopted computational domain was a single block H-H topology rectangular box defined using six boundaries: inlet plane, outlet plane, top plane, bottom plane and the two side planes.

In the case of simulations with grid system G1, the inlet and outlet plane were positioned at 1.2*L* ahead of FP and 2.0*L* behind AP. In order to minimize blockage in the lateral flow, the side boundaries were placed at 1.5*L* from the centreline of the hull. In the vertical direction, the domain extended from z=-1.5*L* to 0.5*L* with the free surface located at z/L=0.

On the other hand, for simulations with grid system G2, the domain extended from x=-0.6*L* to 2.4*L* from F.P. in the longitudinal direction. The side boundaries were located at 1.1*L* away from the centerline of the hull. The top and bottom planes of the domain were positioned equidistantly at 0.8*L* from the free-surface set at *z/L*=0.

Inlet and outlet boundary conditions followed the upstream and downstream planes of the domain respectively. Zero gradient boundary condition was imposed on the side boundaries of the domain. The far-field boundary condition was applied on the top and bottom planes of the domain. No-slip boundary condition was exercised on the ship hull and its appendages. In wave condition (case 4), for grid system G1, all the boundaries of the domain were changed to wave boundary condition. On the other hand, for grid system G2, only the inlet boundary condition was changed to wave generation boundary (case 4). The details of the various boundary condition used in this study are described in Table 5.1.

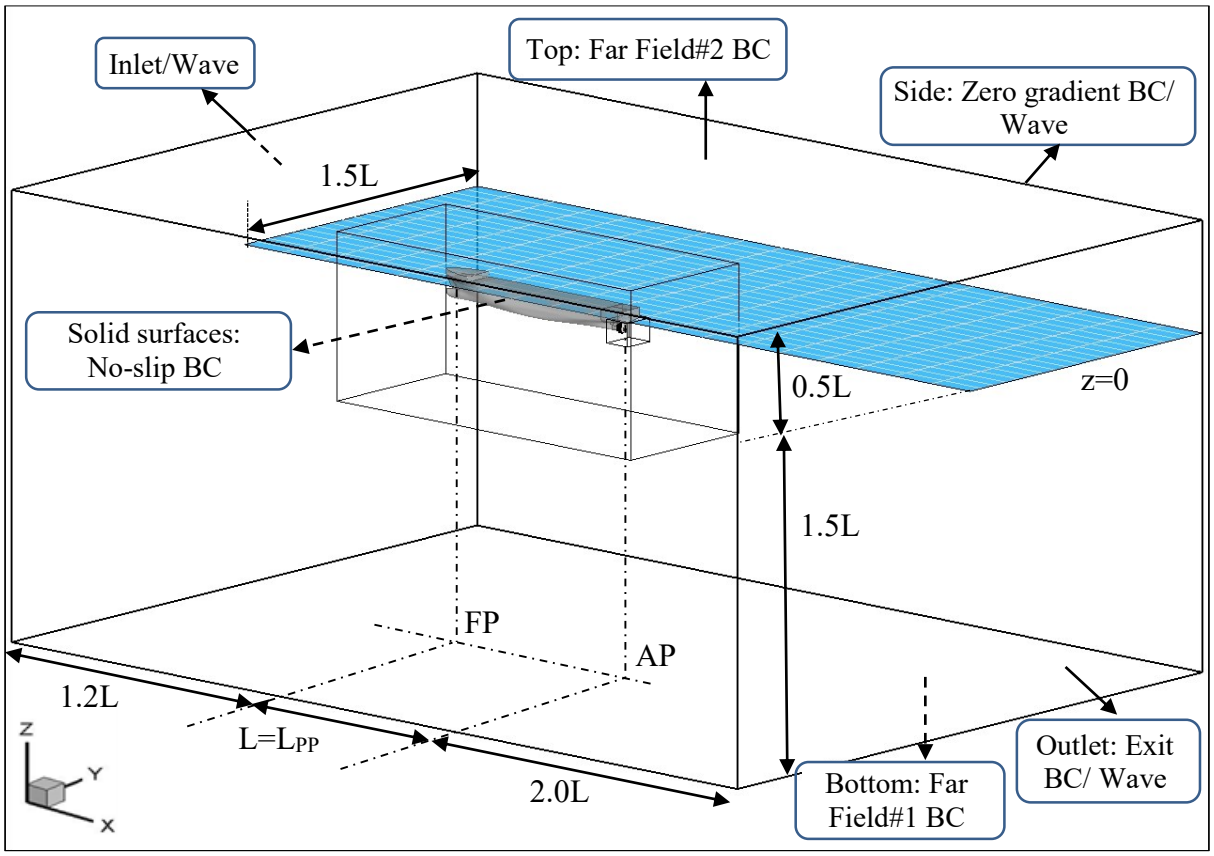

Figure 5.1 Adopted computation domain along with imposed boundary conditions for grid system G1.

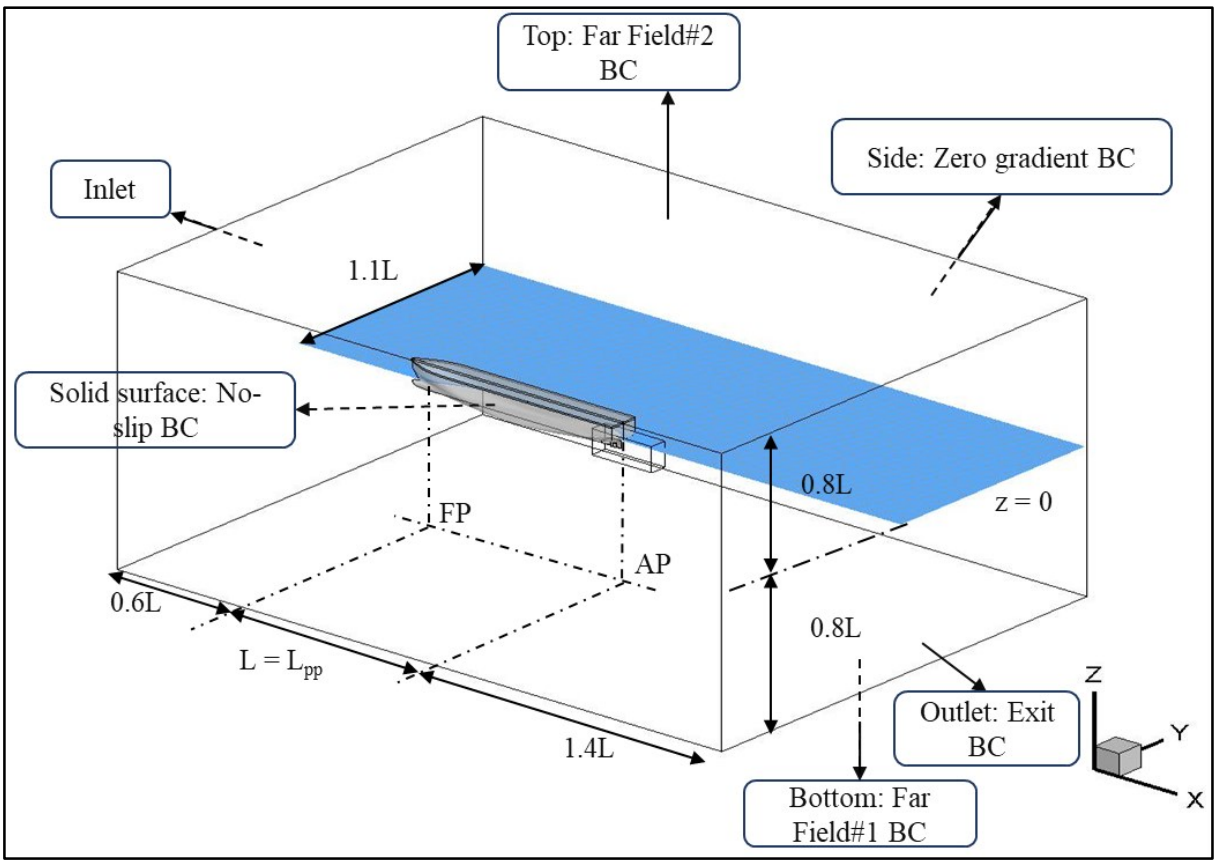

Figure 5.2 Adopted computation domain along with imposed boundary conditions for grid system G2.

Table 5.1 Detailed Boundary conditions [31]

Type	***u***	***v***	***w***	***p***	k_t	ω_t	v_t	ζ
Inlet	u_∞	v_∞	w_∞	$\partial p=0$	0	0	0	0
Exit	$\partial^2 u=0$	$\partial^2 v=0$	$\partial^2 w=0$	$\partial p=0$	$.\partial k=0$	$\partial\omega=0$	$\partial v_t=0$	0
Zero gradient	$\partial u=0$	$\partial v=0$	$\partial w=0$	$\partial p=0$	$\partial k=0$	$\partial\omega=0$	$\partial v_t=0$	0
Far field #1	u_∞	$\partial v=0$	$\partial w=0$	0	$\partial k=0$	$\partial\omega=0$	$\partial v_t=0$	0
Far field #2	u_∞	v_∞	w_∞	$\partial p=0$	$\partial k=0$	$\partial\omega=0$	$\partial v_t=0$	0
No-slip	0	0	0	$\partial p=0$	0	$\frac{60}{Rn\beta\Delta y^2}$	0	0
Wave	Equation 5.2	0	Equation 5.3	Equation 5.4	0	0	0	Equation 5.1

ζ represents the wave elevation;
u, v, w: velocity component in *x*-direction, *y*-direction and *z*-direction respectively;
u_∞, v_∞, w_∞: Free-stream velocity component in *x*-direction, *y*-direction and *z*-direction respectively;
p: Pressure:
k_t: Turbulent kinetic energy; ω_t: Specific dissipation rate; v_t: Eddy viscosity

The applied wave boundary condition is calculated from the linear potential flow solution [43].

$$\zeta(x,t) = A\cos(kx - \omega t + \gamma) \tag{5.1}$$

$$u(x,z,t) = \omega A e^{kz}\cos(kx - \omega t + \gamma) \tag{5.2}$$

$$w(x,z,t) = \omega A e^{kz}\sin(kx - \omega t + \gamma) \tag{5.3}$$

$$p(x,z,t) = \frac{\omega^2 A e^{kz}}{k}\cos(kx - \omega t + \gamma) - \frac{\omega^2 A^2 e^{2kz}}{2} \tag{5.4}$$

where, A is the wave amplitude, $k=2\pi/\lambda$ is the wave number, ω is the wave frequency.

5.2. NUMERICAL SCHEMES

To transform governing equations from physical space to computational space, 2nd order finite difference method with a fully structured grid was used. The second-order backward

Euler differencing scheme was used to discretize the temporal terms in momentum and turbulent equations. The second-order central differencing scheme was applied to viscous or diffusive terms. In case of computations with grid system G1, fourth-order and second-order upwind scheme were used to discretize convective terms in momentum equation and level-set respectively. On the other hand, the second-order upwind method was used to discretize convective terms in both momentum equations and level-set for the computations with grid system G2. The convective terms in turbulent equations were discretized with second-order upwind scheme for computations with both grid systems.

6DOF rigid body equations of motions were solved for this study. The turbulence model used was blended k-ω/k-ε SST with no wall function. The free surface was modelled using single phase level-set method. The coupling of velocity and pressure was achieved by the two-step Projection method effectively using the PETSc toolkit. Inner iterations for each time step were maintained between a minimum of three to a maximum of five. To analyse the convergence of solutions, computations with grid system G1 were performed with tolerances of $1.0e^{-5}$, $1.0e^{-6}$, 1.0^{-6}, and $1.0e^{-3}$ for velocities, pressure, level set, and non-linear iterations respectively. On the other hand, tolerances used for velocities, pressure, level set, and non-linear iterations were $1.0e^{-5}$, $1.0e^{-6}$, $1.0e^{-5}$, and $5.0e^{-4}$ respectively for computations with grid system G2. The time step (Δt) used in the simulations was 0.0025.

In the present moving body application, overset assembly and interpolation were performed at each time step. To obtain the DCI information at run time, the Suggar++ library [44,45] was used. In the present work, the MPI library bridged the communication gap between Suggar++ and overset compatible solver, CFDShip-Iowa V4.5 for DCI exchange.

5.3. CONTROLLERS

Proportional-Integral-Derivative (PID) controller was implemented on the propeller and the rudder to achieve the target speed and the target heading angle respectively. The feedback controller 'cruise' (P_n=100, I_n=30, D_n=50) was engaged to rotate the propeller at an appropriate revolution, n(t) to achieve the target non-dimensionalised speed (U_T=1) for self-propulsion simulation. On the other hand, rudder angle, δ(t) was controlled by the feedback controller 'heading' (P_δ=1, I_δ=0.05, D_δ=4) to emulate a free-running ship under course-keeping control. The controller for the rudder aimed to achieve zero yaw deviation from the

target heading angle (ψ_T=0). PID gains for rudder control were the same as the experiments. The control mechanism for both the controllers is expressed in Equations 5.4 and 5.5. Both the controllers were used in self-propulsion simulations under course-keeping control in calm water and waves and were kept constant across all the simulations.

$$\Delta U(t) = U(t) - U_T$$
$$n(t) = P_n \Delta U(t) + I_n \int_0^t \Delta U(t)\, d\tau + D_n \frac{d\Delta U(t)}{dt} \tag{5.4}$$

$$\Delta \psi(t) = \psi_T - \psi(t)$$
$$\delta(t) = P_\delta \Delta \psi(t) + I_\delta \int_0^t \Delta \psi(t)\, d\tau + D_\delta \frac{d\Delta \psi(t)}{dt} \tag{5.5}$$

where, $U(t)$ and $\psi(t)$ are the instantaneous ship speed and yaw angle respectively.

However, during maneuvering simulations, open-loop controllers were used. The rudder angle was controlled by the 'zigzag' controller following the IMO standard maneuvering test procedure [46]. On the other hand, to satisfy Fn=0.26, the propeller revolutions were kept at a constant value predicted from the self-propulsion simulations.

5.4. ADOPTED COORDINATE SYSTEM

Two right-handed coordinate systems: Earth-fixed (inertial) and ship-fixed (non-inertial), were used to describe the computations. The ship–fixed system, translated and rotated according to the 6DOF solutions. The Earth-fixed system was not allowed to heave, pitch or roll but was allowed to move at a constant speed relative to the ship. This resulted in advancement in space only. The Earth-fixed coordinate system coincided with the ship fixed co-ordinate system at rest at the initial condition. The adopted coordinate systems are shown in Figure 5.3, where U, u, v, δ, ψ, β, and χ stand for ship service speed, surge speed, sway speed, rudder deflection angle, heading angle, drift angle, and incident wave angle, respectively. As per the experimental results provided by various institutions, the positive longitudinal *x*-axis points bow, *y* points starboard and *z* are positive downward with the origin located at the intersection of symmetry line, the waterline, and centre of gravity. For direct comparison, the predicted motions were adjusted to match the coordinate system used in experiments. Non-dimensional ship length was used in CFDShip-Iowa V4.5 computations.

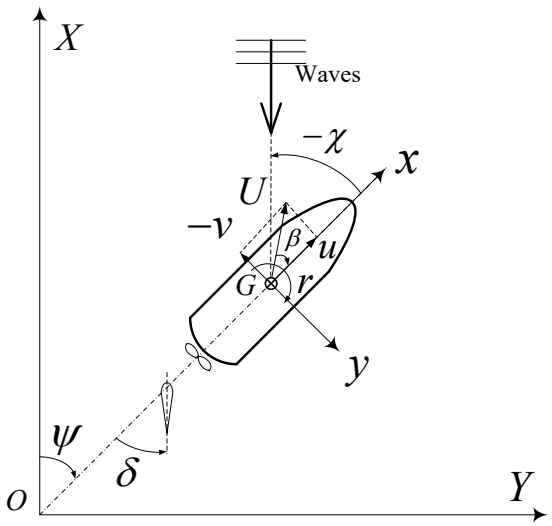

Figure 5.3 Adopted coordinate system.

5.5. HIGH-PERFORMANCE COMPUTING

The computations with grid system G1 were managed on the Argon and Neon system of The University of Iowa. The number of processors used for each case is listed in Table 5.2. In each case, only one processor was dedicated for dynamic Suggar++ computation and the rest for the flow solver.

All the computations with grid system G2 were managed on the Toda Lab server at Osaka University, which consists of 7 CPUs with 124 cores (Intel Xeon E5). 32 processors were allocated for the free-running computations, both in calm water and in waves, of which 31 processors were for flow computations and one processor was earmarked for dynamic Suggar++ computations.

5.6. PROPELLER OPEN WATER COEFFICIENTS

The thrust and torque prediction requires the advance coefficients (J) and open water curves. In the present study, the curves were defined as the second-order polynomial fit to the experimental open water curves. K_T (J) and K_Q (J) are the thrust and torque coefficients, respectively, and are defined by Equation 5.6. IIHR open water curves were used in simulations with grid system G1 whereas and MOERI open water curves were used for computations with grid system G2.

$$K_T = \frac{T}{\rho n^2 D_P^4}$$

$$K_Q = \frac{Q}{\rho n^2 D_P^5} \tag{5.6}$$

where, n is the propeller revolutions, D_P is the propeller diameter, ρ is the fluid density.

Table 5.2 Processor allocation for grid system G1

Case		Number of grid points	Number of processors
Case 1	Calm Water	10,799,780	128
Case 2			
Case 3			
Case 4	λ/L=0.65	21,952,940	320
	λ/L=1.00	13,678,466	168
	λ/L=1.15	13,678,466	
	λ/L=1.37	12,460,496	
Case 5	λ/L=1.00	13,678,466	224
Case 6			
Case 7			

Table 5.3 Thrust and Torque Coefficients

Parameters	MOERI	IIHR
$K_T(J)$	$-0.0609J^2-0.4390J+0.5228$	$-0.0892J^2-0.4280J+0.5020$
$K_Q(J)$	$-0.0114J^2-0.0512J+0.0725$	$-0.0148J^2-0.0523J+0.0752$

CHAPTER 6

MANEUVERING IN CALM WATER

In this chapter, the detailed validation study of the CFD method on appended KCS hull in unrestricted waters was extensively performed for self-propulsion under course-keeping control, zigzag maneuvers (±10°/10° and ±20°/20°), and turning circle (±35°) in calm water. The time series for ship motions, rudder angle, speeds, and trajectory was compared with experiments conducted at IIHR, The University of Iowa. The flow field was further studied to better understand the phenomenon.

Due to limited computational resources, a verification study for KCS was not performed. So far, our experience in building grids was based on the work by [25] that provides the complete verification and validation (V&V) study for KVLCC2.

In this study, validation was performed at the model scale by comparing with the experimental test data for calm water (steady-state). The error (E) was determined as the difference between computed data (S) and experimental data (D) and normalized using the experimental data (E%D), as shown in Equation 6.1.

$$E\%D = \left(\frac{D - S}{D} \right) \times 100 \tag{6.1}$$

6.1. HYDROSTATICS

The input database used in the modelling of the ship for experiments and the grid generation for computations was the same. The hydrostatic parameters used in the simulation were identical to the experiments for direct comparison. Only the longitudinal position of the centre of gravity, static wetted area, and total buoyancy weight of KCS in calm water conditions were computed. This was realized in the hydrostatic mode of CFDShip-Iowa v4.5 by shifting the LCG position such that the pitching moment turned to zero and thus the wetted area and weight were calculated. The computed values were very close to the experiments as seen in Table 3.1. The resulting values were used in all the following simulations.

6.2. SELF-PROPULSION UNDER COURSE-KEEPING CONTROL

Self-propulsion at the model point under course-keeping control with 6DOF motions in calm water was the first simulation case. The case was used to validate the designed CFD method with an overset grid by comparing against experimental data of IIHR, The University of Iowa. To further adjudge the efficiency of the OU propeller model in the adopted setup, the computed integral values were compared with the computational results, from IIHR, The University of Iowa. The latter was performed by [42], for similar test conditions and grid setup, using a fully discretized actual propeller (DP) and an axisymmetric body force (BF) propeller model.

Engine restrictions result in insufficient power generation, at the start of the experiment, thus limiting thrust and torque supply. Consequently, experimental fluid dynamics (EFD) was conducted with the propeller being ramped up and kept constant when the desired speed was reached. The computations, contrarily, were started from rest with an initial propeller revolution maintained at 20rps. Due to this inherent difference in the initial condition of CFD and experiments, the EFD data was shifted to match the ship speed at the release point. The steady state environment was compared for CFD and EFD data. Due to the higher inertia of the model, the convergence was slow. Artificial damping was not used to accelerate the same.

KCS being a single screw single rudder ship, tends to turn portside. The asymmetric flow at the stern caused by a clockwise rotating propeller introduces pressure difference on both sides of the rudder. The pressure difference generates a negative yaw moment causing the hull to turn portside. To counter the situation, the rudder needs to be deflected to the starboard. This angle is known as the neutral rudder angle or check helm angle. To analyse the phenomenon, rudder control was activated during self-propulsion prediction. The predicted rudder angle was necessary to maintain a straight-ahead course.

Figure 6.1 and Figure 6.2 show the comparison of time series of PID controls, neutral rudder angle, propeller thrust and torque, 6DOF motions between computational results for grid system G1, grid system G2, and the EFD data. Table 6.1 summarizes the steady state integral values of OU-CFD and experiments and computations conducted at IIHR, The University of Iowa [42].

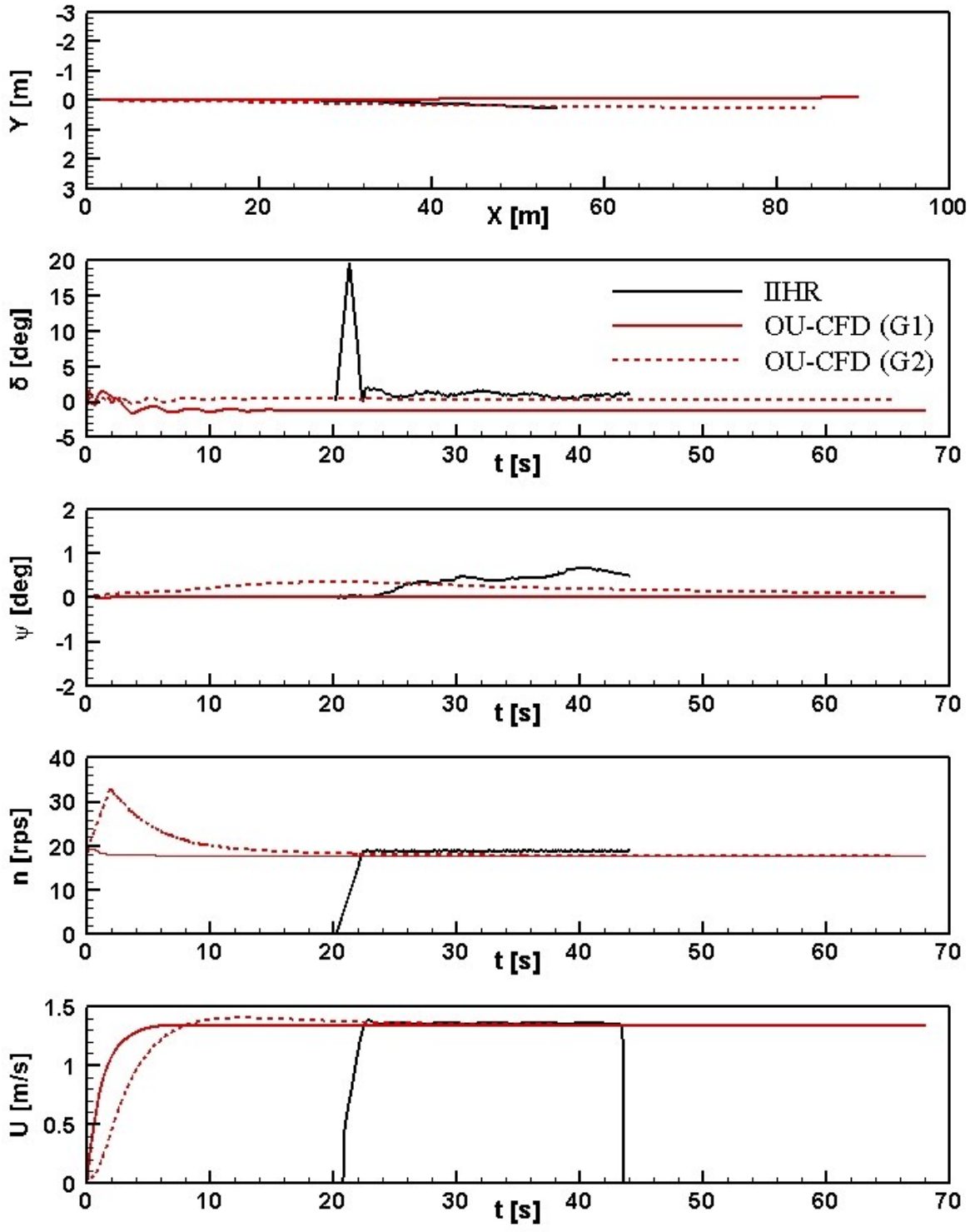

Figure 6.1 Comparison of time histories of PID controls and trajectories during the self-propulsion simulation.

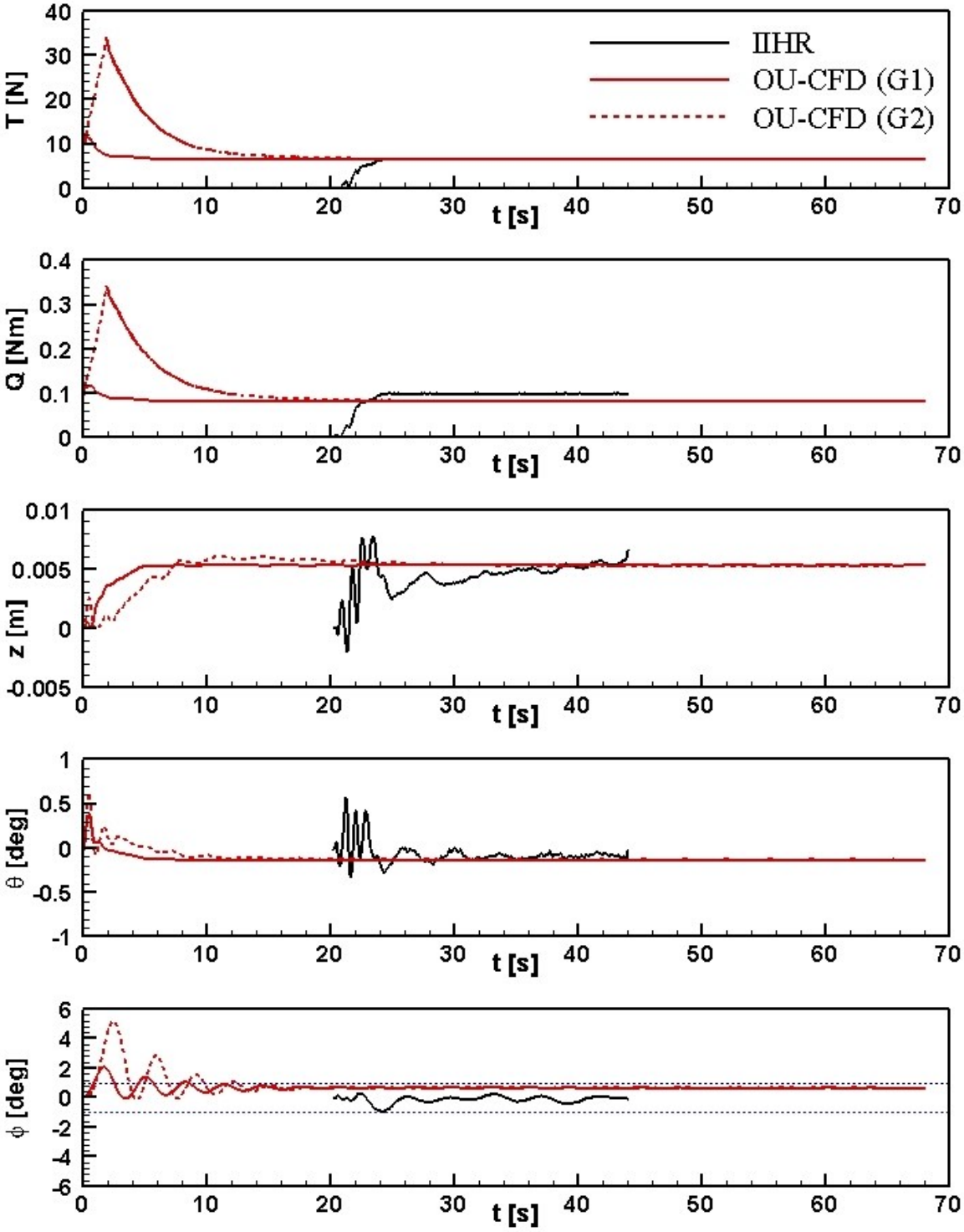

Figure 6.2 Comparison of time histories of motions and forces during the self-propulsion simulation.

6.2.1. *PID controlled Variable*

On adjusting the propeller revolutions, based on Equation 5.4, the ship speed was attained. The target ship speed was accurately predicted by OU computations using both the grid systems (G1 and G2). However, the propeller revolution speed was underestimated for both the grid systems but the error percentage was within acceptable limits (E%D <5%). Due to its detailed modelling and its proximity in behavior with an actual propeller, the fully discretized propeller showed good agreement (E%D<4%) with the experimental data. The BF model, however, overestimated (E%D about 22.5%) the propeller revolution speed as the model itself is based on ship speed and not on the propeller inflow velocity [42]. On comparing with the other propeller models, the OU propeller model showed smaller E%D than the BF model by 17.5% but showed higher E%D than the DP by 1%. The performance of the adopted PID approach was satisfactory.

As observed from Table 6.1, the neutral rudder angle prediction was challenging. The experiments reported a small neutral rudder angle to starboard for course-keeping. In OU computation using G2, a similar phenomenon was predicted although the E%D (≈ 45%) was higher compared to computation with BF model (24%) but lower compared DP computation. However, computation using G1 failed. As the angle is small, the coarse grid of G1 could be the reason. [42] showed better prediction in neutral rudder angle with finer grids. However, due to the limitation of computational resources, simulation using finer grids was not achieved. The reason for the discrepancy requires further investigation.

6.2.2. *Propeller Forces*

The prediction of the dimensional value of propeller thrust was satisfactory for OU computations using both the grid systems with the error percentage being within acceptable limits. On comparing with computations using other propeller models, E%D of OU propeller model with grid system G1 was similar to the BF model whereas G2 showed a slightly higher value compared to the BF model. Computations with G1 and G2 showed smaller E%D than the computations with DP by 5% and 3%, respectively.

The prediction of the dimensional value of propeller torque was underestimated for both the grid systems and the deviation was high (E%D was 18%). This could be attributed to the adopted drag coefficient in the propeller code. However, the comparison of torque coefficient

showed better agreement with the experiment where E%D for G1 and G2 were 5.3% and 6.5% respectively. On comparing torque obtained from computations using other propeller models, the OU propeller model showed smaller E%D than the BF model by 8% but showed higher E%D than the DP by 14%.

Table 6.1 Comparison of self-propulsion parameters

Parameters	IIHR-EFD (D)	OU-CFD G1 (S_1)	OU-CFD G2 (S_2)	IIHR-CFD (DP)	IIHR-CFD (BF)	E%D (S_1)	E%D (S_2)
PID Controlled Variables							
Propeller revolution: n[rps]	18.69	17.84	17.91	18.08	22.89	4.55	4.17
Ship speed: U [m/s]	1.34	1.34	1.34	1.34	1.34	0.00	0.00
Rudder Angle: δ [°]	0.75	-1.22	0.41	1.52	0.93	262.67	45.33
Propeller Forces							
Thrust: T [N]	6.57	6.52	6.41	6.19	6.55	0.76	2.44
Torque: Q [N]	0.10	0.082	0.082	0.096	0.126	18.00	18.00
Motions							
Heave: z [m]	0.0059	0.0053	0.00523	0.0056	0.0058	10.17	11.95
Pitch: θ [deg]	-0.090	-0.13	-0.13	-0.158	-0.128	-38.89	-38.89
Roll: φ [deg]	-0.12	0.64	0.65	-0.60	0.36	634.71	641.67

6.2.3. *Motions*

As shown in Table 6.1, the prediction accuracy for heave motion using G1 and G2 were comparable. Both the systems showed an E%D of about 10%. On comparing with computations with other propeller models, the E%D reported by G1 was higher than the BF model and DP by 8% and 5% respectively. As the heave motion is strongly coupled with the pitch motion, the notable difference in predicted pitch motion leads to a higher percentage of error in heave motion. Computations with G1 and G2 showed a notable difference in pitch angle. E%D for G1 and G2 were -39%. As reported by [42], E%D for computations with the BF model and DP was -43% and -76% respectively. On comparing with computations using other propeller models, G1 and G2 with OU propeller model showed less E%D compared to BF model and DP by 4% and 37% respectively. Overall, the computations with grid systems G1 and G2 using the OU propeller model fared better.

Computations with both grid systems G1 and G2 failed to predict the roll. Due to the simplified rudder geometry used in simulations with grid system G2, there existed a dissimilarity in the centre of pressure between CFD and EFD. This led to a higher deviation

of roll prediction as moment generated due to the difference in height between centre of pressure and centre of gravity was not the same in CFD and EFD. As shown in Table 6.1, opposite roll angle was also reported for the body force propeller model by [42]. Only the fully discretized model showed a similar trend to the experiment. As the roll angles were small (less than 1°), the effect of the same on maneuvering simulations was expected to be less.

6.2.4. *Neutral Rudder Angle*

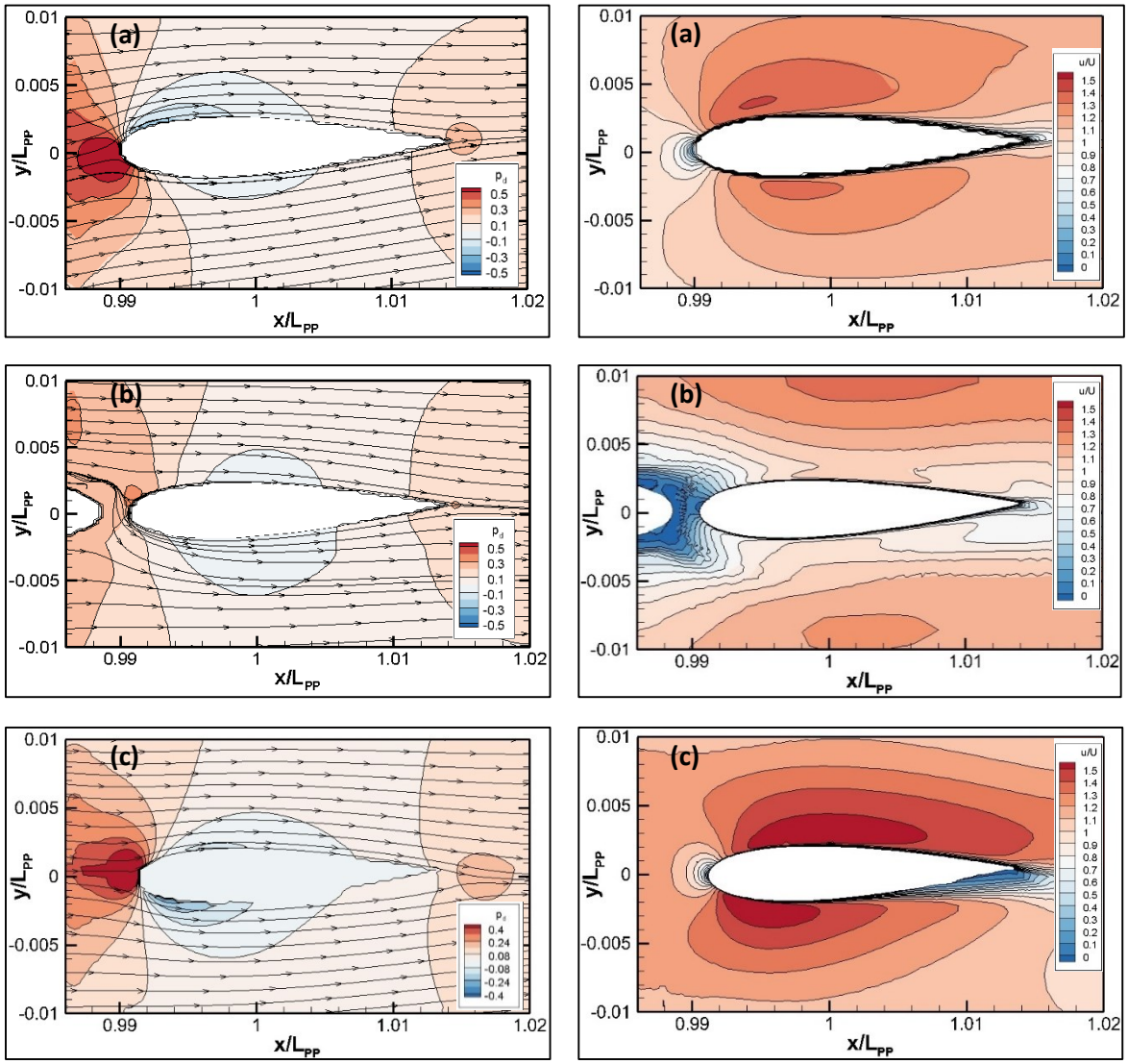

Figure 6.3 (left) Dynamic pressure and Streamlines and (Right) Velocity contours at various p_z/R sections.

The flow field around the rudder was studied for computations with grid system G2 at (a) p_z/R=0.7, (b) p_z/R=0, and (c) p_z/R=-0.7, as presented in Figure 6.3. The dynamic pressure (p_d) along with streamlines and the axial velocity (u/U) was plotted. The movement of flow from

high pressure to low pressure followed the traditional laws of physics. Upward flow on the portside of the rudder and downward on the starboard side of the rudder was noticed. This was due to the induced swirl introduced by the right-handed propeller. On observing the streamlines in conjunction with the velocity contour, it was noticed that at locations with zero velocity, the streamlines curl up to a point known as the stagnation point. It was also noted that higher velocity contours correspond to the lower pressure contours as the flow was accelerated from higher pressure to lower pressure. Thus, the flow moved faster when it reached the lower pressure region. As noticed from the plotted streamlines, the angle of attack of (a) was to starboard while in (c) it turned to be zero. The negative pressure was equal but opposite for sections (a) and (c), thus canceling. In the absence of the neutral rudder angle, the force on the starboard side caused by a higher angle of attack would result in a higher negative yaw moment. This would turn the ship to port. Thus, the flow field emphasizes the use of a neutral rudder angle for straight-ahead course.

6.2.5. *Local Flow Prediction*

To better understand the mechanism of the flow, the flow field of computation with grid system G2 was investigated. The computed effective wake at various axial cross-sections across the hull is shown in Figure 6.4.

(a) x/L=0.975 from F.P. (just ahead of propeller),

(b) x/L=0.9825 from F.P. (at the propeller centre),

(c) x/L=1.00 from F.P. (at the rudder stock) and

(4) x/L=1.025 from F.P. (just after rudder).

The flow field was mapped with axial velocity (u/U) and cross-field vectors (v/U and w/U). The figures showed the evolution of the boundary layer across the hull, with the solid surface marked with blue contour. The symmetric axial velocity contour, as indicated in Figure 6.4(a), was disturbed after the introduction of the propeller as seen in Figure 6.4(b)-(d). The clockwise rotation of the propeller was also noticed. The low-speed area under the boss in Figure 6.4(a) denoted the ship stern was upward. The bilge vortex was present above the hub. Due to the presence of a rudder, the wake field splits into two at the hub location and rotates in opposite directions to each other. The outside contour colour of pink represents flow velocity same as the ship speed. Due to the clockwise rotation of the propeller, the flow velocity was higher on the starboard side.

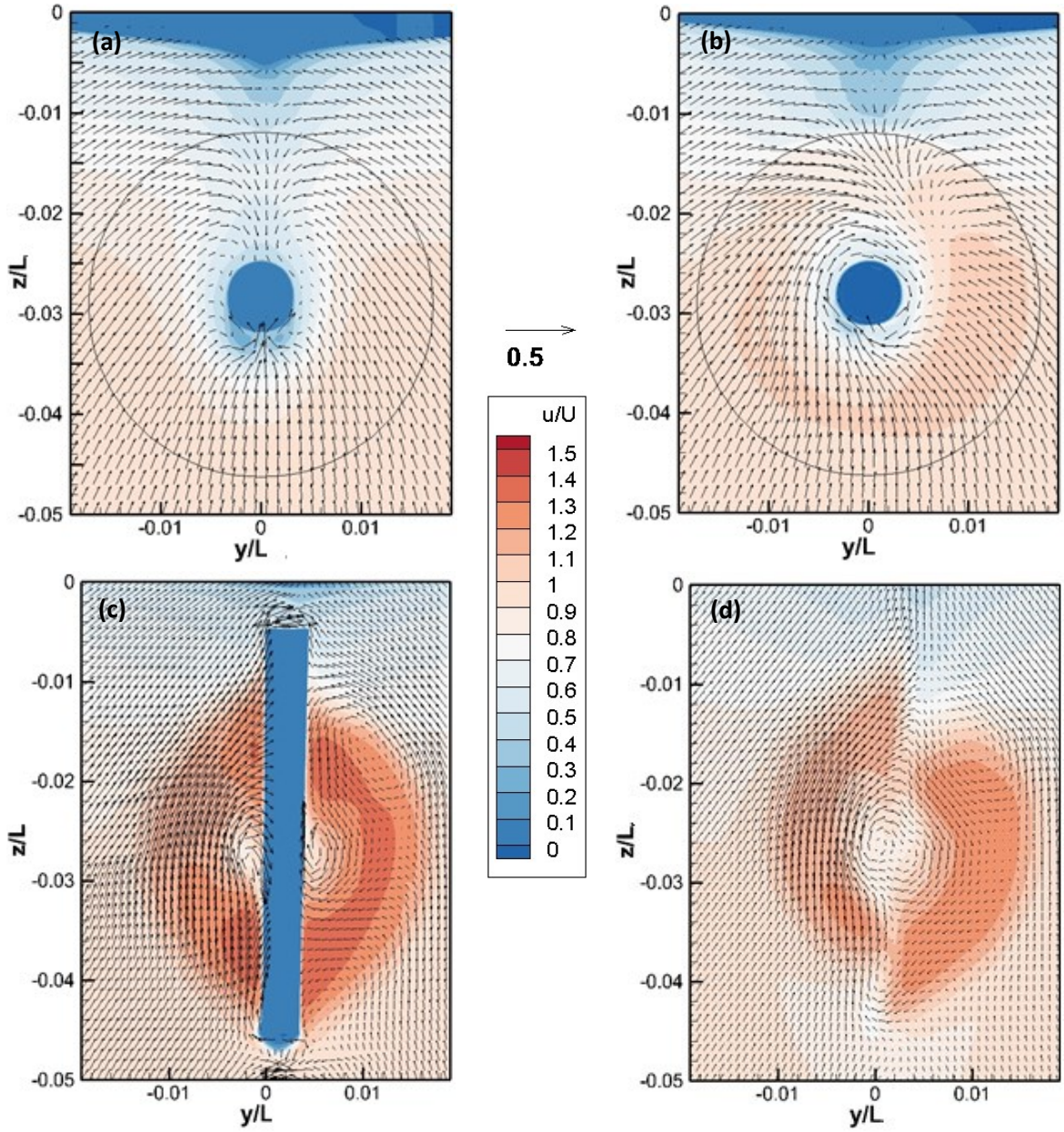

Figure 6.4 Axial Velocity Contours at various *x/L* sections.

The local flow prediction (for both grid systems G1 and G2) in calm water aft of the rudder (*x/L*=1.025 from F.P.) was compared with OU S-PIV data and IIHR-CFD [42] using the fully discretized propeller (see Figure 6.5), for further validation on the flow field. The flow field was mapped with axial velocity (*u/U*) and cross-field vectors (*v/U* and *w/U*). Due to the clockwise rotation of the propeller, the axial flow velocity was higher on the starboard side than the portside and the same was observed in all the computations. Two separated vortices near the hub were detected efficiently by OU-CFD with grid system G2. The positioning of the hub vortices was similar in the *z/L* direction. In the *y/L* direction, the portside vortex in CFD was much closer to the starboard vortex than in EFD. On the other

hand, grid system G1 showed only one hub vortex similar to IIHR-CFD predictions. As stated earlier in chapter 4, in calm water OU-CFD with grid system G1 was essentially the same grid used in IIHR-CFD computations except for the propeller grid. The lack of accuracy in predicting the two vortices by G1 could be attributed to the coarser grid used in the domain compared to G2. [42] showed better agreement with experiments on using finer grids. The clockwise vortex-induced vertically lower part of the propeller around (y/L, z/L) = (0.0, -0.04) was predicted accurately by grid system G2. An anticlockwise vortex-induced near the starboard side above the propeller (0.01, -0.02), caused by the cross-flow between downward starboard flow and outer upward flow, and was also predicted well by CFD. Though the CFD captured the higher inflow to the propeller on the upward portside qualitatively but failed in capturing it quantitatively. The reason for the difference could be attributed to the presence of rudder deflection and roll angle.

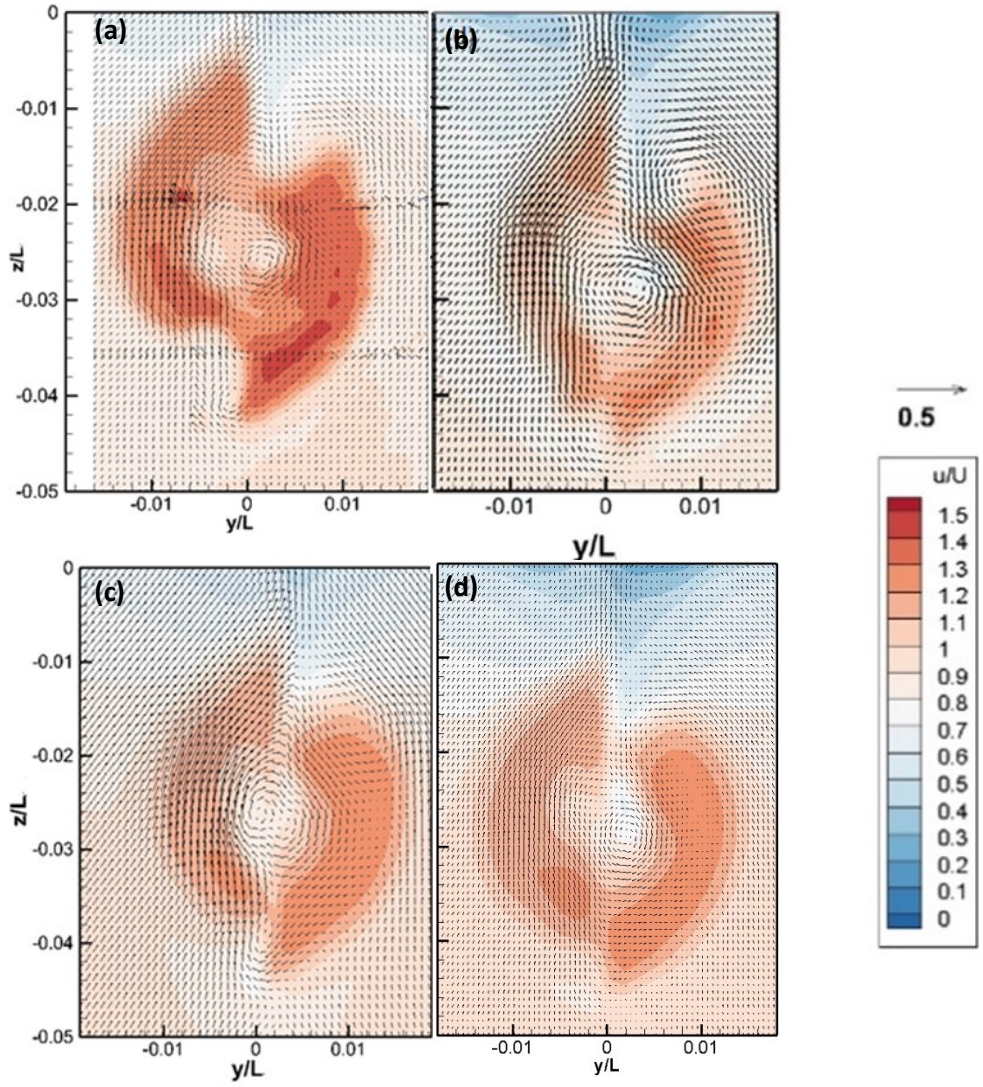

Figure 6.5 Comparison of flow field at x/L=1.025 (a) OU S-PIV (b) IIHR-CFD DP [42] (c) OU-CFD G2 (d) OU-CFD G2.

6.3. CALM WATER MANEUVERING

Once the self-propulsion simulation was complete, maneuvering simulations with grid systems G1 and G2 were performed. During maneuvers, the real geometric rudder deflection was considered and not away from the neutral rudder angle. Initial conditions (t=0) at the start of the maneuver were:

(a) Ship position in the earth-fixed coordinate, $(X_0,Y_0)=(0,0)$,

(b) Ship velocity, $u=U_0$ (the target ship velocity corresponding to Fn=0.26 achieved in the self-propulsion simulation)

(c) Propeller revolution speed, $n=n_{self\text{-}propulsion}$ (kept constant at the predicted value from self-propulsion simulation)

(d) Yaw rate, r=0,

(e) Rudder angle, $\delta=\delta_0$ (which is the neutral rudder angle)

The time histories of motion, motion rates, and rudder angle were compared with experimental data from IIHR, The University of Iowa, and MARIN. As this was one of the first attempts in using the OU propeller model in maneuvering simulations, the integral parameters were also compared with the computational results, from IIHR, The University of Iowa [42] to understand the efficiency of the adopted setup. The reported results using the BF model by [42] were for a finer grid setup compared to the self-propulsion results using the same model illustrated in the earlier section. However, the reported results using the fully discretized propeller model were using the same grid setup as G1.

6.3.1. *Turning Circle Maneuver*

The ship is maintained at straight running condition and having zero yaw rate, followed by rudder execution to maximum design rudder angle until the ship enters into steady turning. The path of centre of gravity is recorded during the test. Depending on which side the rudder (starboard or port) is deflected, the ship experiences a slight deviation to the other side (port or starboard), as shown in Figure 6.6, caused due to the rudder lateral force post the introduction of rudder deflection. Once the yaw moment generated surpasses the rudder lateral force, the ship starts to turn.

Figure 6.7 and Figure 6.8 show the comparison of trajectories, motions, motion rates, velocities, and rudder angle for portside and starboard turning between OU-CFD (G1 and G2)

and EFD results. The non-dimensionalised advance (A_d/L), transfer (T_r/L), tactical diameter (T_D/L), time taken to change headings of 90° and 180°, steady yaw rate, velocity drops, and roll angle were obtained from the turning circle simulation and are placed at Table 6.2 and Table 6.3.

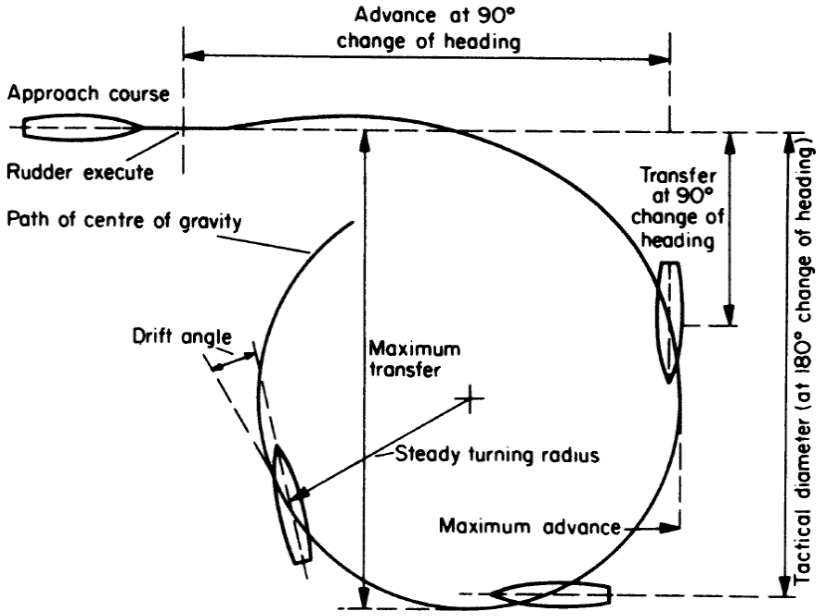

Figure 6.6 A typical example of motion path of centre of gravity during a turning circle test defining the terminologies involved. [30]

As explained in earlier sections, the ship has an inherent tendency to turn to the portside as KCS is a single screw single rudder ship with asymmetric propeller rotational flow causing a pressure difference on either side of the rudder thereby generating rudder force to portside. Due to the portside maneuverable characteristic, the tactical diameter of portside turning was smaller than that of the starboard side turning. As observed from Table 6.2 and Table 6.3, the tactical diameter of starboard turning was larger than portside turning by 12.7% and 6.7% for experimental data of IIHR and MARIN respectively. Computations with grid systems G1 and G2 showed starboard turning was larger than portside turning by 2.7% and 4.25% respectively. Though CFD results followed the trend, the difference in tactical diameter of port and starboard turning was not as prominent as that in the experiments. Computations of IIHR, The University of Iowa [42] using fully discretized propeller also showed the same trend, with the tactical diameter of starboard turning being larger than portside turning by 2.67%. However, computations with BF model showed an opposite trend with the tactical diameter of portside turning being larger than starboard turning by 3.8% [42]. In summary, all the computations using various propeller models reported a very small differences in tactical diameter for port and starboard turning.

(a) Portside Turning

As shown in Figure 6.3, the comparison of time series shows reasonable agreement of computations using G1 with the experimental data. However, the trajectory was over-predicted. However, using G2 with a rudder angle of 35° showed a lack of prediction accuracy for all the parameters. This emphasized the error in rudder modelling. The prediction accuracy improved significantly on using a 30° rudder angle. The details of the same are explained later in the chapter.

On comparing with both sets of experimental data, as shown in Table 6.2, the advance was over-predicted with G1 but under-predicted by G2. On comparing with computations using other propeller models, E%D (D=IIHR & MARIN) of advance using OU propeller model with grid system G1 was similar to the BF model whereas it was slightly lower (≈2%) compared to DP model. G2, however, showed a higher E%D compared to both the propeller models but the deviation was particularly prominent when experimental results of MARIN were used for error percentage calculation.

Similar to the prediction of advance, the transfer as well was over-predicted with G1 but under-predicted by G2 when compared to both the experiments. E%D (D=IIHR & MARIN) of transfer using OU propeller model with grid system G1 was similar (<1%) to the BF model whereas it was slightly lower (≈2.5%) compared to DP model. G2, however, showed a higher E%D compared to both the propeller models.

Similar to the prediction of advance and transfer, the tactical diameter as well was over-predicted with G1 but under-predicted by G2 when compared to both the experiments. E%D (D=IIHR & MARIN) of tactical diameter using OU propeller model with grid system G1 was similar (<1%) to the DP model whereas it was higher (≈4%) compared to BF model. G2, however, reported a very high E%D compared to both the propeller models.

Again, the time taken to change headings of 90° and 180° was over-predicted with G1 and under-predicted with G2 compared to both the experiments. The results however agreed reasonably well for both the grid systems. E%D compared well other computational results as well.

The ship velocity at the steady turn was also compared with experimental data. As evident from figures and tables, G1 predicted better compared to G2. The average E%D, using G1, was about 7.5%. The higher drop in velocity using G2 resulted in a smaller tactical diameter. The predicted rate of steady turn for both G1 and G2 was closer to experimental data of MARIN than to IIHR, The University of Iowa with better accuracy achieved by G1. On using G1, the predicted angle of heel was closer to experimental results of IIHR (E%D about 3%) than to MARIN (E%D about 29%). However, on using G2, the E%D was very high for both sets of experimental data. The inaccurate prediction of heel in the initial steady approach phase could play a role in the poor estimation of heel in turning. The angle of heel computed by other propeller models was not available for comparison.

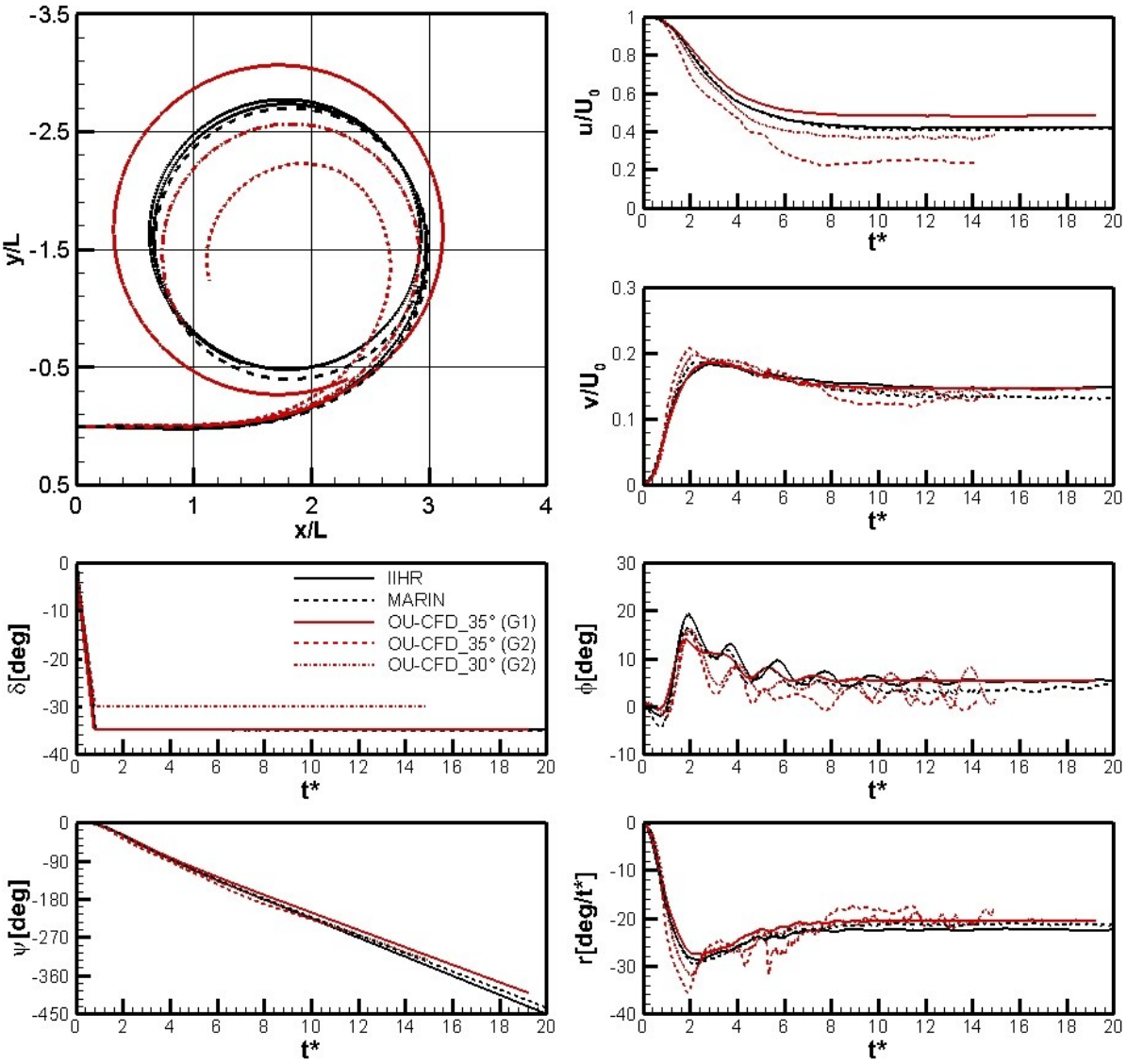

Figure 6.7 Comparison of time histories of motions, motion rates, velocities, rudder and heading angle during the portside turning maneuvering simulation.

Table 6.2 Comparison of portside turning circle parameters

Parameters		D		S		IIHR-CFD (DP)	IIHR-CFD (BF)	E%D (D=IIHR)		E%D (D=MARIN)	
		IIHR	MARIN	OU-CFD G1	OU-CFD G2			G1	G2	G1	G2
35°	A_d/L	2.87	2.93	3.05	2.59	3.12	3.08	-6.27	9.76	-4.09	11.60
	T_r/L	-1.13	-1.09	-1.23	-0.95	-1.26	-1.23	-8.85	15.93	-12.84	12.84
	T_D/L	-2.69	-2.64	-3.00	-2.12	-3.00	-2.90	-11.52	21.19	-13.63	19.70
	$t^*[A_d/L, T_r/L]$	4.09	4.18	4.31	3.89	4.34	4.23	-5.38	4.89	-3.11	6.94
	$t^*[T_D/L]$	7.88	8.08	8.45	7.42	8.35	7.87	-7.23	5.84	-4.58	8.17
	u/U_0	0.45	0.44	0.48	0.24	-	-	-6.67	46.67	-9.09	45.46
	$r[deg/t^*]$	-24.01	-21.67	-20.53	-19.51	-	-	14.77	18.74	5.26	9.97
	φ [deg]	5.137	4.109	5.30	2.28	-	-	-3.17	55.62	-28.99	44.51
30°	A_d/L	-	-	-	2.84	-	-	-	1.05	-	3.07
	T_r/L	-	-	-	-1.06	-	-	-	6.20	-	2.75
	T_D/L	-	-	-	-2.49	-	-	-	7.43	-	5.68
	$t^*[A_d/L, T_r/L]$	-	-	-	4.06	-	-	-	0.73	-	2.87
	$t^*[T_D/L]$	-	-	-	7.92	-	-	-	-0.51	-	1.98
	u/U_0	-	-	-	0.37	-	-	-	17.78	-	15.91
	$r[deg/t^*]$	-	-	-	-20.62	-	-	-	14.20	-	4.85
	φ [deg]	-	-	-	4.06	-	-	-	20.97	-	1.19

(b) Starboard Turning

As observed from Figure 6.4, the comparison of time series showed a reasonable agreement of computations using G1 with the experimental data. However, the trajectory of the ship was complicated. Initially, an over-prediction was noted but around 180° heading the trajectory plunges and follows the experimental data on the inner side. On the other hand, using G2 with a rudder angle of 35° showed a lack of prediction accuracy for all the parameters similar to portside turning.

Similar to portside turning, on comparing with both sets of experimental data reported in Table 6.3, advance, transfer, tactical diameter, and time taken to change heading to 90° and 180° were under-predicted using G2, However, G1 over-predicted all the parameters compared to MARIN but, for the most part, under-predicted the parameters compared to experimental results of IIHR, The University of Iowa. The model used in experiments by MARIN was larger than that used by IIHR, The University of Iowa.

In the case of prediction of advance using OU propeller model with grid system G1, E%D (D=IIHR) was similar to the BF model whereas E%D (D=MARIN) was higher (≈7%) compared to the same. However, E%D (D=IIHR & MARIN) using G1 was slightly higher (≈2%) compared to the fully discretized propeller. The transfer predicted using G1 was closer to the EFD data of IIHR than MARIN. However, computations using other propeller models reported the opposite trend. The tactical diameter predicted using G1 was closer to the EFD data of MARIN than IIHR. The average E%D (D=IIHR & MARIN) using G1 was about 4%, similar to the values reported using BF model and fully discretized propeller [42].

In the case of prediction of the above parameters using G2, E%D was high compared to both the propeller models but the deviation was particularly prominent when experimental results of IIHR were used for error percentage calculation. This emphasized the error in rudder modelling.

The predicted time taken to change the heading of 90° and 180° using grid system G1 was closer to IIHR experiments than MARIN. E%D (D=IIHR &MARIN) for the time taken to change heading to 180°, using G1, was similar to the fully discretized propeller whereas the same was lower (≈9%) compared to the BF model.

At the steady turn, the ship velocity, rate of turn, and angle of the heel were compared with the experimental results. The ship velocity using G1 compared well with experimental data (average E%D of about 3%). The average E%D, using G2, was about 26%. The higher drop in velocity using G2 resulted in a smaller tactical diameter.

The predicted rate of turn, however, showed better results for G2 than G1. The average E%D (D=IIHR & MARIN) using G1 and G2 was around 9% and 1.75% respectively. Using both G1 and G2, the prediction of the angle of the heel failed with high E%D (D=IIHR &MARIN). The reason for this discrepancy is uncertain and requires further study.

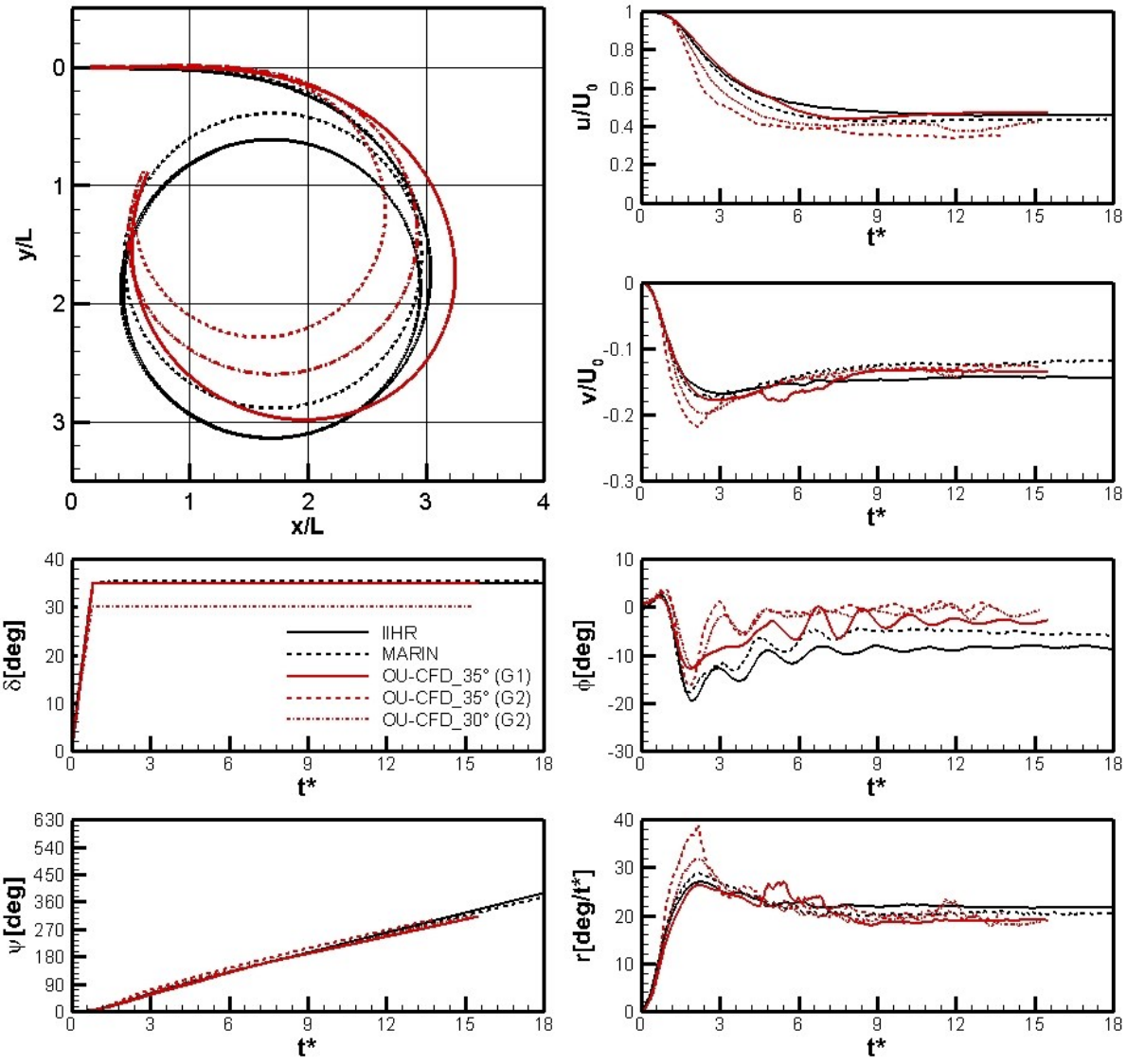

Figure 6.8 Comparison of time histories of motions, motion rates, velocities, rudder and heading angle during the starboard turning maneuvering simulation.

Table 6.3 Comparison of starboard side turning circle parameters

Parameters		D		S		IIHR-CFD (DP)	IIHR-CFD (BF)	E%D (D=IIHR)		E%D (D=MARIN)	
		IIHR	MARIN	OU-CFD G1	OU-CFD G2			G1	G2	G1	G2
35°	A_d/L	3.06	2.90	3.18	2.58	3.11	2.96	-3.92	15.69	-9.66	11.03
	T_r/L	1.34	1.21	1.32	0.83	1.22	1.15	1.49	38.06	-9.09	31.41
	T_D/L	3.08	2.83	2.92	2.21	3.08	2.79	5.20	28.25	-3.18	21.91
	$t^*[A_d/L, T_r/L]$	4.39	4.18	4.55	3.79	4.25	4.07	-3.64	13.67	-8.85	9.33
	$t^*[T_D/L]$	8.44	8.41	8.515	7.74	8.48	7.63	0.89	8.29	-1.25	7.97
	u/U_0	0.49	0.46	0.47	0.35	-	-	4.08	28.57	-2.17	23.91
	$r[deg/t^*]$	21.34	20.59	19.03	20.69	-	-	10.83	3.05	7.58	-0.49
	φ [deg]	-10.591	-5.781	-3.16	-0.065	-	-	70.16	99.39	45.34	98.88
30°	A_d/L	-	-	-	2.85	-	-	-	6.86	-	1.72
	T_r/L	-	-	-	0.99	-	-	-	26.12	-	18.18
	T_D/L	-	-	-	2.53	-	-	-	17.86	-	10.60
	$t^*[A_d/L, T_r/L]$	-	-	-	4.15	-	-	-	5.47	-	0.72
	$t^*[T_D/L]$	-	-	-	8.48	-	-	-	-0.47	-	-0.83
	u/U_0	-	-	-	0.40	-	-	-	18.37	-	13.04
	$r[deg/t^*]$	-	-	-	19.49	-	-	-	8.67	-	5.34
	φ [deg]	-	-	-	-0.99	-	-	-	90.65	-	82.88

(c) Sensitivity Test

As observed in Figure 6.7 and Figure 6.8, computations using grid system G2 showed a poor agreement of all parameters with experiments for both starboard side and portside turning with a rudder angle of 35°. This emphasized the modelling error caused due to oversimplification of rudder geometry. In the rudder geometry model used in G2, the entire model was free to rotate, and hence the higher lateral area was subjected to maximum rudder angle thereby producing higher rudder force. The force induced by the rudder at 35° (port and starboard) was higher due to higher speed drops. That resulted in a smaller tactical diameter prediction. A sensitivity test was performed for both starboard and portside turning with ±30° to study this effect. The rudder angle reached ±30° at the same point where the rudder angle was intended to reach its maximum design rudder angle of ±35°. The predicted results were compared with the experimental results for a rudder angle of ±35°.

As known from the theory of turning, the yaw moment generated due to rudder side force is predominant in the transient and steady turning phase of the turning circle maneuver. Hence the accurate prediction of Y-force and thereby the yaw moment is necessary to predict the turning circle characteristics with higher accuracy. Ship and rudder forces for portside turning with rudder angles of -35° and -30° were compared and placed at Figure 6.9. As can be observed from Figure 6.9 (a) and (b), the ship experiences the X-forces, i.e., the resistance, predominantly compared to Y-force and N-moment which was close to zero for both the rudder angles. As can be clearly noticed in Figure 6.9 (1) and (2), there was a reduction in rudder forces when a lesser maximum rudder angle was used. During the transient phase, the estimation of rudder side force and yaw moment was higher for -35° than for -30° with a sudden spike in the rudder forces. Although in the case of the steady turning phase, the prediction of rudder side force -35° was close to forces predicted by rudder angle of -30°.

The prediction of velocity improved for both port and starboard turning thereby the tactical diameter prediction improved. On comparing with experimental data of IIHR, The University of Iowa and MARIN, for portside turning, E%D of the tactical diameter reduced by about 14%. On the other hand, for starboard side turning, E%D of the tactical diameter was reduced by about 10%. Due to the presence of horn fixed to the hull, the predicted tactical diameter using a semi-balanced horn rudder was higher compared to the spade rudder as the angle of attack to the movable rudder changes. The percentage increase of tactical

diameter was 20% in portside turning and 15% in starboard turning when compared against rudder angle of 30°.

At the change of 90° heading, prediction of advance also improved for both port and starboard turning by 8%. In the case of prediction of transfer, the E%D was reduced for both port and starboard turns. However, the transfer was better predicted for portside (E%D=6.20%) than for starboard side turning (E%D=26.12%). The time taken to change headings of 90° and 180° matched very well for both port and starboard turning.

The angle of heel prediction when starboard turning did not match well with the experiments even after using a lesser maximum rudder angle. But in the case of portside turning, the heel angle estimation improved on implementation of lesser maximum rudder angle. The inaccurate prediction of heel in the initial steady approach phase could play a role in the poor prediction of heel in turning.

The overall prediction of the parameters was reasonable when grid system G1 (the actual rudder geometry) was used. The predictions improved for grid system G2 (modified rudder geometry) on using lesser rudder angle indicating that modelling of modified rudder requires improvement. All parameters reported using grid system G2 showed an under-prediction even after using a smaller rudder angle whereas G1 showed an over-prediction. The satisfactory reason for this discrepancy is not yet known and more study is required.

In summary, it was highlighted that a low fidelity model (such as the OU propeller model and BF model) was capable of handling turning circle maneuvers provided the resolution of the grid near the rudder was good. Although the grid system G1 used in computations was coarser compared to the grid setup used in computations with the BF model [42], the integral parameters fared well with the experiments and sometimes better than the other models.

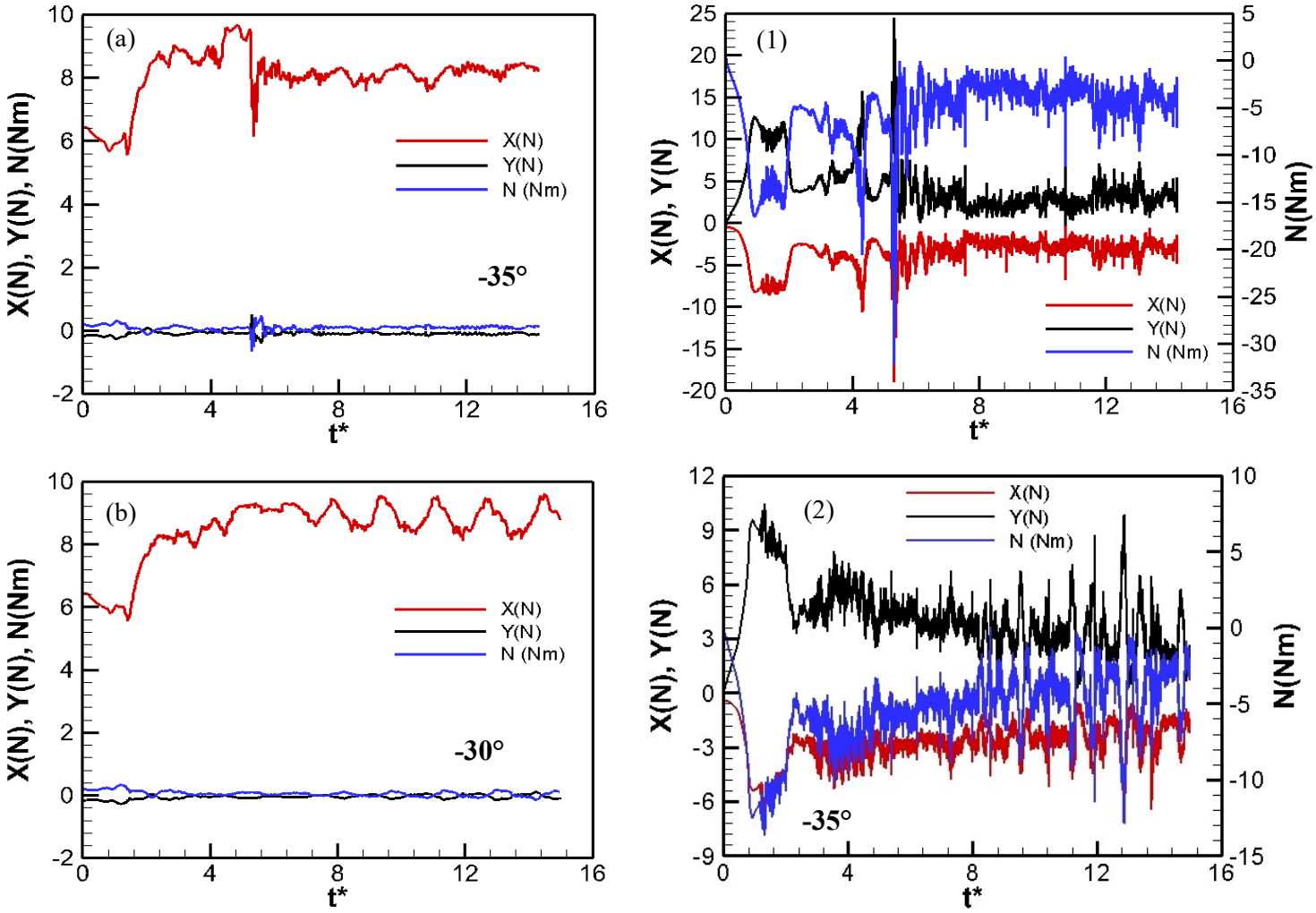

Figure 6.9 (a) Time histories of Ship Forces for -35°.
(b) Time histories of Ship Forces for -30°.
(1) Time histories of Rudder Forces for -35°.
(2) Time histories of Rudder Forces for -30°.

6.3.2. *Zigzag Maneuver*

The simple zig-zag test is performed to evaluate the indices of course-keeping and course-changing abilities. A zigzag maneuver is performed by applying a specified amount of rudder angle either portside or starboard side. Once the yaw response of ship is reached the desired amount, the rudder angle is then alternatively shifted to either side. In the case of 20°/20° zigzag test, 20° of rudder angle and 20° yaw angle is targeted whereas, in the case of 10°/10° zigzag test, 10° of rudder angle and 10° yaw angle is the target. The difference in the peak of yaw response and maximum rudder angle is the overshoot angle and depending on the occurrence of the overshoot it is defined as first overshoot angle or second overshoot angle. The overshoot angle is easily obtained from the time histories of yaw response and for this reason, International Maritime Organization Maneuverability Standards uses this index to judge the course-keeping and course changing ability of a ship. Along with the overshoot angles, the initial turning time to second execute and time to check yaw is used to evaluate the maneuvering characteristics.

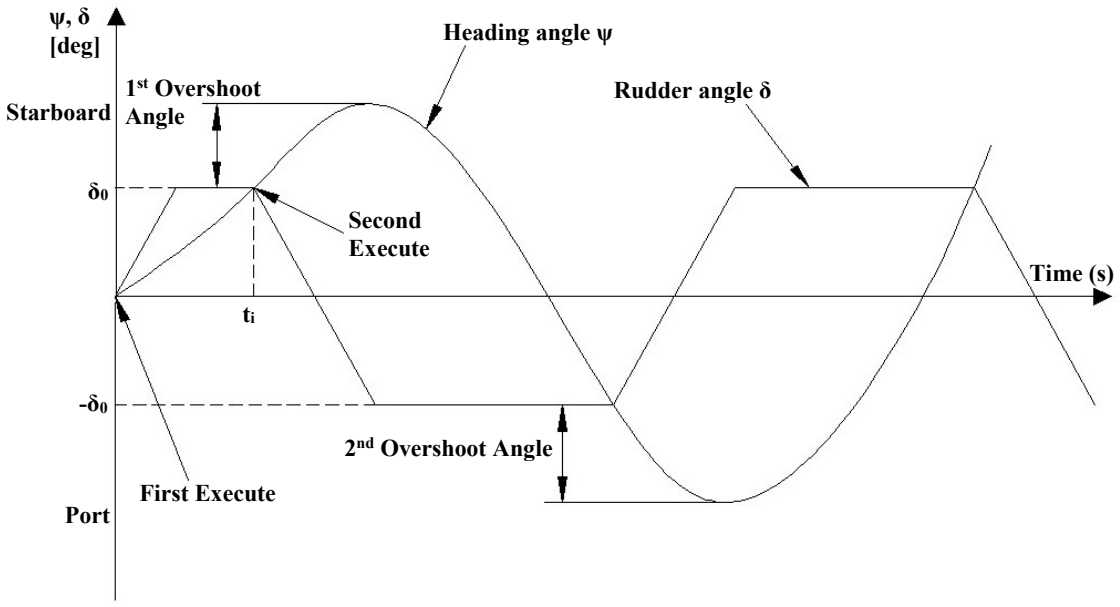

Figure 6.10 A typical example of time histories of rudder angle and yaw response during zigzag maneuver.

The time histories of motions, motion rate, yaw response, and rudder angle for portside and starboard side zigzag 20°/20° are placed at Figure 6.11 and Figure 6.12 respectively. Figure 6.13 and Figure 6.14 show the comparison of trajectories, motions, motion rates, velocities, and rudder angle for portside and starboard zigzag 10°/10° between

OU-CFD (G1 and G2) and EFD results, respectively. The time histories were compared with IIHR, University of Iowa [42], and MARIN [20]. The details of 1st and 2nd overshoot obtained are placed in Table 6.4 to Table 6.7. The integral parameters obtained from the zigzag test are overshoot angle, non-dimensionalised time of overshoot angle (OSA), and non-dimensional location (x and y) of ship at the overshoot angle.

(a) Zigzag Maneuver Characteristics

As can be observed from Table 6.4, the 1st OSA of -20°/20° zigzag maneuver using computations with G1 matched well with both the experimental data set (E%D ≈ 2%). However, the 2nd OSA showed a higher E%D compared to the 1st OSA with a better agreement with MARIN. The yaw rate to portside agreed well with the -20°/20° zigzag experimental data with overestimation of yaw rate to the starboard side hence the over-prediction of overshoot. From Figure 6.11, computations using G1 matched well with IIHR, The University of Iowa for the portside turn while the agreement was better with MARIN when the ship turns to starboard. Computations using G2 showed an opposite trend. The overall E%D (D=IIHR &MARIN) of computations using G1 was lower compared to the BF model. However, computations using G2 showed a higher percentage of error emphasizing the shortcomings of the rudder modelling. The velocity drop, however, was predicted reasonably well with G2 compared to G1.

As can be observed from Table 6.5, the 1st OSA of 20°/20° zigzag maneuver using computations with G1 matched well with the experimental results of MARIN whereas, the E%D of 2nd OSA was comparable for both the experimental data set. On the other hand, the 1st OSA of 20°/20° zigzag maneuver using computations with G2 matched well with the experimental results of IIHR, The University of Iowa and the 2nd OSA had a better agreement with MARIN. A higher velocity drop was predicted by computations using G1 and irregularities were reflected by the same. Even with a better propeller model, the overall E%D (D=IIHR &MARIN) of computations using G1 fared better than the fully discretized propeller. The overall E%D (D=IIHR) showed a slightly higher value compared to the BF model computations [42]. However, the error percentage was comparable to the BF model for experimental data of MARIN.

Computations for the ±10°/10° zigzag maneuver were challenging for both grid systems G1 and G2. The evaluated E%D (D=IIHR & MARIN) using grid system G1 for -10°/10° maneuver was very high whereas computations using grid G2 showed a lower E%D. 10°/10° maneuver showed lower E%D compared to the fully discretized propeller model but the setup fared inadequately when compared to the BF model. The BF model, however, was simulated with a denser grid compared to grid system G1.

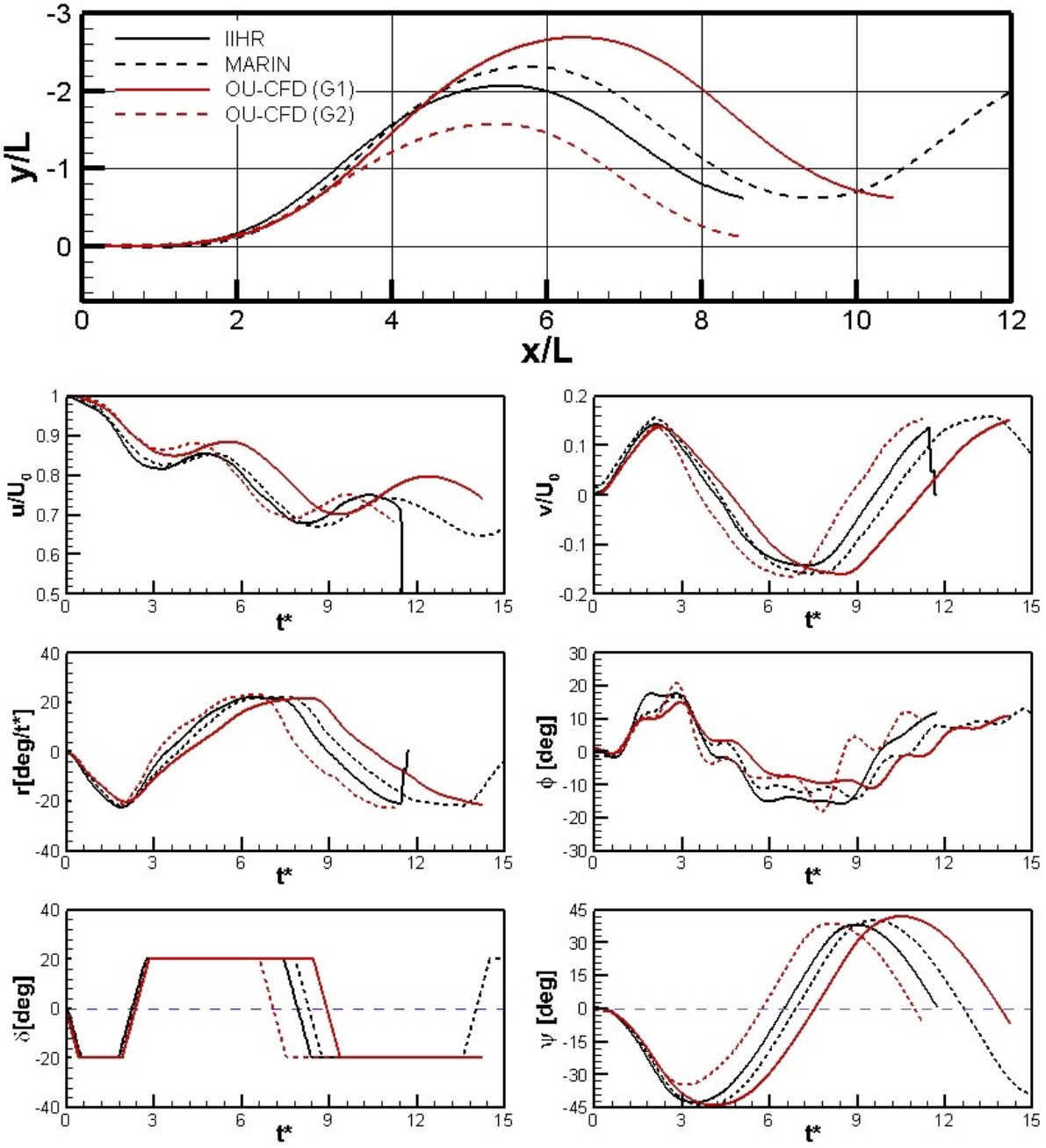

Figure 6.11 Comparison of time histories of motions, motion rates, velocities, rudder and heading angle during the -20°/20° maneuvering simulation.

Table 6.4 Comparison of 1st and 2nd overshoot for -20°/20° maneuver

Parameter			D		S		IIHR-CFD (BF)	E%D (D=IIHR)		E%D (D=MARIN)	
			IIHR	MARIN	OU-CFD G1	OU-CFD G2		G1	G2	G1	G2
-20°/20°	1st	t*	3.63	3.82	4.11	3.11	4.18	-13.22	14.33	-7.59	18.59
		x/L	3.06	3.25	3.53	2.86	3.52	-15.36	6.54	-8.62	12.00
		y/L	-0.86	-0.86	-1.03	-0.52	-1.17	-19.77	39.54	-19.77	39.53
		ψ [deg]	-44.81	-44.40	-44.10	-34.63	-47.92	1.58	22.72	0.68	22.00
		OSA [deg]	24.81	24.40	24.10	14.63	27.92	2.86	41.03	1.23	40.04
	2nd	t*	9.13	9.59	10.52	8.09	9.83	-15.22	11.40	-9.70	15.64
		x/L	6.88	7.12	7.99	6.55	7.35	-16.13	4.80	-12.22	8.01
		y/L	-1.88	-1.81	-2.03	-1.17	-2.24	-7.98	37.77	-12.15	35.36
		ψ [deg]	36.59	40.04	41.82	38.60	44.55	-14.29	-5.49	-4.45	3.60
		OSA [deg]	16.59	20.04	21.82	18.60	24.55	-31.53	-12.12	-8.88	7.19

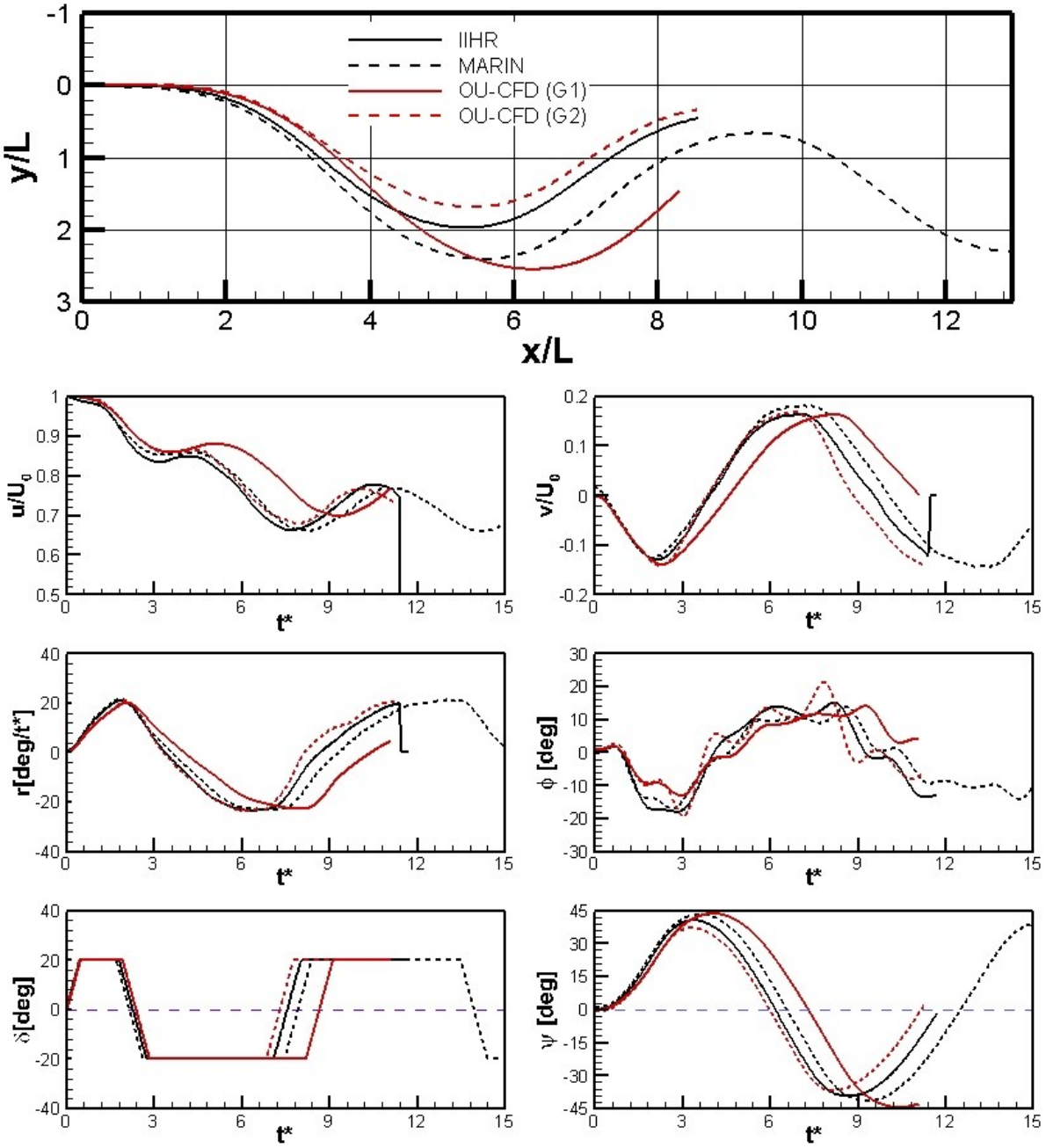

Figure 6.12 Comparison of time histories of motions, motion rates, velocities, rudder and heading angle during the 20°/20° maneuvering simulation.

Table 6.5 Comparison of 1st and 2nd overshoot for 20°/20° maneuver

Parameter			D		S		IIHR-CFD (DP)	IIHR-CFD (BF)	E%D (D=IIHR)		E%D (D=MARIN)	
			IIHR	MARIN	OU-CFD G1	OU-CFD G2			G1	G2	G1	G2
20°/20°	1st	t*	3.36	3.63	4.04	3.32	3.81	4.06	-20.24	1.19	-11.30	8.54
		x/L	3.02	3.11	3.51	3.03	3.29	3.53	-16.23	-0.33	-12.75	2.67
		y/L	0.68	0.95	0.98	0.57	0.94	1.05	-44.12	16.18	-2.73	40.25
		ψ [deg]	39.35	43.22	43.56	37.04	44.05	44.36	-10.70	5.87	-0.79	14.30
		OSA [deg]	19.35	23.22	23.56	17.04	24.05	24.36	-21.76	11.94	-1.46	26.61
	2nd	t*	8.59	9.34	10.41	8.14	9.59	10.22	-21.19	5.24	-11.41	12.89
		x/L	6.62	6.89	7.92	6.50	7.34	7.72	-19.64	1.81	-14.50	5.62
		y/L	1.31	1.91	1.81	1.37	1.70	1.84	-38.17	-4.58	5.09	28.16
		ψ [deg]	-41.81	-41.58	-44.47	-37.02	-44.42	-45.67	-6.36	11.46	-6.95	10.97
		OSA [deg]	21.81	21.58	24.47	17.02	24.42	25.67	-12.20	21.96	-13.39	21.13

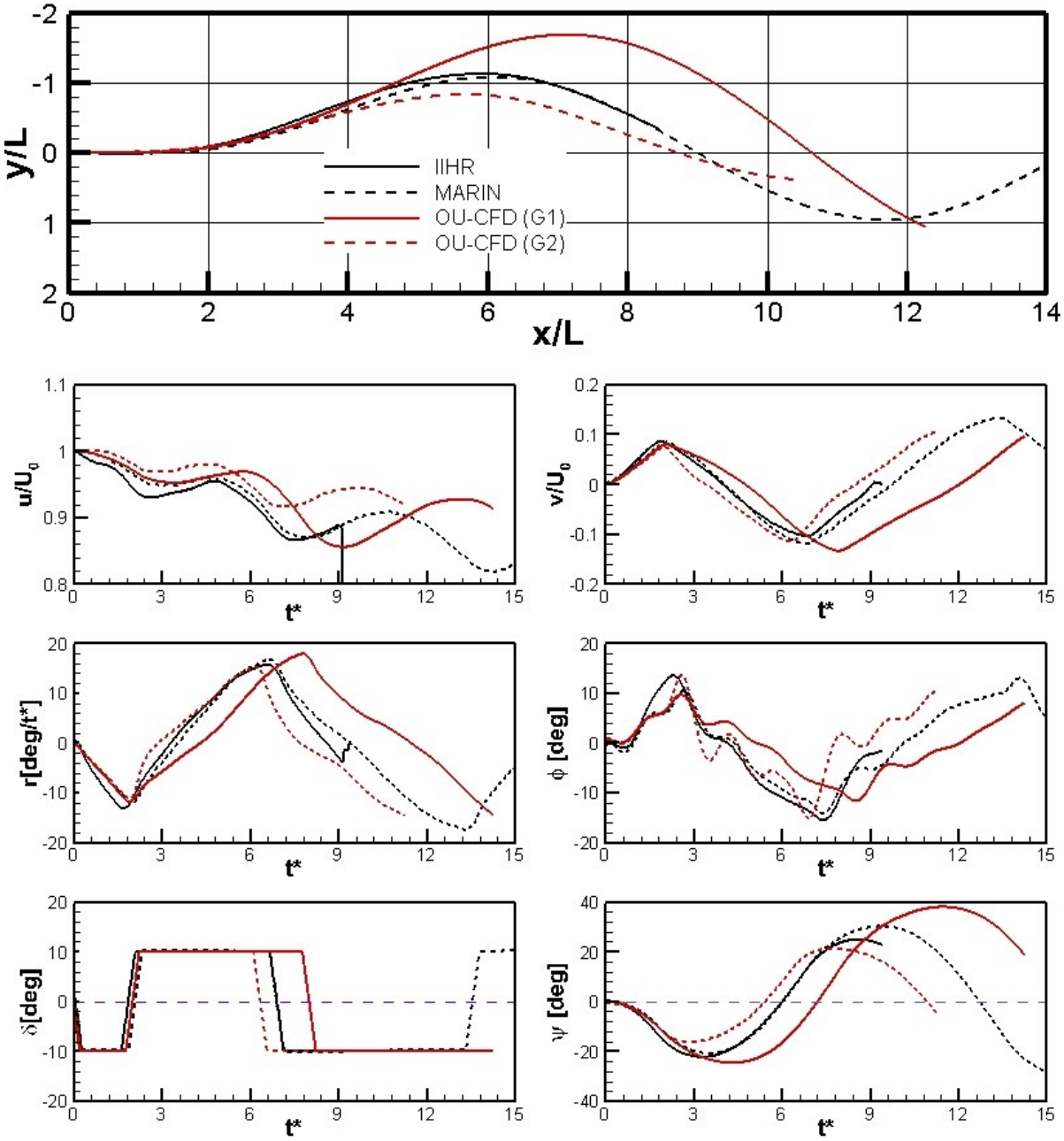

Figure 6.13 Comparison of time histories of motions, motion rates, velocities, rudder and heading angle during the -10°/10° maneuvering simulation.

Table 6.6 Comparison of 1st and 2nd overshoot for -10°/10° maneuver

Parameter			D		S		IIHR-CFD (DP)	IIHR-CFD (BF)	E%D (D=IIHR)		E%D (D=MARIN)	
			IIHR	MARIN	OU-CFD G1	OU-CFD G2			G1	G2	G1	G2
-10°/10°	1st	t*	3.41	3.53	4.30	2.86	3.63	4.19	-26.10	16.13	-21.81	18.98
		x/L	3.22	3.37	4.08	2.80	3.46	3.91	-26.56	13.04	-20.93	16.91
		y/L	-0.54	-0.40	-0.73	-0.26	-0.59	-0.81	-35.38	51.85	-82.77	35.00
		ψ [deg]	-24.07	-20.76	-24.52	-16.06	-24.33	-27.23	-1.86	33.28	-18.10	22.64
		OSA [deg]	14.07	10.76	14.52	6.06	14.33	17.23	-3.17	56.93	-34.91	43.68
	2nd	t*	8.75	9.42	11.46	7.70	9.28	10.67	-30.97	12.00	-21.66	18.26
		x/L	8.01	8.50	10.13	7.34	8.44	9.50	-26.51	8.36	-19.22	13.65
		y/L	-1.05	-0.29	-0.38	-0.50	-0.83	-1.08	63.48	52.38	-32.23	-72.41
		ψ [deg]	23.01	30.23	37.98	21.28	31.04	33.68	-65.08	7.52	-25.65	29.61
		OSA [deg]	13.01	20.23	27.98	11.28	21.04	23.68	-115.10	13.30	-38.33	44.24

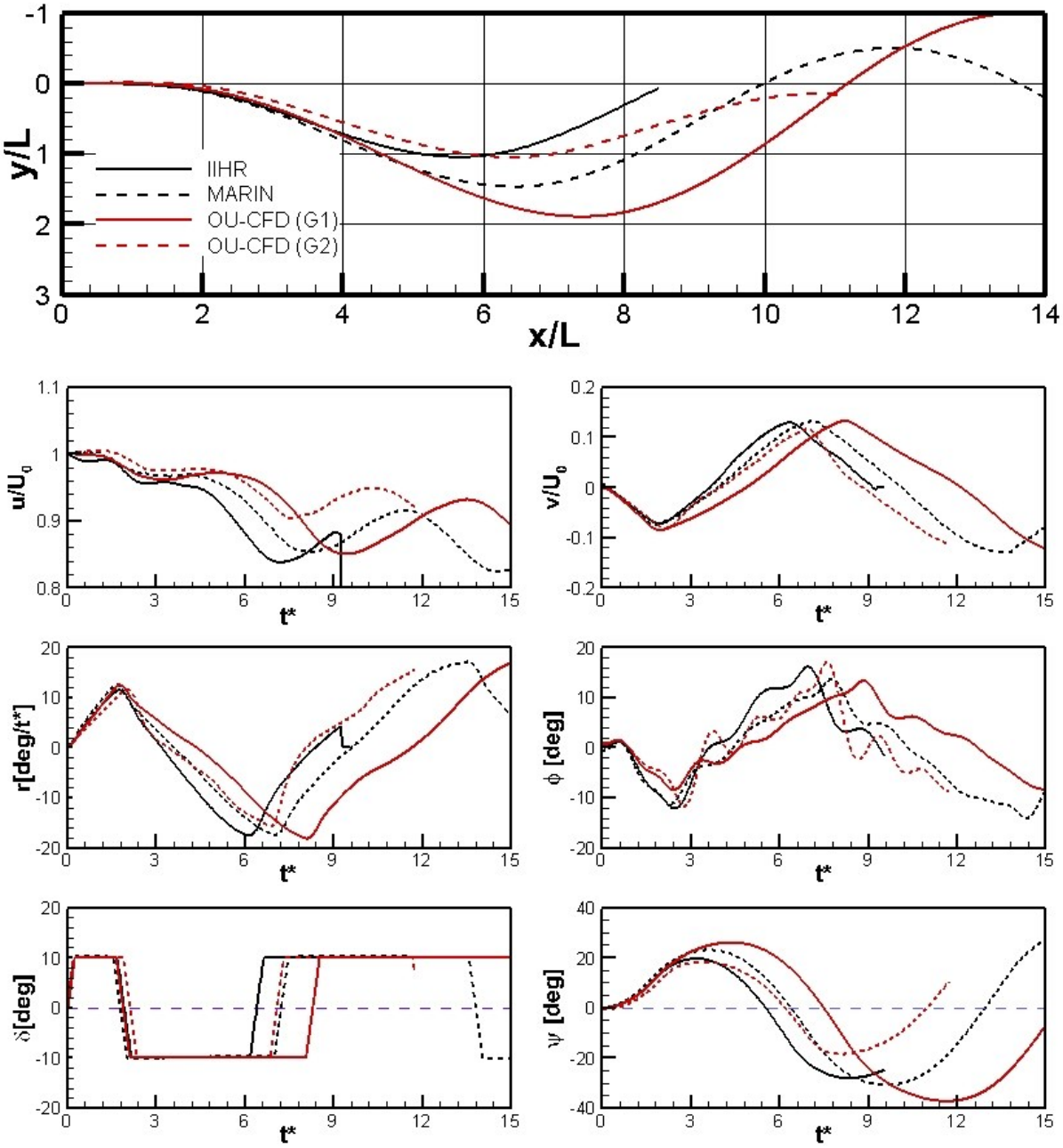

Figure 6.14 Comparison of time histories of motions, motion rates, velocities, rudder and heading angle during the 10°/10° maneuvering simulation.

Table 6.7 Comparison of 1st and 2nd overshoot for 10°/10° maneuver

Parameter			D		S		IIHR-CFD (DP)	IIHR-CFD (BF)	E%D (D=IIHR)		E%D (D=MARIN)	
			IIHR	MARIN	OU-CFD G1	OU-CFD G2			G1	G2	G1	G2
10°/10°	1st	t*	3.08	3.61	4.37	3.41	3.36	3.58	-41.88	-10.80	-21.05	5.47
		x/L	3.02	3.47	4.15	3.35	3.25	3.47	-37.42	-10.93	-19.60	3.37
		y/L	0.36	0.59	0.82	0.35	0.45	0.50	-127.78	2.14	-38.98	40.29
		ψ [deg]	18.55	23.00	25.96	18.23	21.50	21.98	-39.95	1.74	-12.87	20.75
		OSA [deg]	8.55	13.00	15.96	8.23	11.50	11.98	-86.67	3.77	-22.77	36.71
	2nd	t*	8.21	9.60	11.64	8.07	9.31	10.2	-41.78	1.74	-21.25	15.96
		x/L	7.51	8.65	10.29	7.70	8.49	9.09	-37.02	-2.26	-18.96	11.22
		y/L	0.36	0.75	0.66	0.84	0.27	-0.02	-83.33	-133.21	12.00	-11.94
		ψ [deg]	-29.46	-30.85	-37.28	-18.53	-32.46	-38.07	-26.54	37.08	-20.84	39.92
		OSA [deg]	19.46	20.85	27.28	8.53	22.46	28.07	-40.19	56.14	-30.84	59.07

For both G1 and G2, the yaw rate of 20°/20° and 10°/10° zigzag maneuver when starboard turning agreed well with the experimental data. However, computations using G1 over-predicted the yaw rate to the portside, and the same was reflected in the overestimation of the overshoot. In the case of computations with G2, yaw rate to portside turn showed some underestimation hence the under-prediction of overshoot. On the other hand, the yaw rate to portside of -20°/20° and -10°/10° agreed well with the experimental data. But the yaw rate to starboard turn of -20°/20° and -10°/10° showed deviations.

The overall prediction of zigzag ±20°/20° was better than zigzag ±10°/10°. This was attributed to the early fluctuations of self-propulsion simulations encroaching the ±10°/10° zigzag maneuver whereas, for ±20°/20°, the fluctuations had settled with time. The analysis was promising as it provided insights into the hull-propeller-rudder interaction.

With the progress of the zigzag maneuver, the velocity of the ship decreases. Computations with both grid systems, G1 and G2, captured the trend fairly well and followed the EFD data. On correlating with roll angle, it was noticed that velocity of ship decreased considerably every time the ship reached roll peak angle. This trend was aggravated every time the ship rolled to the port. This behaviour was observed for both zigzag ±20°/20° and ±10°/10°, though less evident in the latter. The speed loss is also related to the drift angle. Both drift angle and roll angle contributed to the speed loss by increasing the resistance in a maneuvering ship. The loss of speed was compensated by increasing the thrust, though the process was complex as the wake velocity, as discussed later in the chapter, changes considerably during the maneuver. Since the velocities were still dropping the periodic behaviour for both sets of maneuver were not reached.

In summary, computations with the BF model [42] fared best when compared to experimental data sets of IIHR & MARIN. The OU propeller model fared reasonably well but the prediction of certain parameters requires further investigation. As mentioned earlier, the grid setup of BF was denser than the grid setup of the OU propeller model and the fully discretized propeller. This reiterated that low fidelity propeller models were capable of handling zigzag maneuver, provided the grid resolution is good. However, using a denser grid with the fully discretised propeller model is computationally exhaustive. Usage of body force propeller models in a fine grid setup could provide the answer.

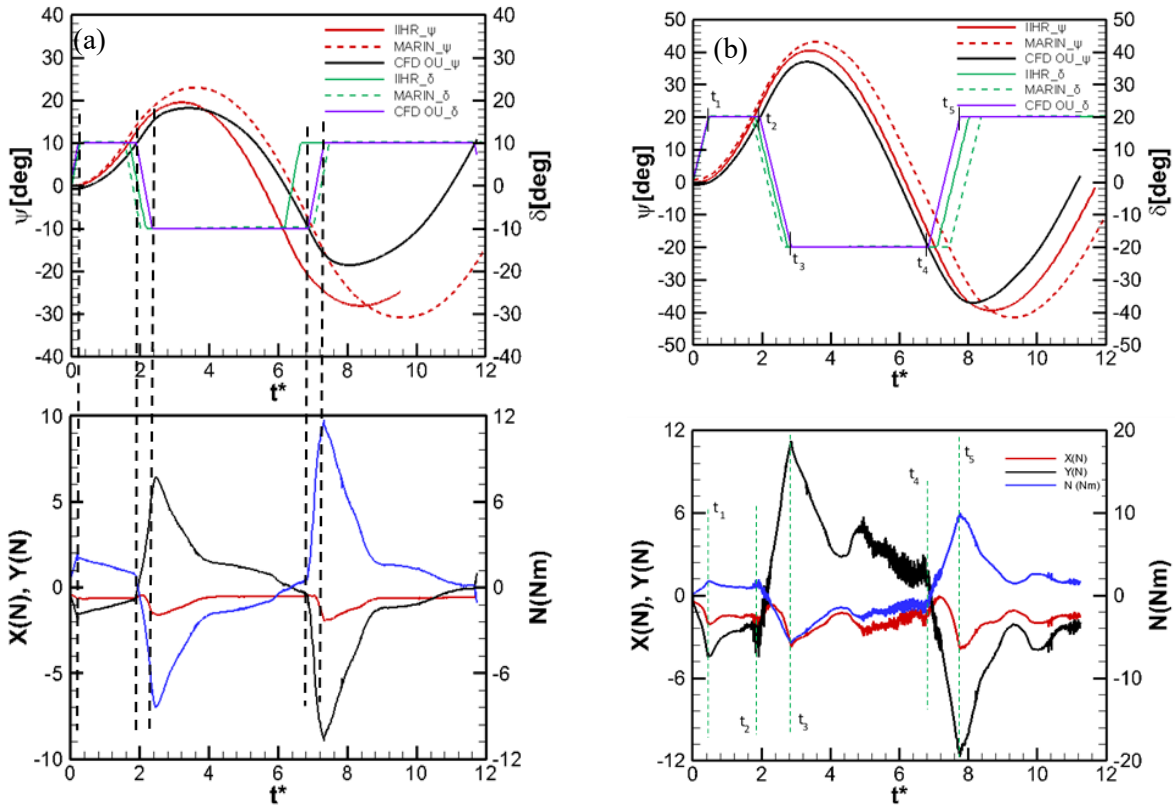

Figure 6.15 Time histories of rudder forces and moment (below) corresponding to the yaw response and rudder angle (top) during the (a) 10°/10° and (b) 20°/20° maneuvering simulation.

An advantage of CFD over EFD is the availability of rudder forces and moments which are not readily available during experiments. The time histories of rudder forces and moment from computations using G2 for zigzag 10°/10° and zigzag +20°/20° was studied and is shown in Figure 6.15. In the case of zigzag +20°/20°, a minimum rudder resistance was recorded every time the rudder was executed and aligned itself with the flow. When the rudder was operating in the portside, the rudder resistance went up to 5N in the model scale. This increased rudder resistance led to the loss of momentum and consequently to speed drops. The rudder resistance decreased fairly smoothly with a sudden drop in resistance when the rudder was operated from starboard to port and kept at the port. In contrast, the transition was smooth when the rudder moved from port to starboard and kept at starboard. The predicted rudder force was higher in the starboard side for the third execute than in the first execute. On correlating speed drops and rudder resistance, it was noticed that with the movement of the rudder from port to starboard or starboard to port, speed loss was recorded. But when the rudder remained at port or at starboard, the resistance of the rudder decreased hence speed recoveries were observed. Increased vibration was recorded for yaw moment when operating on the port side. In the case of zigzag +10°/10°, a similar trend was observed.

(b) Free-surface Analysis

The maneuver was analysed for the axial velocity at the free surface (see Figure 6.16) and free-surface elevation (see Figure 6.17). Four different stages of the 20°/20° maneuver, computed by grid system G2, were studied for free surface elevation and axial velocity contours at the free-surface. Point B and D represent zero yaw while crossing from starboard to port and port to starboard respectively. Point A refers to maximum yaw and Point C represents the minimum yaw.

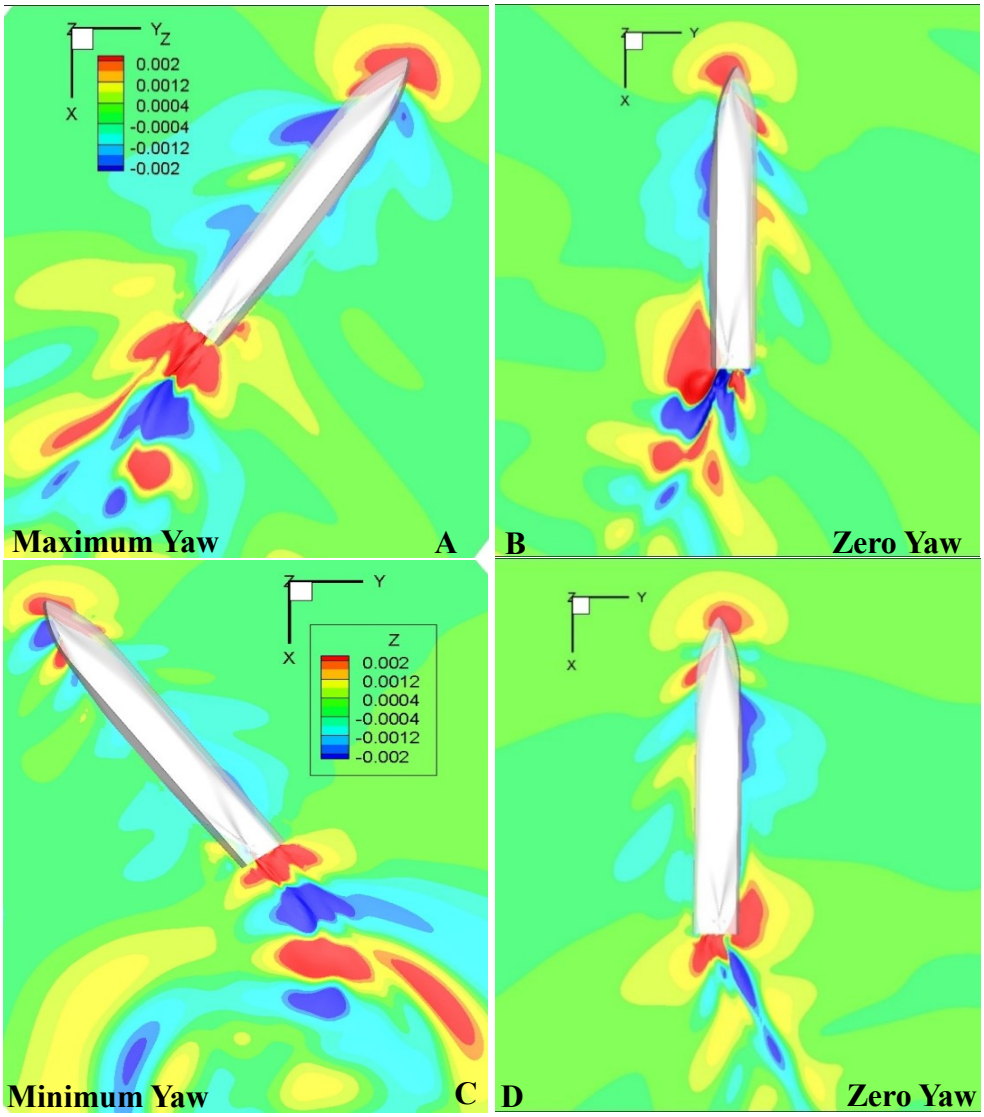

Figure 6.16 Free surface elevation for different stages of the 20°/20° maneuver.

From Figure 6.16, it was noticed that at points B and D (zero yaw while crossing from starboard to port and to starboard respectively): Ship and Propeller wakes were aligned following the trajectory. The opposite situation was observed at Point A and Point C. At Point A, the ship had maximum heading to the starboard with the rudder deflected to port.

The ship wake near the free surface was directed to port, due to rudder deflection to port whereas the propeller was still at starboard with the propeller wake following the trajectory. Thus the split of wake in two directions was observed. Similarly, for point C. A similar trend was reported in [15]. The splitting of wake in two directions was also hinted in the images with the velocity at the free surface.

Figure 6.17 represents the free-surface coloured with the axial velocity at the same stages of zigzag 20°/20° maneuver as explained earlier. As can be clearly depicted from the images, *low-velocity ship wake* extends close to the ship whereas *high-velocity ship wake* reaches the free surface farther out. This could result from the interaction of propeller wake with the rudder thereby sending high-speed flow closer to the free surface.

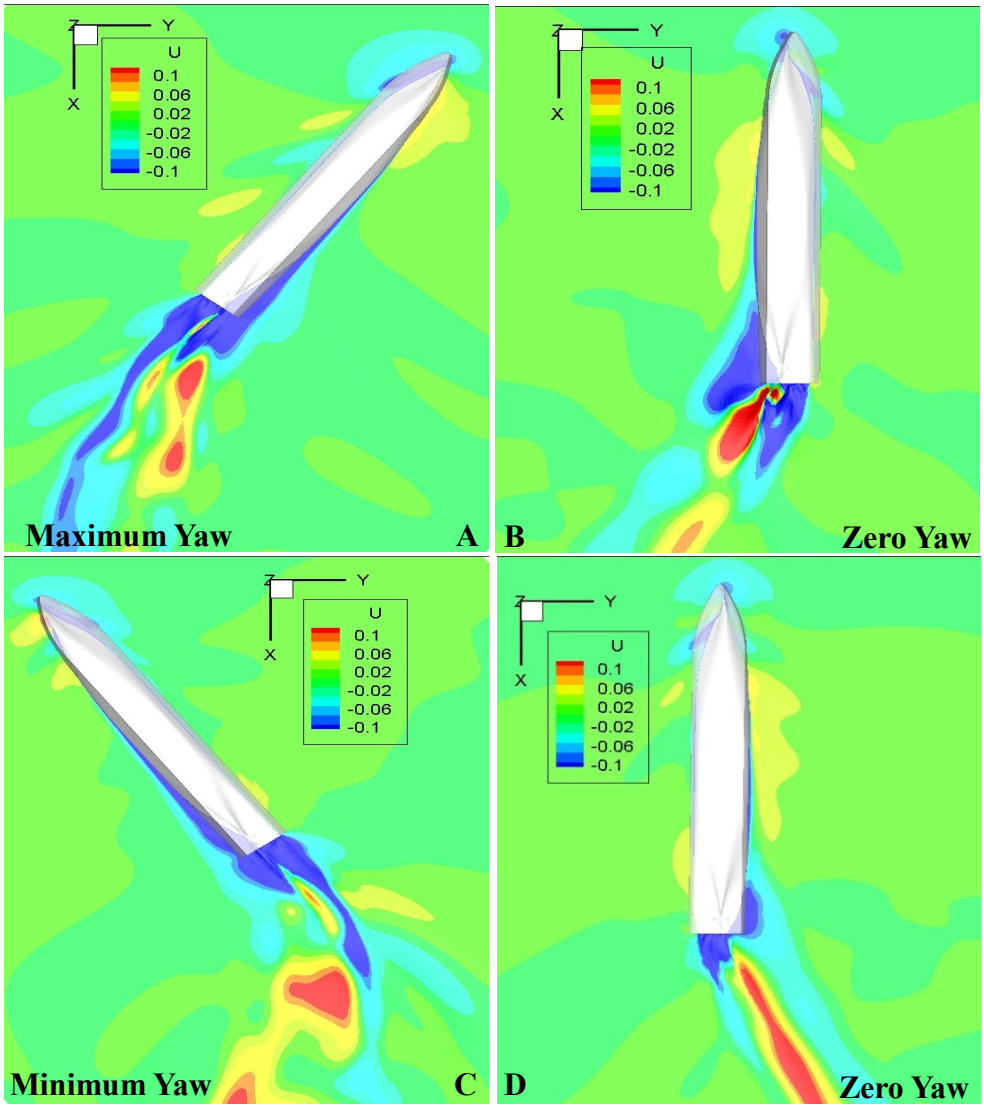

Figure. 6.17 Free surface coloured with U-velocity for different stages of the 20°/20° maneuver.

(c) Axial Velocity Contours

The axial velocity contours at various time steps of one period of the zigzag 20°/20° maneuver, as shown in Figure 6.18 and Figure 6.19, were studied for two cross-sections: x/L =0.975 (upstream of the propeller) and x/L =1.01 (downstream of the propeller).

The evolution of the boundary layer during the maneuver was evident, with the solid surface marked with blue contour (velocity was zero). The flow field was normalized using the initial speed at the start of the maneuver. The speed drops and recoveries were evident from the velocity of the background which was the same as the ship speed at the instantaneous time step. Due to yawing motion generated by the rudder angle deflection, the symmetricity of the flow was disturbed and the distortion was evident. The asymmetry was more pronounced as the ship heading and the rudder deflection angle increased. The wake field and the aft-body bilge vortex moved from starboard to port as the yaw motion moved from starboard to port.

A prominent hub vortex was observed, in Figure 6.18, interacting with the bilge vortex as the ship turns. Vortex shedding below the hub was noticed at various instantaneous stages of the maneuver.

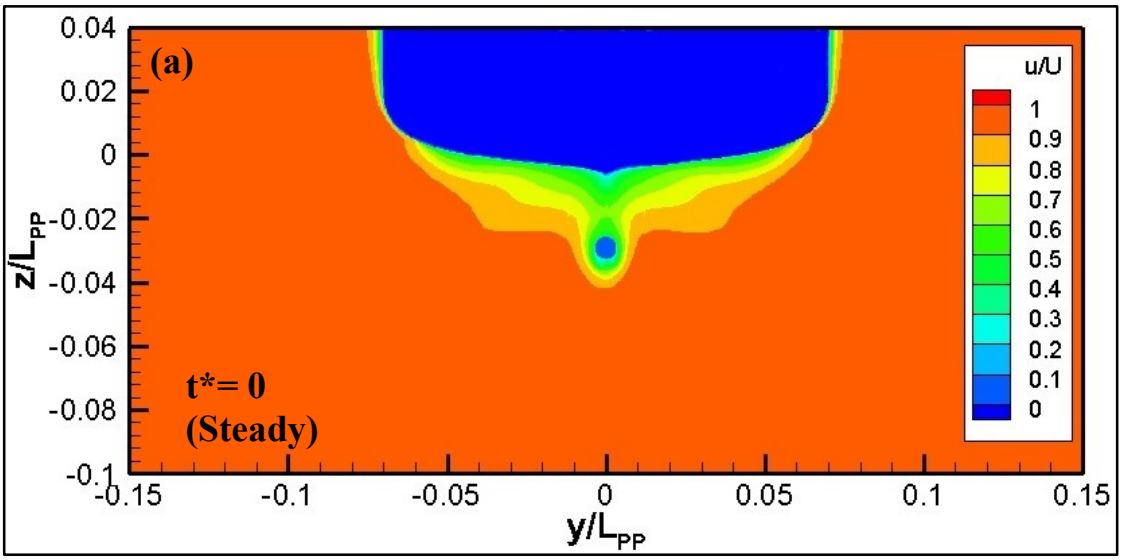
(a)
t*= 0
(Steady)
u/U
1
0.9
0.8
0.7
0.6
0.5
0.4
0.3
0.2
0.1
0
z/L_PP
y/L_PP
0.04
0.02
0
-0.02
-0.04
-0.06
-0.08
-0.1
-0.15
-0.1
-0.05
0
0.05
0.1
0.15

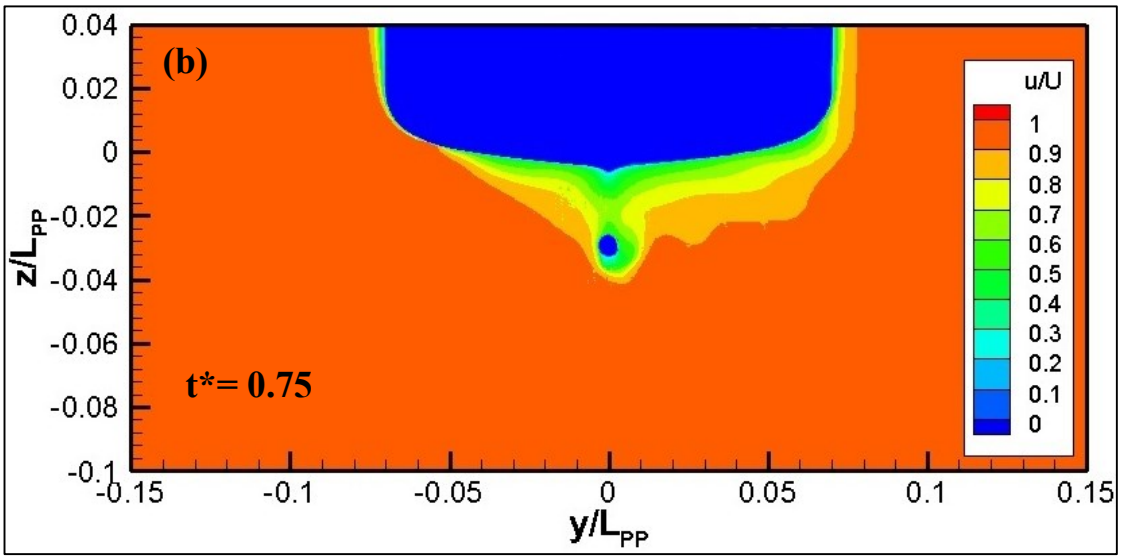
(b)
t*= 0.75
u/U
1
0.9
0.8
0.7
0.6
0.5
0.4
0.3
0.2
0.1
0
z/L_PP
y/L_PP
0.04
0.02
0
-0.02
-0.04
-0.06
-0.08
-0.1
-0.15
-0.1
-0.05
0
0.05
0.1
0.15

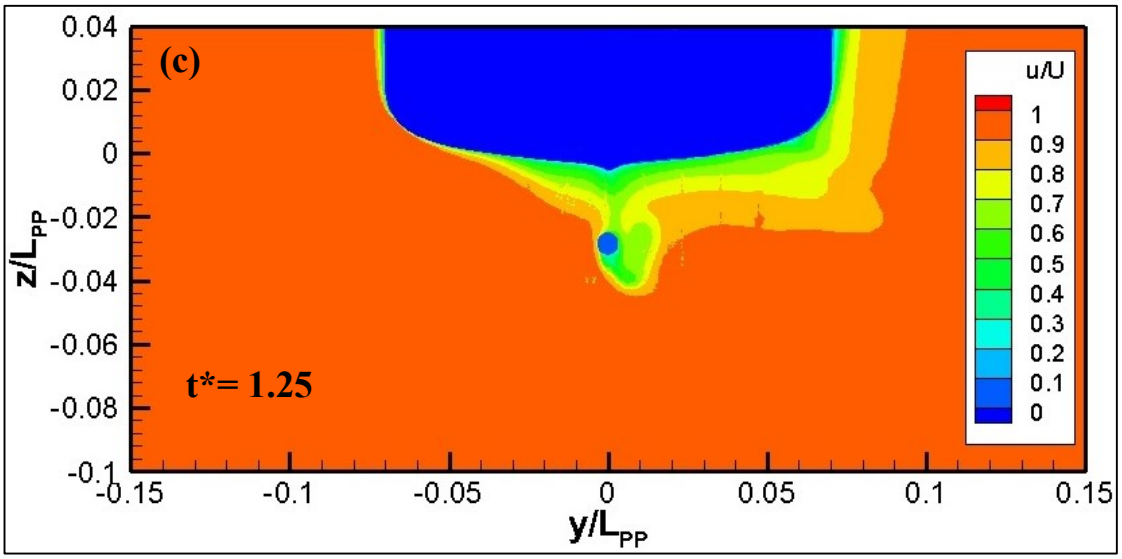
(c)
t*= 1.25
u/U
1
0.9
0.8
0.7
0.6
0.5
0.4
0.3
0.2
0.1
0
z/L_PP
y/L_PP
0.04
0.02
0
-0.02
-0.04
-0.06
-0.08
-0.1
-0.15
-0.1
-0.05
0
0.05
0.1
0.15

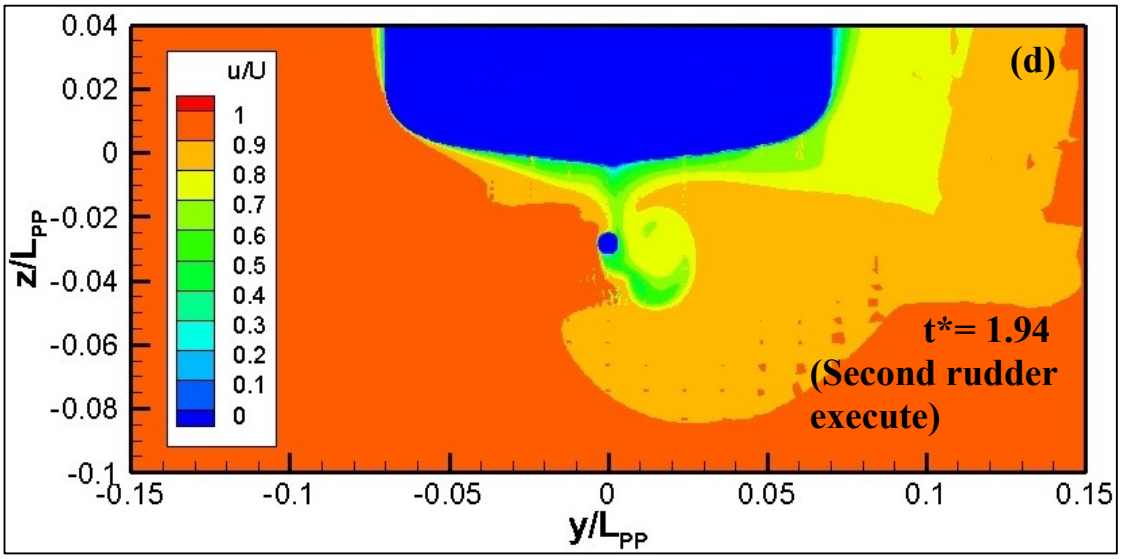
(d)
t*= 1.94
(Second rudder execute)
u/U
1
0.9
0.8
0.7
0.6
0.5
0.4
0.3
0.2
0.1
0
z/L_PP
y/L_PP
0.04
0.02
0
-0.02
-0.04
-0.06
-0.08
-0.1
-0.15
-0.1
-0.05
0
0.05
0.1
0.15

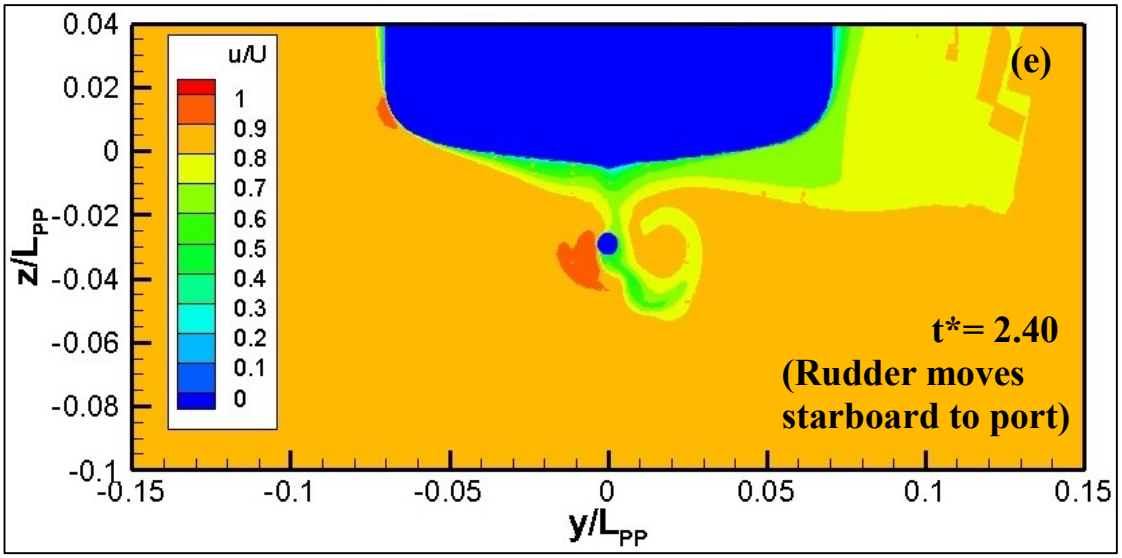
(e)
t*= 2.40
(Rudder moves starboard to port)
u/U
1
0.9
0.8
0.7
0.6
0.5
0.4
0.3
0.2
0.1
0
z/L_PP
y/L_PP
0.04
0.02
0
-0.02
-0.04
-0.06
-0.08
-0.1
-0.15
-0.1
-0.05
0
0.05
0.1
0.15

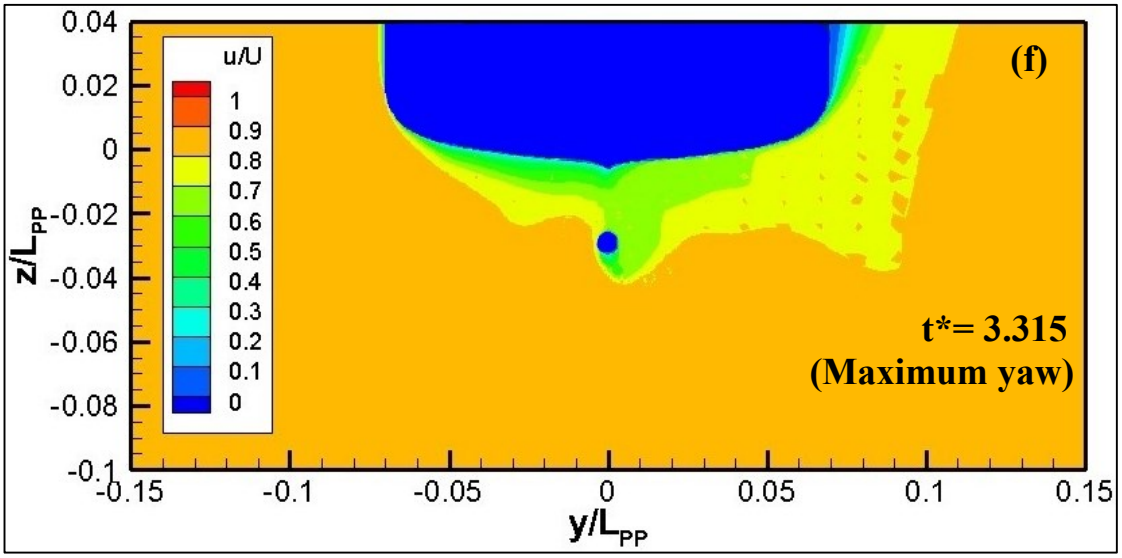
(f)
t*= 3.315
(Maximum yaw)
u/U
1
0.9
0.8
0.7
0.6
0.5
0.4
0.3
0.2
0.1
0
z/L_PP
y/L_PP
0.04
0.02
0
-0.02
-0.04
-0.06
-0.08
-0.1
-0.15
-0.1
-0.05
0
0.05
0.1
0.15

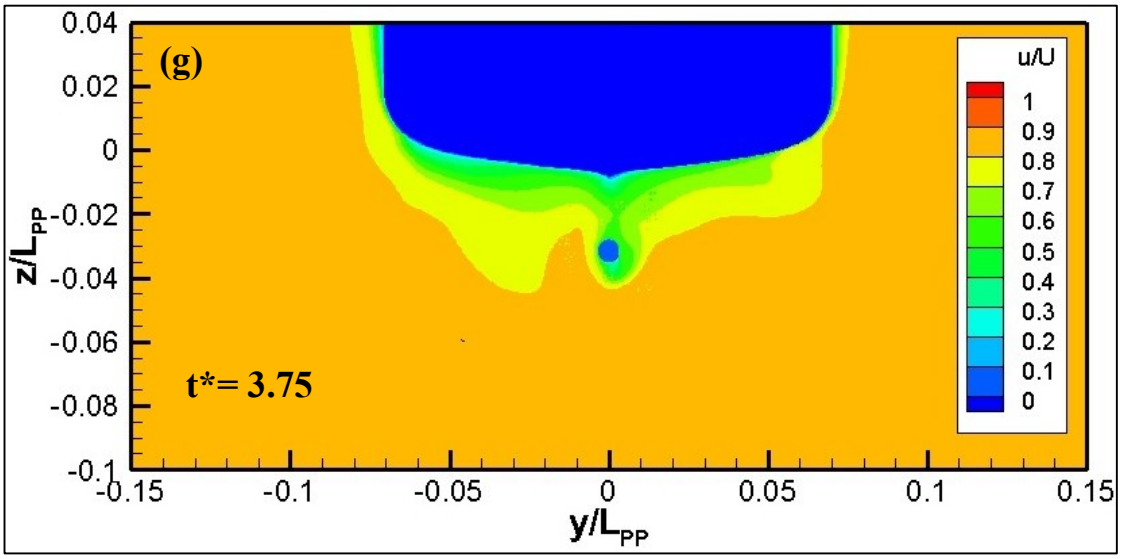
(g)
t*= 3.75
u/U
1
0.9
0.8
0.7
0.6
0.5
0.4
0.3
0.2
0.1
0
z/L_PP
y/L_PP
0.04
0.02
0
-0.02
-0.04
-0.06
-0.08
-0.1
-0.15
-0.1
-0.05
0
0.05
0.1
0.15

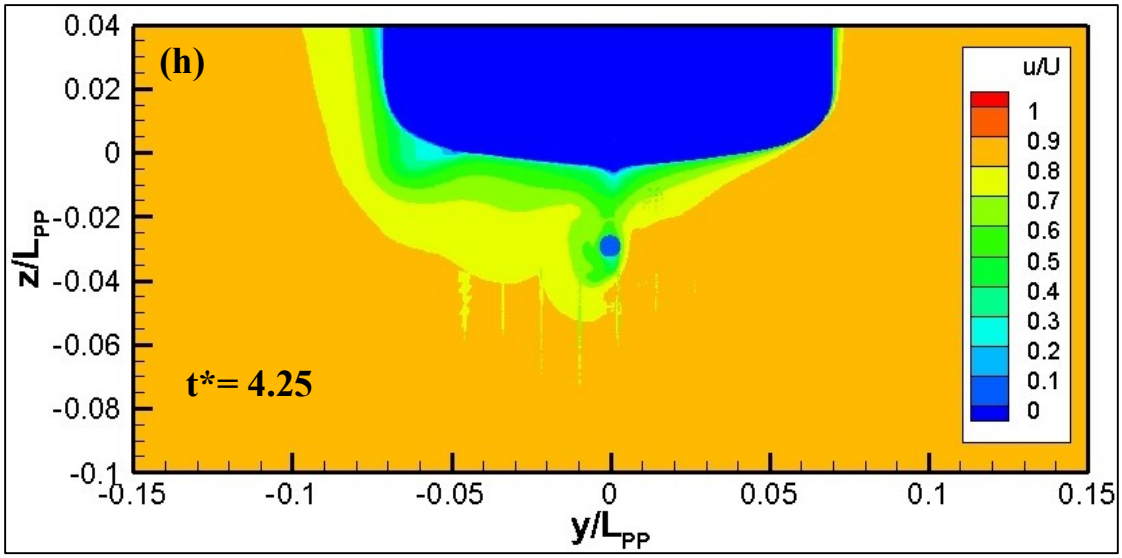
(h)
t*= 4.25
u/U
1
0.9
0.8
0.7
0.6
0.5
0.4
0.3
0.2
0.1
0
z/L_PP
y/L_PP
0.04
0.02
0
-0.02
-0.04
-0.06
-0.08
-0.1
-0.15
-0.1
-0.05
0
0.05
0.1
0.15

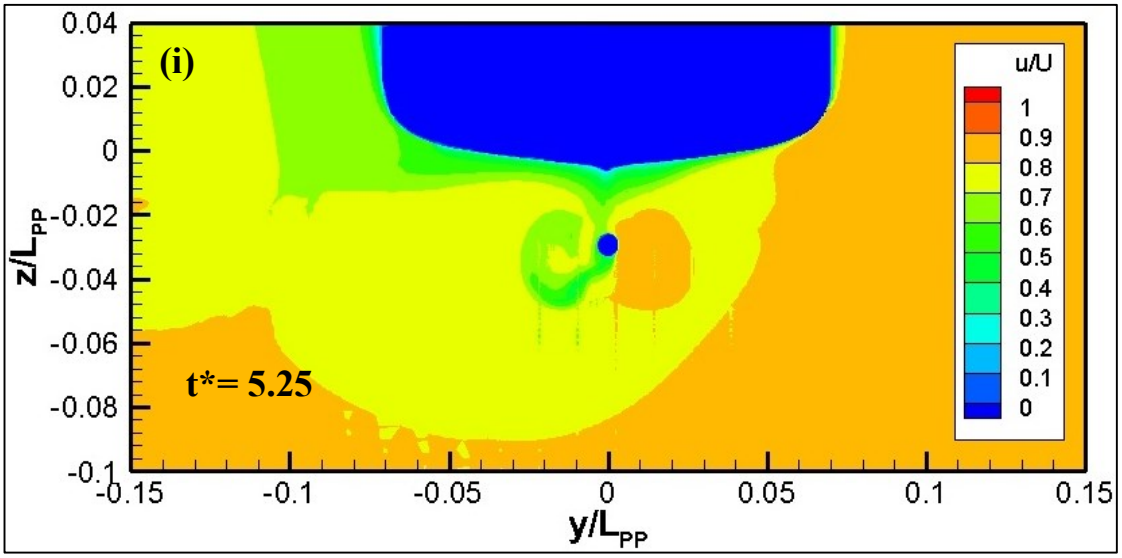
(i)
t*= 5.25
u/U
1
0.9
0.8
0.7
0.6
0.5
0.4
0.3
0.2
0.1
0
z/L_PP
y/L_PP
0.04
0.02
0
-0.02
-0.04
-0.06
-0.08
-0.1
-0.15
-0.1
-0.05
0
0.05
0.1
0.15

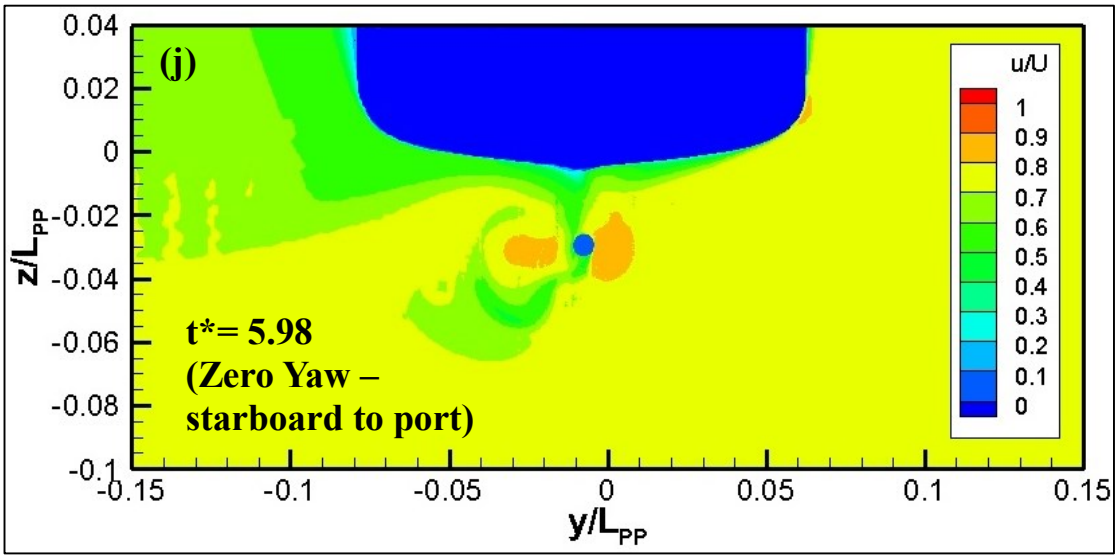
(j)
t*= 5.98
(Zero Yaw –
starboard to port)
u/U
1
0.9
0.8
0.7
0.6
0.5
0.4
0.3
0.2
0.1
0
z/L_PP
y/L_PP
0.04
0.02
0
-0.02
-0.04
-0.06
-0.08
-0.1
-0.15
-0.1
-0.05
0
0.05
0.1
0.15

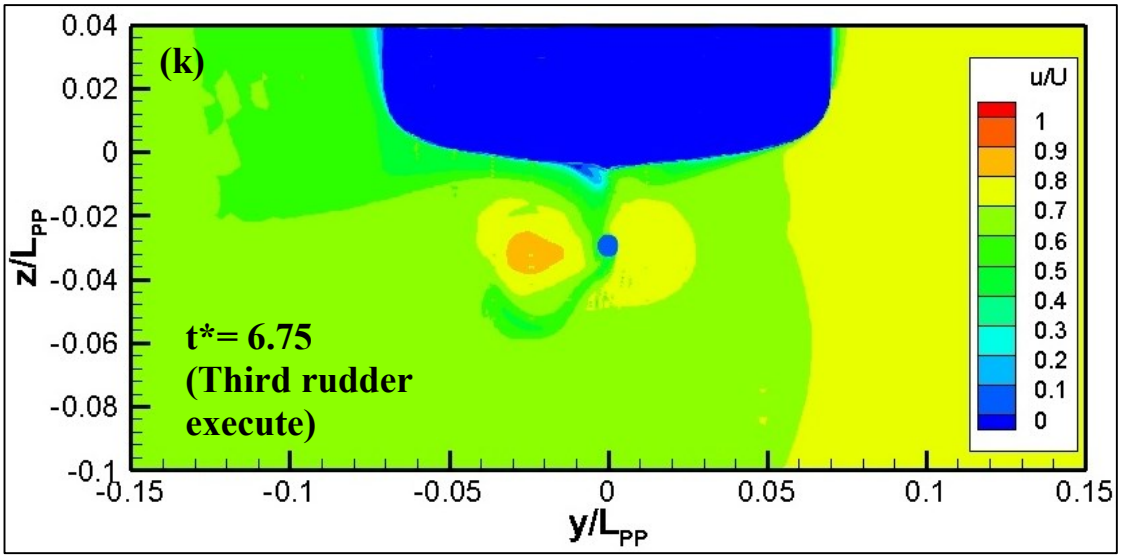
(k)
t*= 6.75
(Third rudder
execute)
u/U
1
0.9
0.8
0.7
0.6
0.5
0.4
0.3
0.2
0.1
0
z/L_PP
y/L_PP
0.04
0.02
0
-0.02
-0.04
-0.06
-0.08
-0.1
-0.15
-0.1
-0.05
0
0.05
0.1
0.15

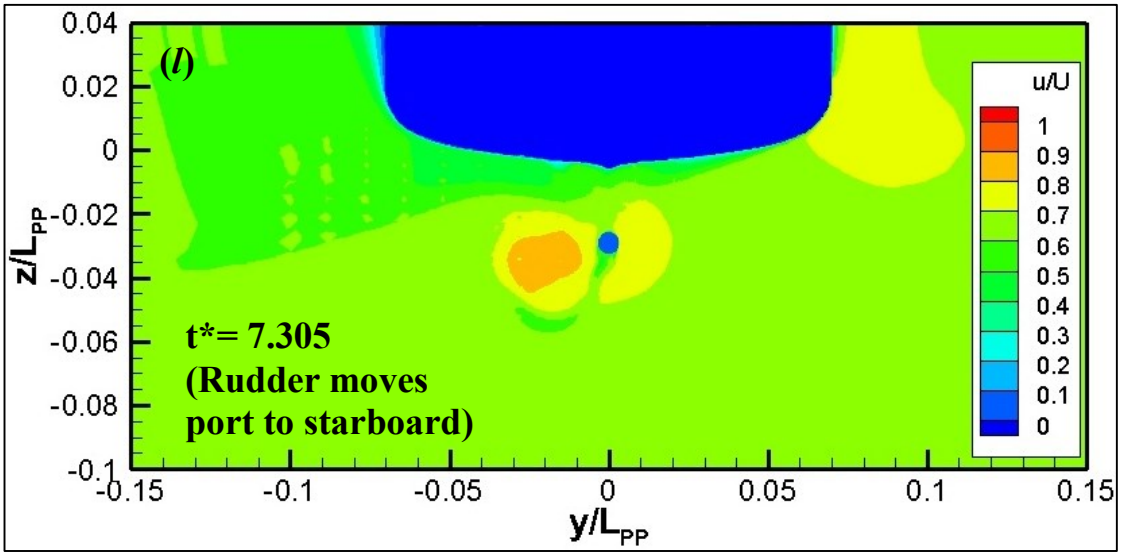
(l)
t*= 7.305
(Rudder moves
port to starboard)
u/U
1
0.9
0.8
0.7
0.6
0.5
0.4
0.3
0.2
0.1
0
z/L_PP
y/L_PP
0.04
0.02
0
-0.02
-0.04
-0.06
-0.08
-0.1
-0.15
-0.1
-0.05
0
0.05
0.1
0.15

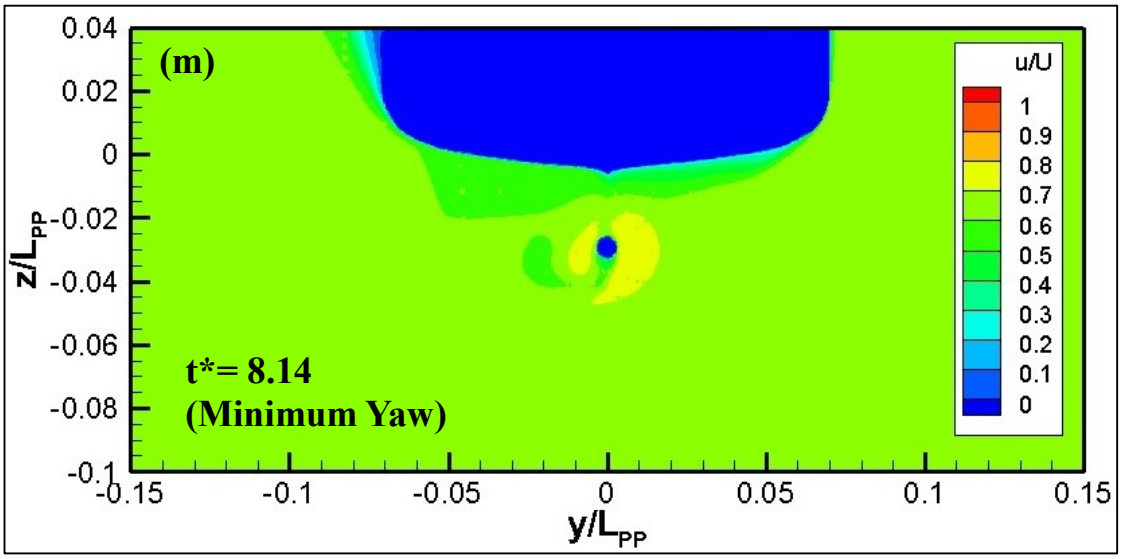
(m)
t*= 8.14
(Minimum Yaw)
u/U
1
0.9
0.8
0.7
0.6
0.5
0.4
0.3
0.2
0.1
0
z/L_PP
y/L_PP
0.04
0.02
0
-0.02
-0.04
-0.06
-0.08
-0.1
-0.15
-0.1
-0.05
0
0.05
0.1
0.15

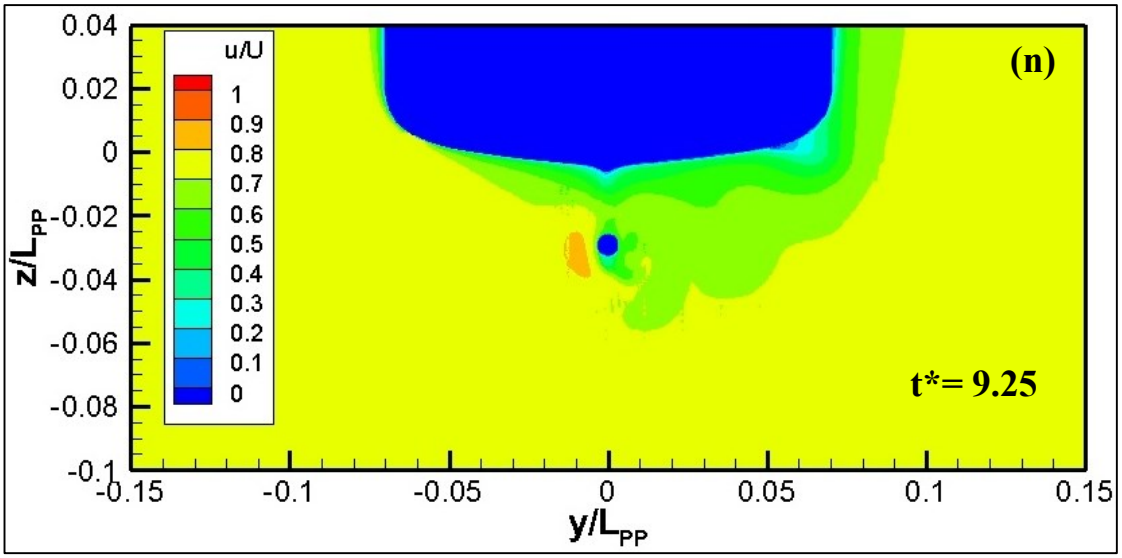
(n)
t*= 9.25
u/U
1
0.9
0.8
0.7
0.6
0.5
0.4
0.3
0.2
0.1
0
z/L_PP
y/L_PP
0.04
0.02
0
-0.02
-0.04
-0.06
-0.08
-0.1
-0.15
-0.1
-0.05
0
0.05
0.1
0.15

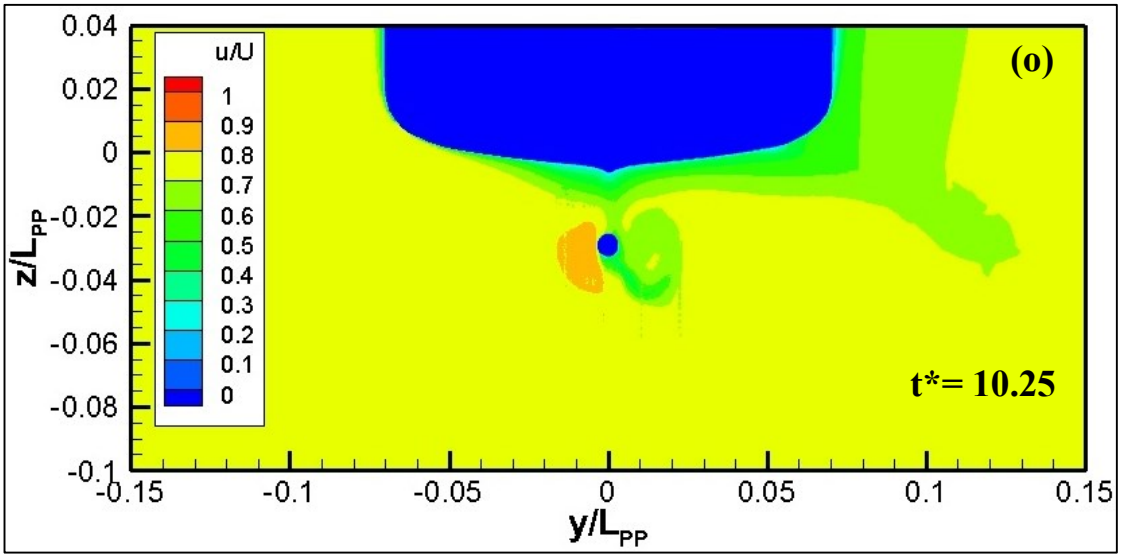
(o)
t*= 10.25
u/U
1
0.9
0.8
0.7
0.6
0.5
0.4
0.3
0.2
0.1
0
z/L_PP
y/L_PP
0.04
0.02
0
-0.02
-0.04
-0.06
-0.08
-0.1
-0.15
-0.1
-0.05
0
0.05
0.1
0.15

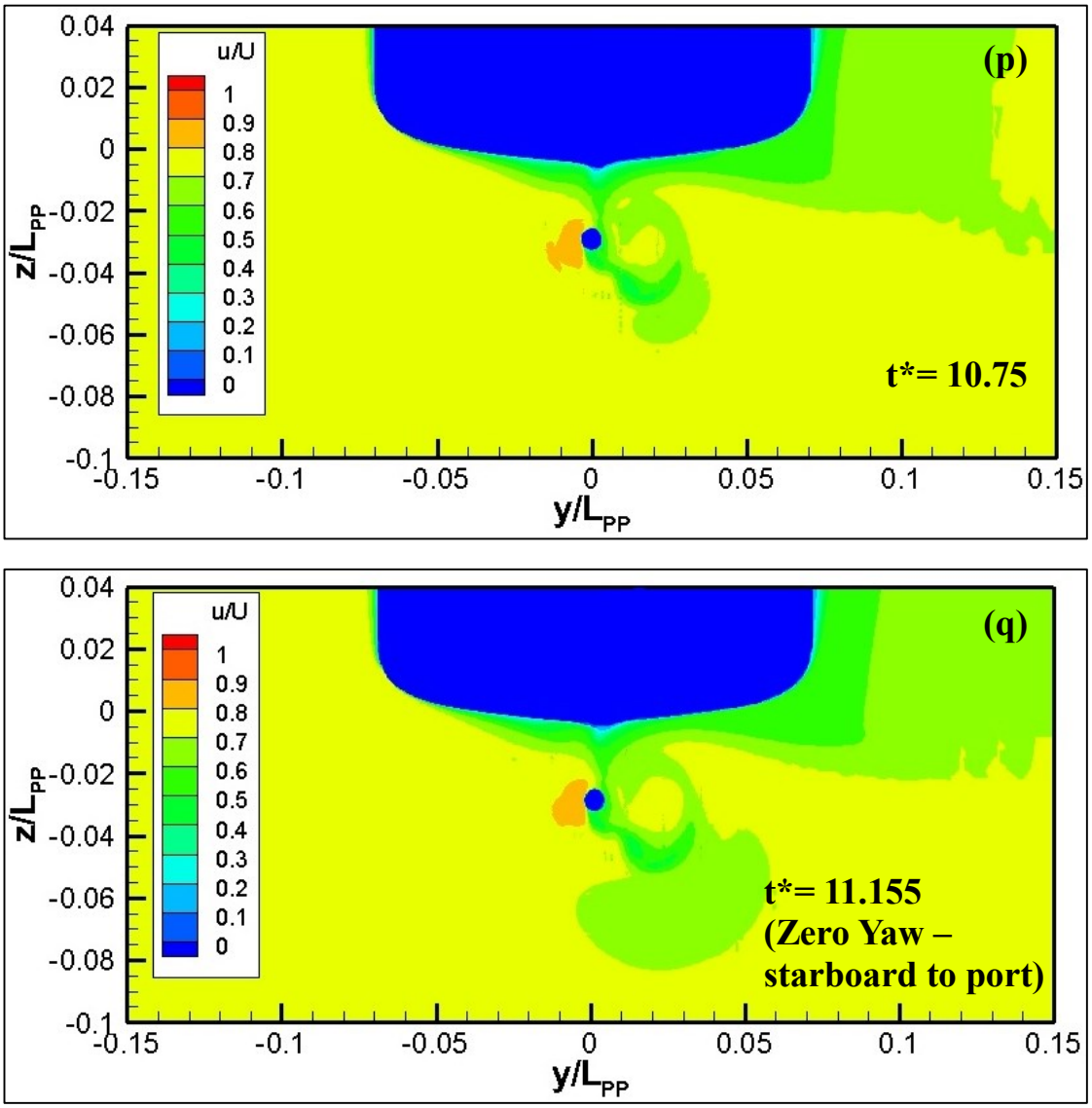

Figure 6.18 Axial Velocity Contours at x/L=0.975 at various time steps of 20°/20°maneuver.

Due to the clockwise propeller action, swirl was introduced in the flow moving port to starboard at the top of the rudder and starboard to port at the bottom of the rudder. This process was clearly observed in Figure 6.19. As pointed out earlier, the high velocity wake of the propeller reached the free surface farther away from the ship whereas the low velocity wake reached the free surface closer to the ship. This process was clearly illustrated in Figure 6.19. A more pronounced separation was observed (Figure 6.19) in the portside of the rudder tip at the instantaneous point of zero yaw turning starboard to port than at the instantaneous point of zero yaw turning port to starboard. A detached separation at the rudder root was only clearly visible at t*=5.25 with maximum rudder angle deflected to port and the ship heading at starboard. As observed in Figure 6.19, the rudder tip vortex created a bulge in the propeller wake thereby pushing it down. A similar observation was pointed out in [15].

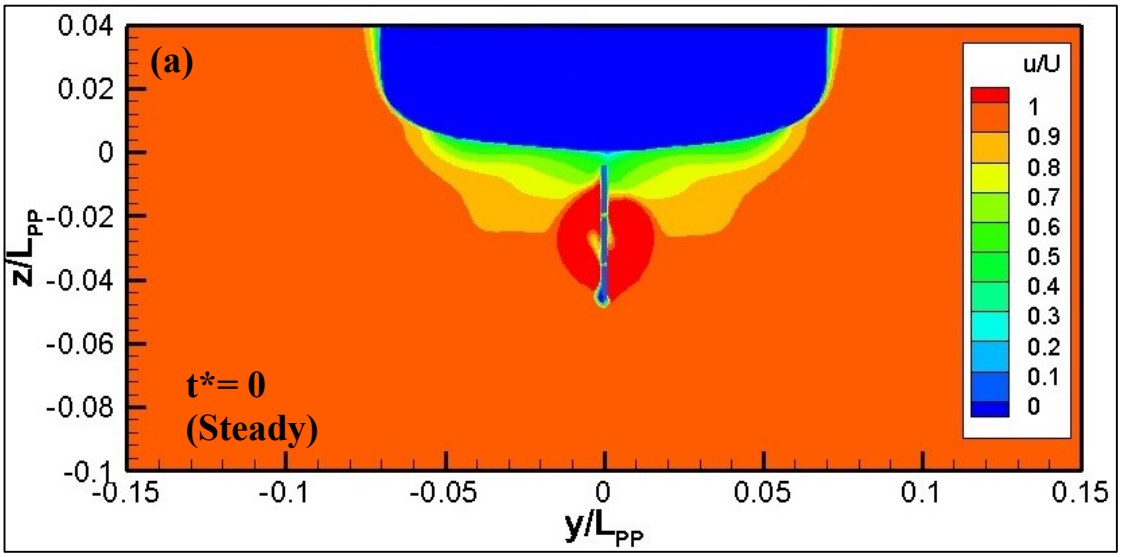
(a)
t*= 0
(Steady)
u/U
1
0.9
0.8
0.7
0.6
0.5
0.4
0.3
0.2
0.1
0
0.04
0.02
0
-0.02
-0.04
-0.06
-0.08
-0.1
z/L_PP
-0.15
-0.1
-0.05
0
0.05
0.1
0.15
y/L_PP

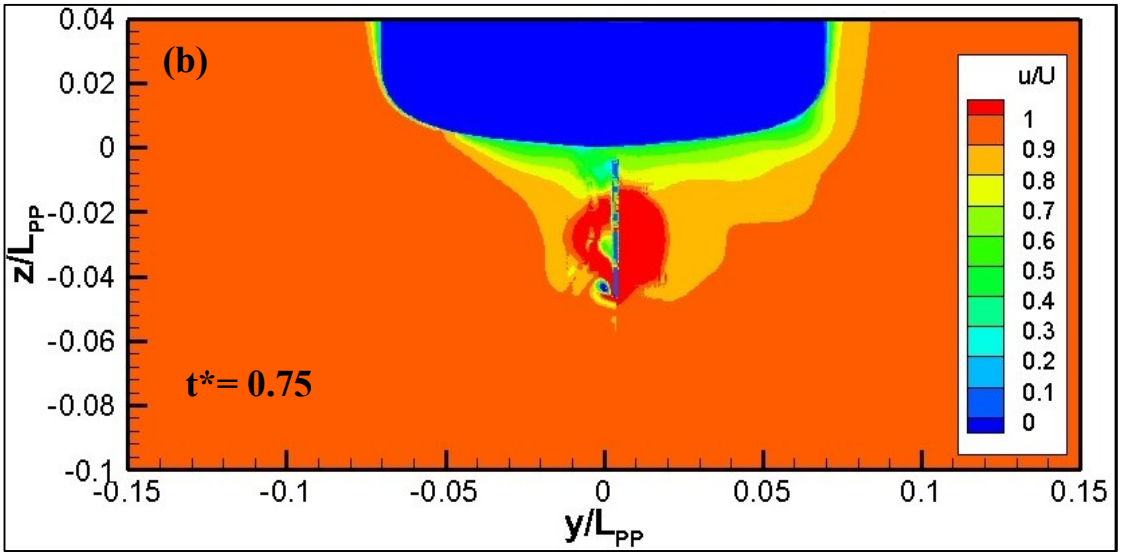
(b)
t*= 0.75
u/U
1
0.9
0.8
0.7
0.6
0.5
0.4
0.3
0.2
0.1
0
0.04
0.02
0
-0.02
-0.04
-0.06
-0.08
-0.1
z/L_PP
-0.15
-0.1
-0.05
0
0.05
0.1
0.15
y/L_PP

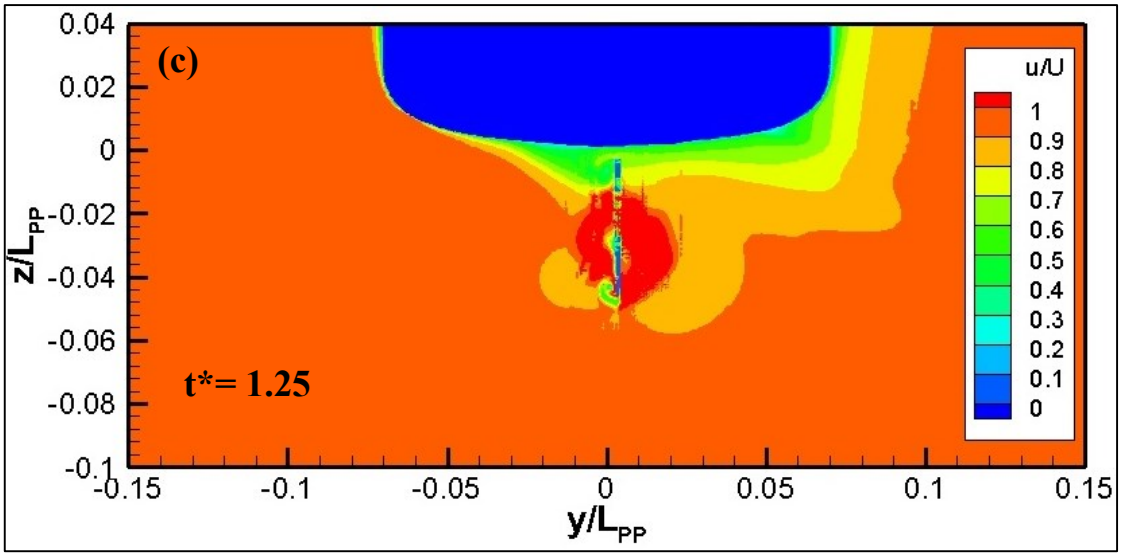
(c)
t*= 1.25
u/U
1
0.9
0.8
0.7
0.6
0.5
0.4
0.3
0.2
0.1
0
0.04
0.02
0
-0.02
-0.04
-0.06
-0.08
-0.1
z/L_PP
-0.15
-0.1
-0.05
0
0.05
0.1
0.15
y/L_PP

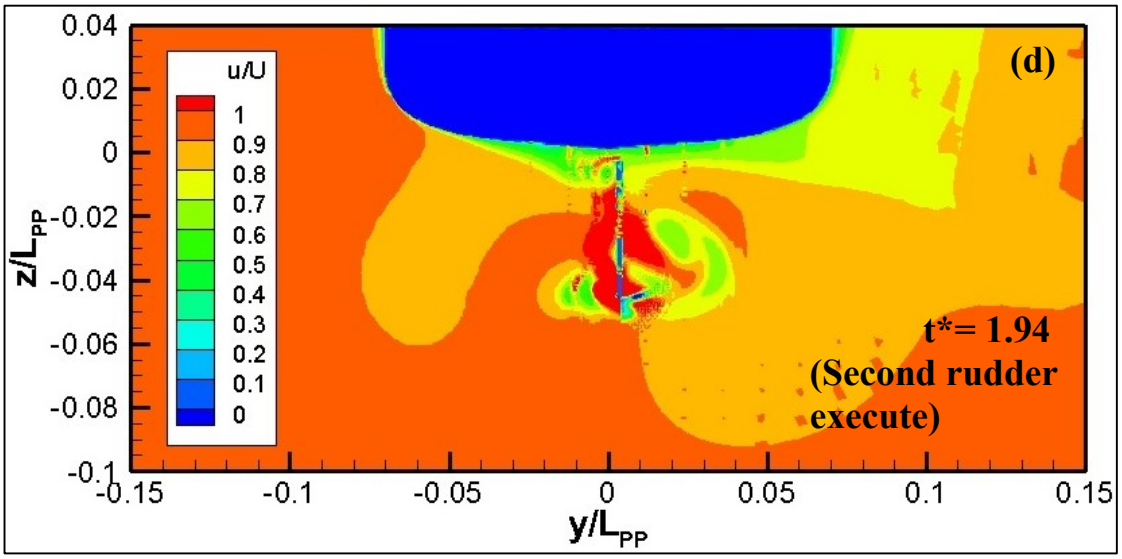
(d)
t*= 1.94
(Second rudder execute)
u/U
1
0.9
0.8
0.7
0.6
0.5
0.4
0.3
0.2
0.1
0
z/L_PP
y/L_PP
0.04
0.02
0
-0.02
-0.04
-0.06
-0.08
-0.1
-0.15
-0.1
-0.05
0
0.05
0.1
0.15

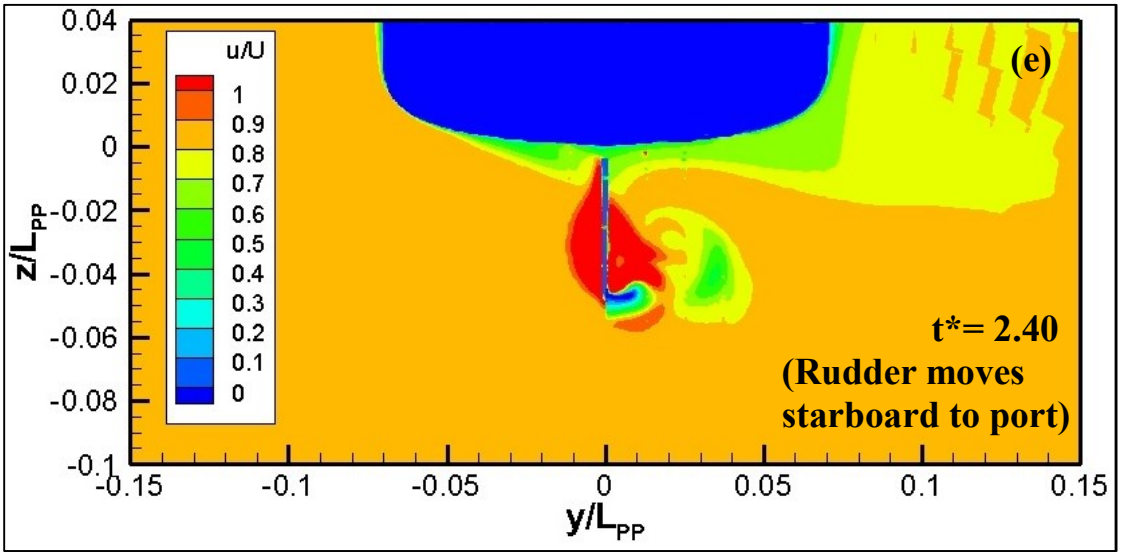
(e)
t*= 2.40
(Rudder moves starboard to port)
u/U
1
0.9
0.8
0.7
0.6
0.5
0.4
0.3
0.2
0.1
0
z/L_PP
y/L_PP
0.04
0.02
0
-0.02
-0.04
-0.06
-0.08
-0.1
-0.15
-0.1
-0.05
0
0.05
0.1
0.15

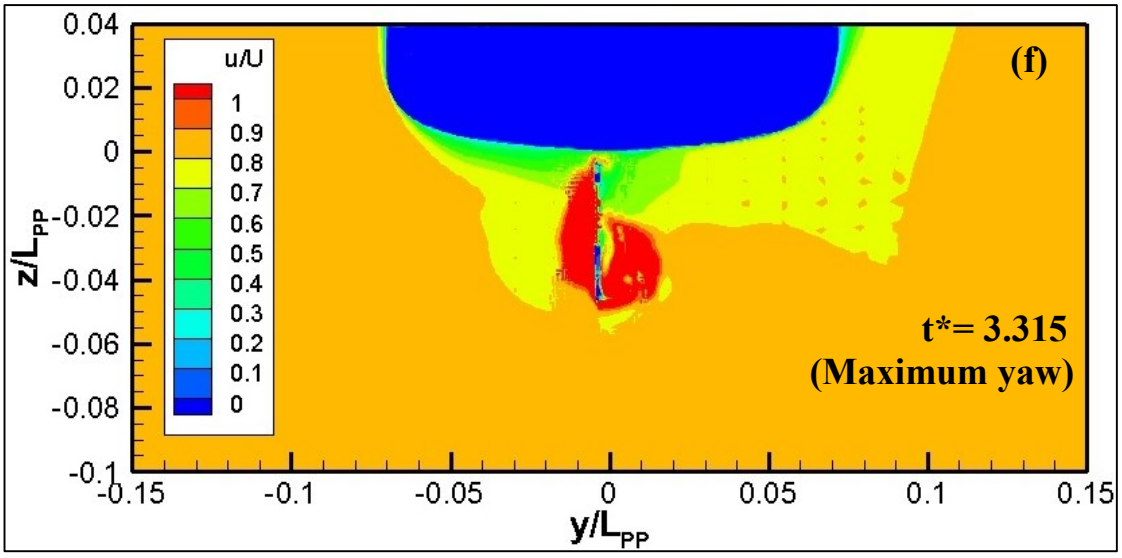
(f)
t*= 3.315
(Maximum yaw)
u/U
1
0.9
0.8
0.7
0.6
0.5
0.4
0.3
0.2
0.1
0
z/L_PP
y/L_PP
0.04
0.02
0
-0.02
-0.04
-0.06
-0.08
-0.1
-0.15
-0.1
-0.05
0
0.05
0.1
0.15

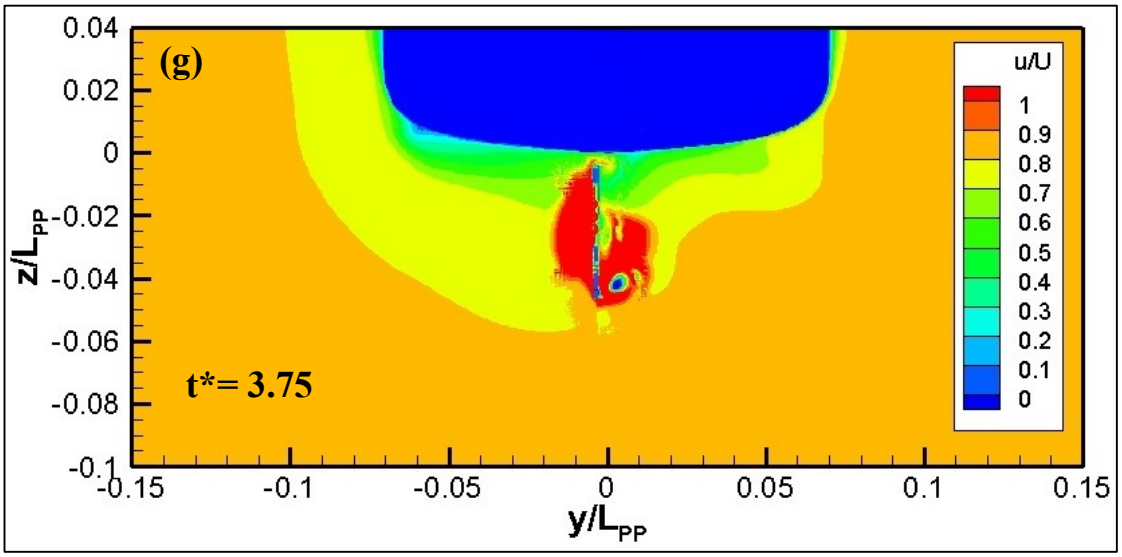
(g)
t*= 3.75
u/U
1
0.9
0.8
0.7
0.6
0.5
0.4
0.3
0.2
0.1
0
z/L_PP
y/L_PP
0.04
0.02
0
-0.02
-0.04
-0.06
-0.08
-0.1
-0.15
-0.1
-0.05
0
0.05
0.1
0.15

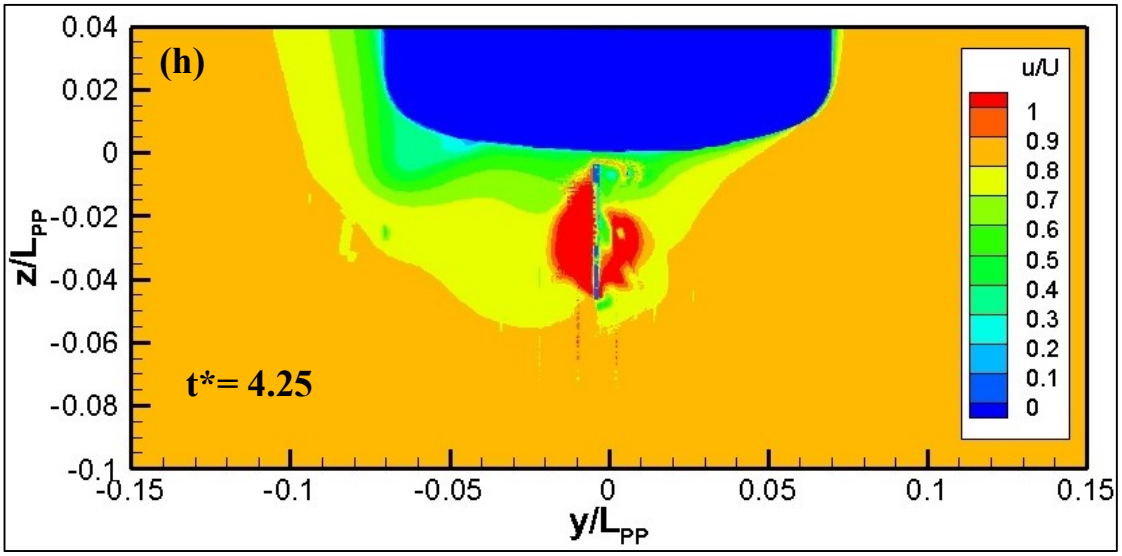
(h)
t*= 4.25
u/U
1
0.9
0.8
0.7
0.6
0.5
0.4
0.3
0.2
0.1
0
z/L_PP
y/L_PP
0.04
0.02
0
-0.02
-0.04
-0.06
-0.08
-0.1
-0.15
-0.1
-0.05
0
0.05
0.1
0.15

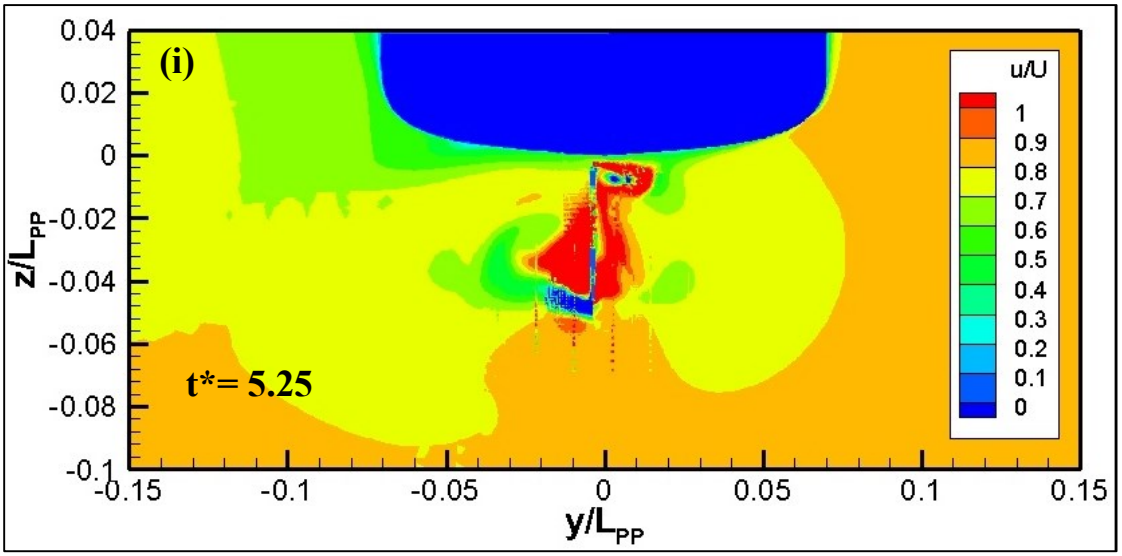
(i)
t*= 5.25
u/U
1
0.9
0.8
0.7
0.6
0.5
0.4
0.3
0.2
0.1
0
z/L_PP
y/L_PP
0.04
0.02
0
-0.02
-0.04
-0.06
-0.08
-0.1
-0.15
-0.1
-0.05
0
0.05
0.1
0.15

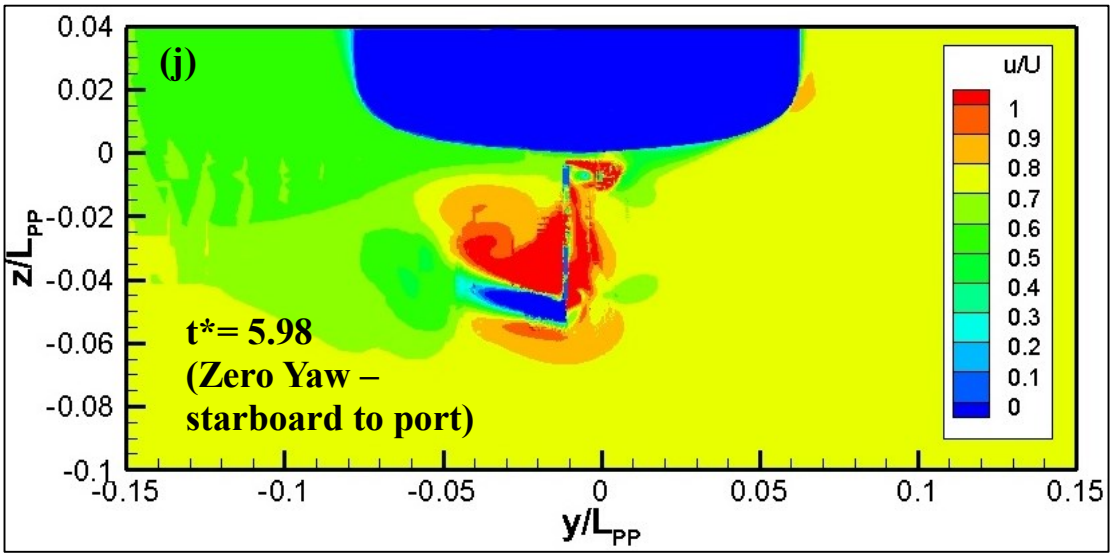
(j)
t*= 5.98
(Zero Yaw –
starboard to port)
u/U
1
0.9
0.8
0.7
0.6
0.5
0.4
0.3
0.2
0.1
0
z/L_PP
y/L_PP
0.04
0.02
0
-0.02
-0.04
-0.06
-0.08
-0.1
-0.15
-0.1
-0.05
0
0.05
0.1
0.15

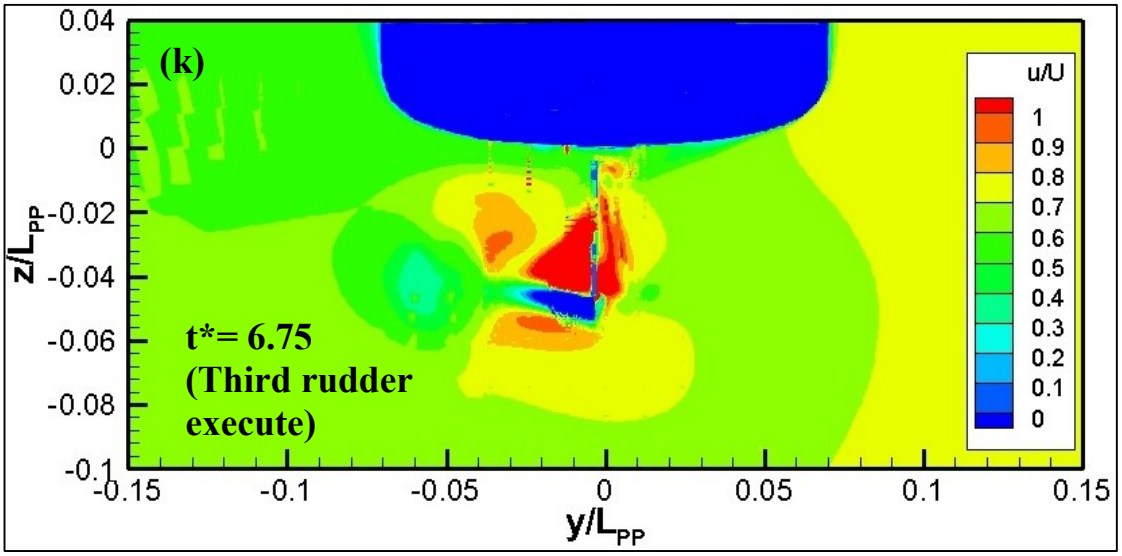
(k)
t*= 6.75
(Third rudder
execute)
u/U
1
0.9
0.8
0.7
0.6
0.5
0.4
0.3
0.2
0.1
0
z/L_PP
y/L_PP
0.04
0.02
0
-0.02
-0.04
-0.06
-0.08
-0.1
-0.15
-0.1
-0.05
0
0.05
0.1
0.15

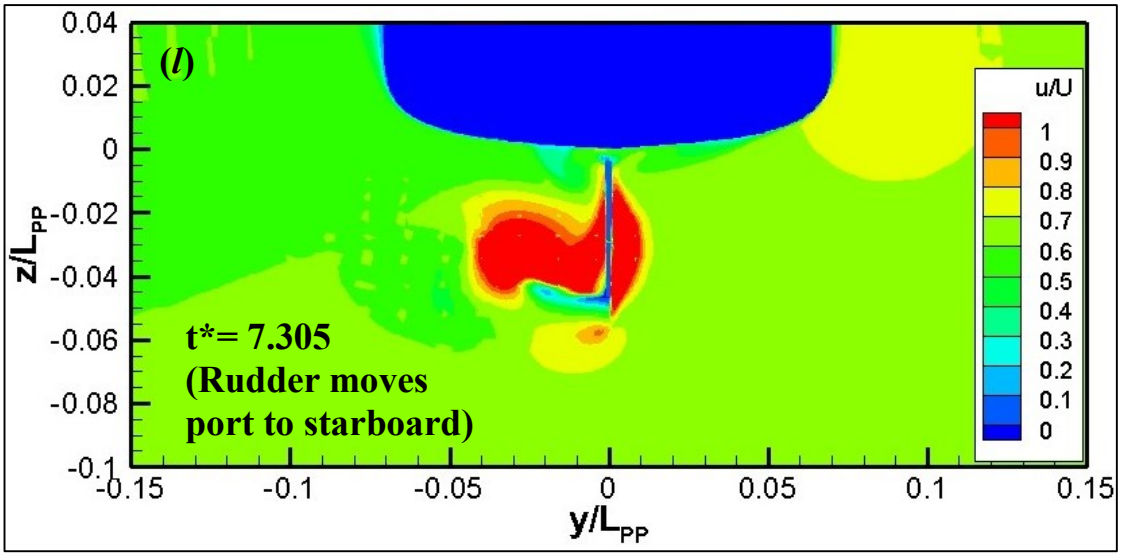
(l)
t*= 7.305
(Rudder moves
port to starboard)
u/U
1
0.9
0.8
0.7
0.6
0.5
0.4
0.3
0.2
0.1
0
z/L_PP
y/L_PP
0.04
0.02
0
-0.02
-0.04
-0.06
-0.08
-0.1
-0.15
-0.1
-0.05
0
0.05
0.1
0.15

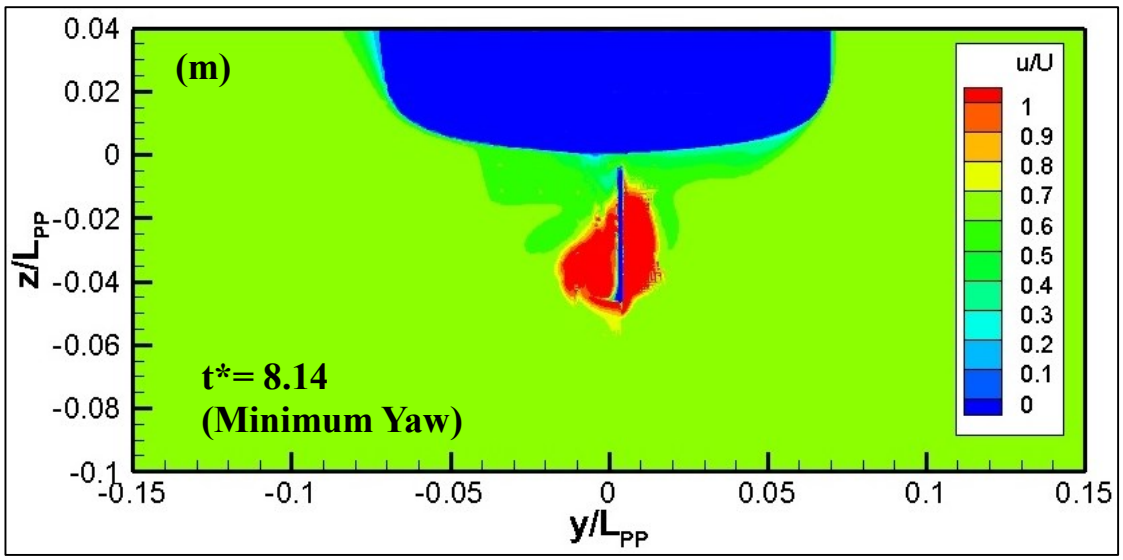
(m)
t*= 8.14
(Minimum Yaw)
u/U
1
0.9
0.8
0.7
0.6
0.5
0.4
0.3
0.2
0.1
0
z/L_PP
y/L_PP
0.04
0.02
0
-0.02
-0.04
-0.06
-0.08
-0.1
-0.15
-0.1
-0.05
0
0.05
0.1
0.15

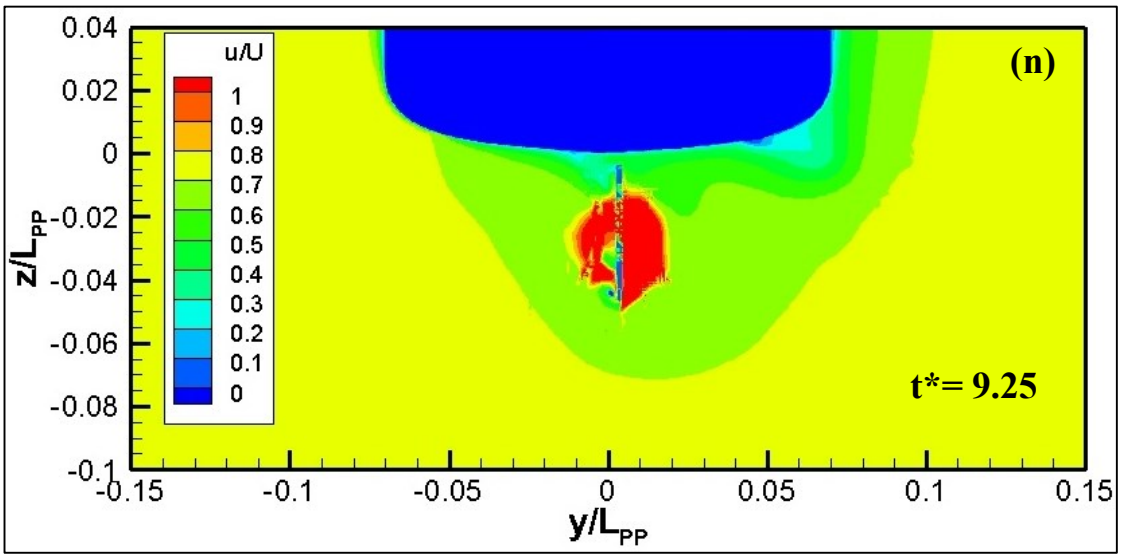
(n)
t*= 9.25
u/U
1
0.9
0.8
0.7
0.6
0.5
0.4
0.3
0.2
0.1
0
z/L_PP
y/L_PP
0.04
0.02
0
-0.02
-0.04
-0.06
-0.08
-0.1
-0.15
-0.1
-0.05
0
0.05
0.1
0.15

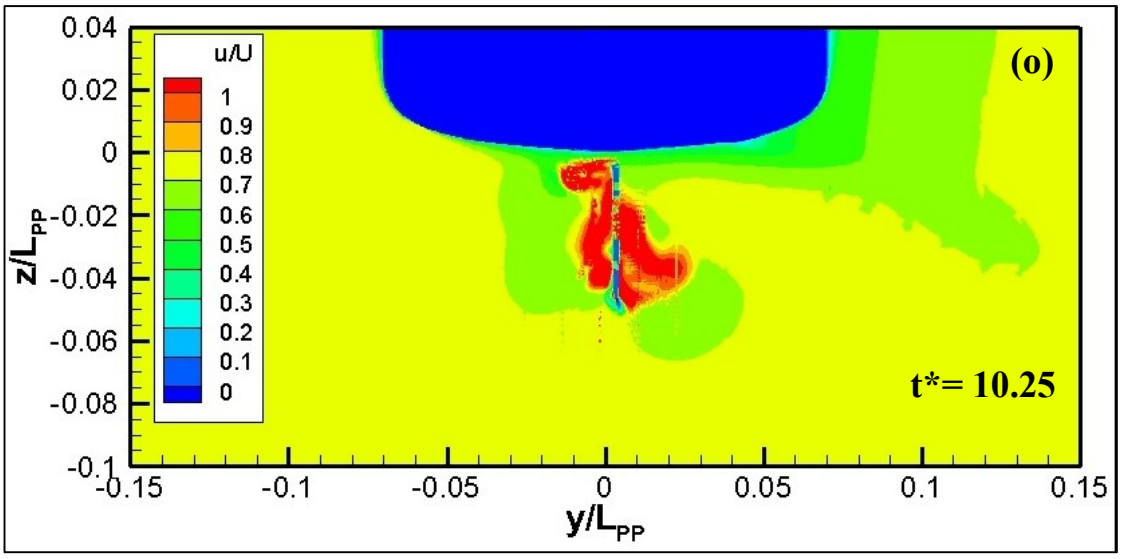
(o)
t*= 10.25
u/U
1
0.9
0.8
0.7
0.6
0.5
0.4
0.3
0.2
0.1
0
z/L_PP
y/L_PP
0.04
0.02
0
-0.02
-0.04
-0.06
-0.08
-0.1
-0.15
-0.1
-0.05
0
0.05
0.1
0.15

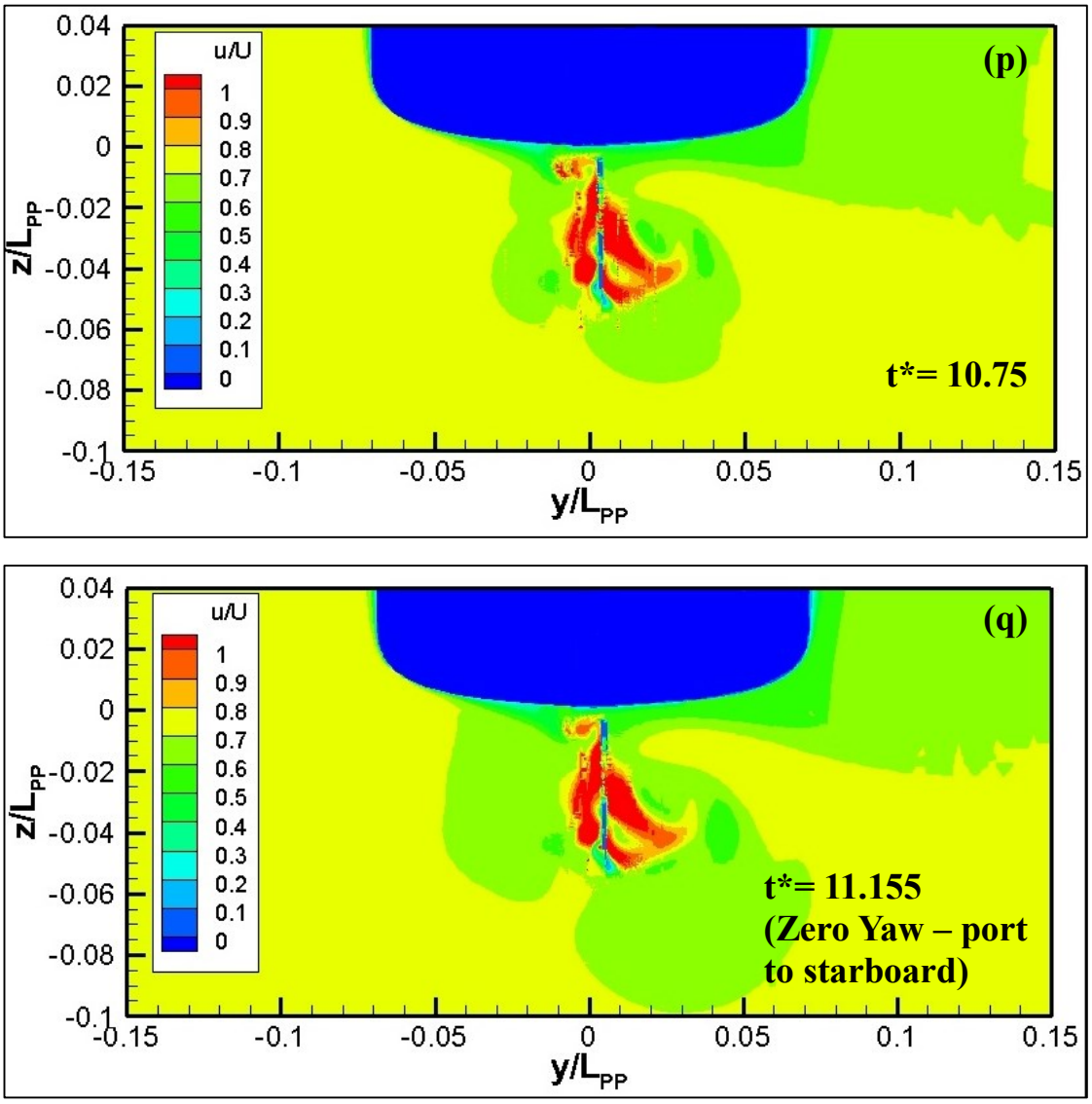

Figure 6.19. Axial Velocity Contours at *x/L*=1.01 at various time steps of 20°/20° maneuver.

As evident from the figures above, the hull-propeller-rudder region is highly turbulent. The turbulence is initially produced by the ship's boundary layer and at the aft aggravated by the propeller action followed by the rudder angle deflection. Though the results were promising in understanding the complex flow, yet higher grid resolution is required to produce more detailed flow field capable of resolving the turbulence of different scales.

CHAPTER 7

MANEUVERING IN HEAD WAVES

7.1. COURSE-KEEPING IN WAVES

Free-running, self-propulsion (model point) simulation under course-keeping control in head waves was the next case. Four head wave conditions were chosen for the study: λ/L=0.65, 1.00, 1.15, and 1.37. The specific wavelengths (λ/L=0.65, 1.15, and 1.37) were chosen since the OU S-PIV measurement data were available for those wavelengths alone. The time evolution for ship motions, 1st harmonic based on the unsteady time series, and flow visualizations were compared with the experimental data.

There exist two approaches in studying the self-propulsion characteristics in waves, namely, the speed loss method and the added powering method. In the speed loss approach, the propeller rotational speed (RPS) obtained in calm water is adopted in waves. This leads to speed loss as the RPS is not sufficient in wave conditions due to added resistance. In the added powering approach, however, the target Fn is maintained constant across calm water and waves. The presence of added resistance in waves generates added powering requirements to maintain the same target speed. Naturally, the RPS in waves is higher than in calm water. In the present simulations, the latter approach was adopted to mimic the experiments conducted at IIHR. Estimation of the propeller revolution in waves was crucial to maintain the target ship speed.

In CFD, the propeller revolutions were computed using the PID control (Equation 5.4) in free-running condition for each wavelength. Hereon, this simulated case is referred to as OU-CFD (PID). Once the propeller revolutions were found, it was fixed to simulate another set of computations of course-keeping control in waves. This was similar to the experimental technique. Hereon this set of simulated cases is referred to as OU-CFD (fixed rps). In this study, grid systems G1 and G2 were used to simulate the OU-CFD (PID) case and only grid system G2 was used to simulate the OU-CFD (fixed rps) case. To achieve the target advancing angle, the rudder was activated with the 'heading' controller (Equation 5.5) following the same PID gains as used for calm water.

7.1.1. *Time Histories*

The time evolution of 6DOF motions, controls, thrust, and torque for λ/L=0.65, 1.00, 1.15, and 1.37 were compared between IIHR-EFD, OU-CFD (PID), and OU-CFD (fixed rps), as shown in Figures 7.1, 7.2, 7.3, and 7.4 respectively. The dimensional parameters were plotted against the ratio of time to the encounter period (t/Te). Te was the non-dimensional wave encounter period corresponding to λ/L. Te for λ/L=0.65, 1.00, 1.15 and 1.37 was 0.2905, 0.3946, 0.4347 and 0.49 respectively. The peak of the incident wave was positioned at t/Te=0.

(a) Propeller Rotational Speed

In experiments, the propeller revolutions are computed for 2DOF motions and then adjusted incrementally for 6DOF motions. This demands multiple runs to locate the self-propulsion point for target Fn. Owing to limited computational resources, in this study the self-propulsion simulation was performed with course-keeping controls. To maintain the target Fn, the propeller revolution was allowed to vary according to the 'cruise' controller. From Figure 7.1- 7.4, periodicity was observed in the propeller revolution for OU-CFD (PID) (both grid systems). The predicted averaged propeller revolution speed in OU-CFD (PID) for both grid systems is listed in Table 7.1. OU-CFD (fixed rps) using G2 was simulated with propeller revolution fixed at the listed propeller revolution speed in Table 7.1. Across all the wavelengths, the E%D for both the grid systems was around 7% (E%D in calm water was <5%). Considering the complexity of the simulation, the error was within acceptable limits.

Periodicity was achieved in the propeller revolution prediction for OU-CFD (PID) for G1 and G2. However, the waveform was saw-toothed. As in most studies on waves, the propeller revolution is kept constant. The thrust and torque however fluctuate due to loading changes. In this study, as the propeller revolution was varying with time, the effect of the thrust and torque fluctuation on the propeller revolution was seen. Also, the inflow to the propeller planes changed in a short time causing the RPS peak to be more pronounced.

A small disturbance was noticed in the waveform at λ/L=1.15 for G2. This could be attributed to the reflections being generated into the solution at certain time frames owing to its adopted boundary condition. A similar fluctuation was also observed with G1 λ/L=1.00. The reasons of which are still are under investigation.

The ship speed was computed accurately. All the wavelengths showed fluctuations in ship speed. However, the experiments showed no fluctuations. Similar findings were also reported in [42].

Table 7.1 Comparison of propeller revolution in varying wavelengths

Parameter	λ/L	IIHR-EFD (D)	OU-CFD G1 (S_1)	OU-CFD G2 (S_2)	E%D (S_1)	E%D (S_2)
n_{calm}[rps]	-	18.69	17.84	17.91	4.55	4.17
n_{waves}[rps]	0.65	19.5	18.26	18.00	6.36	7.69
	1.00	22.0	20.39	-	7.32	-
	1.15	23.0	21.32	21.30	7.30	7.39
	1.37	23.0	21.26	21.60	7.57	6.09

(b) Motions

In Figure 7.1-7.4, the amplitude of the incident wave, 2DOF motions (heave and pitch) showed a good agreement with the EFD data. Although, a slight shift in phase was observed in all the wavelengths except λ/L=1.37. For an accurate comparison, the wave crest or trough was required to be captured at the exact time and place in the computations. The difference could be attributed to temporal and spatial discretization. The time step number (Ne) given by Te/Δt required to be an integral number but the same was not possible to achieve in computations due to the adopted time step. Thus, an approximation was made. A similar situation was also observed in spatial discretization as integral grid number per wavelength and amplitude was difficult to achieve, especially around a curvilinear grid. A combination of the above reasons culminated in the phase difference. As the added resistance in short wave (λ/L=0.65) was small and mainly attributed to wave reflection at the bow, the magnitude of pitch, roll, and heave motion was small (see Figure 7.1). Compared to λ/L=0.65, it was observed that the amplitude of vertical motions (heave and pitch) was larger in the longer wave. The added resistance in the longer wave is mainly attributed to the ship's vertical motions. Deviation of the roll angle was observed again, with similar reasons to calm water.

(c) Thrust and Torque

The thrust and torque waveforms were similar to propeller revolutions. It was noted that the predicted thrust was smaller when the propeller rotation speed was fixed [OU-CFD

(fixed rps) case] than when the propeller speed was varied [OU-CFD (PID) case] in all wavelengths. The fluctuation was closer to the EFD result.

(d) Neutral Rudder Angle

For the course-keeping study, rudder control was activated. On comparing rudder angle prediction, in Figures 7.1 and 7.2, it was observed that the rudder in the computation moved opposite to the EFD but the periodicity was similar. The deviation of the computed rudder angle was higher with G1 compared to G2. Similar findings were also reported in the calm water study in Chapter 6. The required rudder angle to maintain a straight course is small and to capture the small changes in the rudder angle, sufficient grid points are required. In the case of G1, an insufficient number of grids at the stern and the adopted fixed hub were the probable causes for the deviation. However, for G2, the absence of rudder stock played a major role. As shown in Sanada *et al.* [20], the fixed rudder stock was the major contributor to the total negative yaw moment due to the larger angle of attack at its leading edge. In its absence, the total negative yaw moment responsible for the rudder to turn starboard reduces. This effect is more pronounced in waves. Additionally, the fixed hub weakens the hub vortex. Thus, the influence of the hub vortex on the rudder action was not accurately captured. The combined effects culminated in the opposite rudder deflection. However, the trajectory matched well with the experiment for both the grid systems and a straight-ahead course was achieved. The ship's yaw angle in computations was closer to the desired target heading angle of zero degrees whereas the yaw angle in experiments was higher.

For the rudder angle comparison in Figure 7.3 (λ/L=1.15), it was observed that the waveforms of CFD using G2 and EFD were similar. A phase shift in the neutral rudder angle was observed for CFD predictions. Computations with G1, however, showed underestimations in the rudder angle predictions. The trajectory matched well with the experiment and a straight-ahead course was achieved.

Similar to other wavelengths, computations with G1 under-predicted the neutral rudder angle. However, the waveforms were similar to the experiments. Course-keeping was more challenging in λ/L=1.37 using G2. The peaks of the rudder angle (see Figure 7.4) coincided with each other but the waveforms were dissimilar. This could be attributed to the difference in rudder shape between CFD and EFD, and the number of grids near the stern was

insufficient. A straight-ahead course was achieved in computations, similar to the experiments with a better heading angle.

7.1.2. *Harmonic Analysis*

Using Fourier analysis on the unsteady time histories of course-keeping simulations in waves, the 0th and 1st harmonic amplitudes of any arbitrary parameter were determined. The Fourier series in its amplitude-phase form is described in Equation 7.1.

$$F(t) = \frac{a_0}{2} + \sum_{n=1}^{N} F_n \cos\left(2\pi n f_e t + \gamma_n\right) \tag{7.1}$$

where, F_n is defined as follows:

$$\begin{aligned} a_n &= \frac{2}{T}\int_0^T f(t)\cos\left(2\pi n f_e t\right)dt \\ b_n &= \frac{2}{T}\int_0^T f(t)\sin\left(2\pi n f_e t\right)dt \\ F_n &= \sqrt{a_n^2 + b_n^2} \\ \gamma_n &= \tan^{-1}\left(-\frac{b_n}{a_n}\right) \end{aligned} \tag{7.2}$$

where, a_n and b_n are the Fourier coefficients of $F(t)$, F_n and γ_n are the nth harmonic amplitude and its corresponding phase respectively and f_e (determined using Equation 7.3) is the wave encounter frequency.

$$\begin{aligned} f_e &= \frac{\omega_e}{2\pi} \\ \omega_e &= \sqrt{kg} + kU\cos(\chi) \\ k &= \frac{2\pi}{\lambda} \end{aligned} \tag{7.3}$$

where, ω_e is the wave encounter frequency (rad/s), g is the acceleration due to gravity, k is wave number and U is steady-state ship velocity.

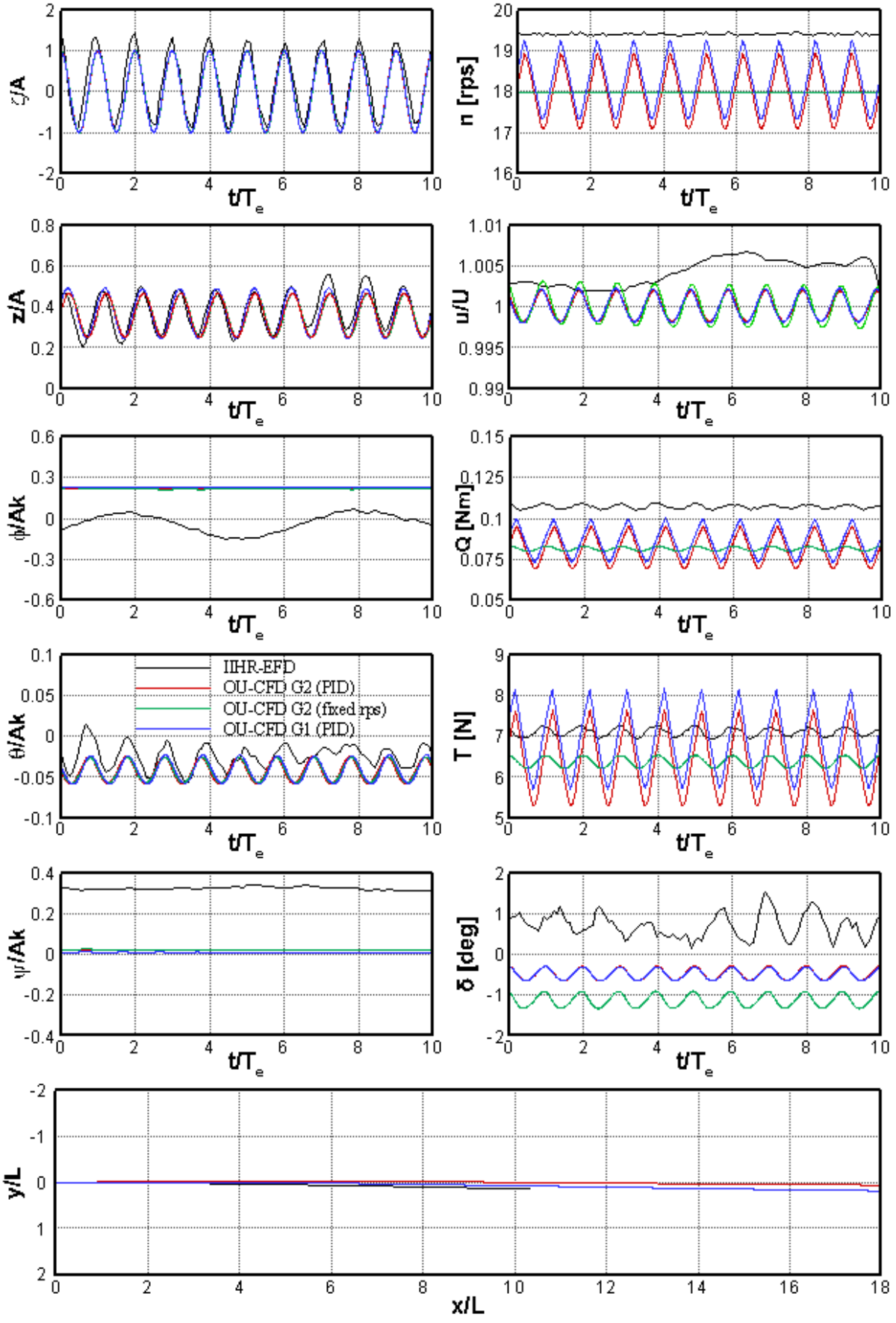

Figure 7.1 Time history comparison for course-keeping simulation at λ/L=0.65.

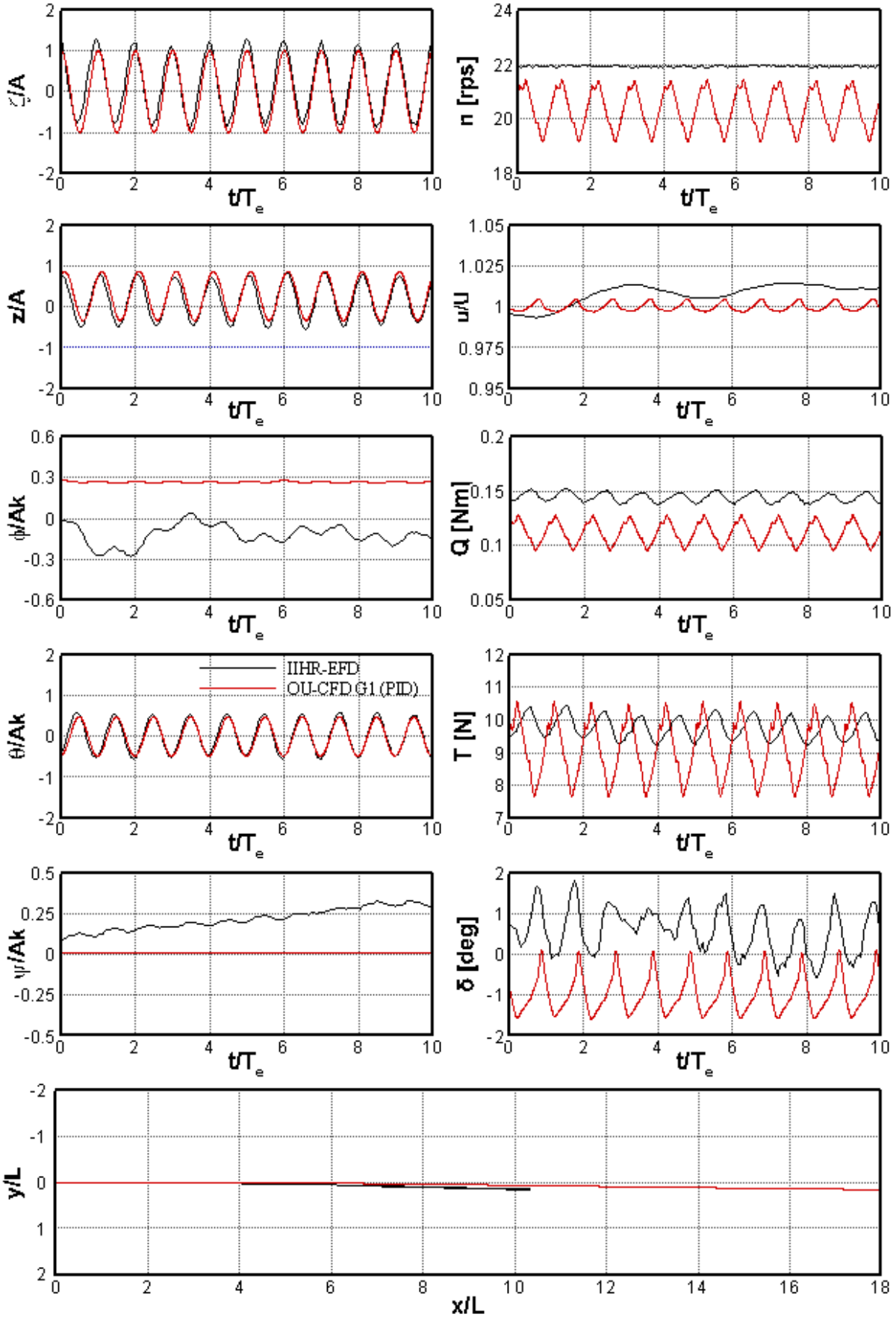

Figure 7.2 Time history comparison for course-keeping simulation at λ/L=1.00.

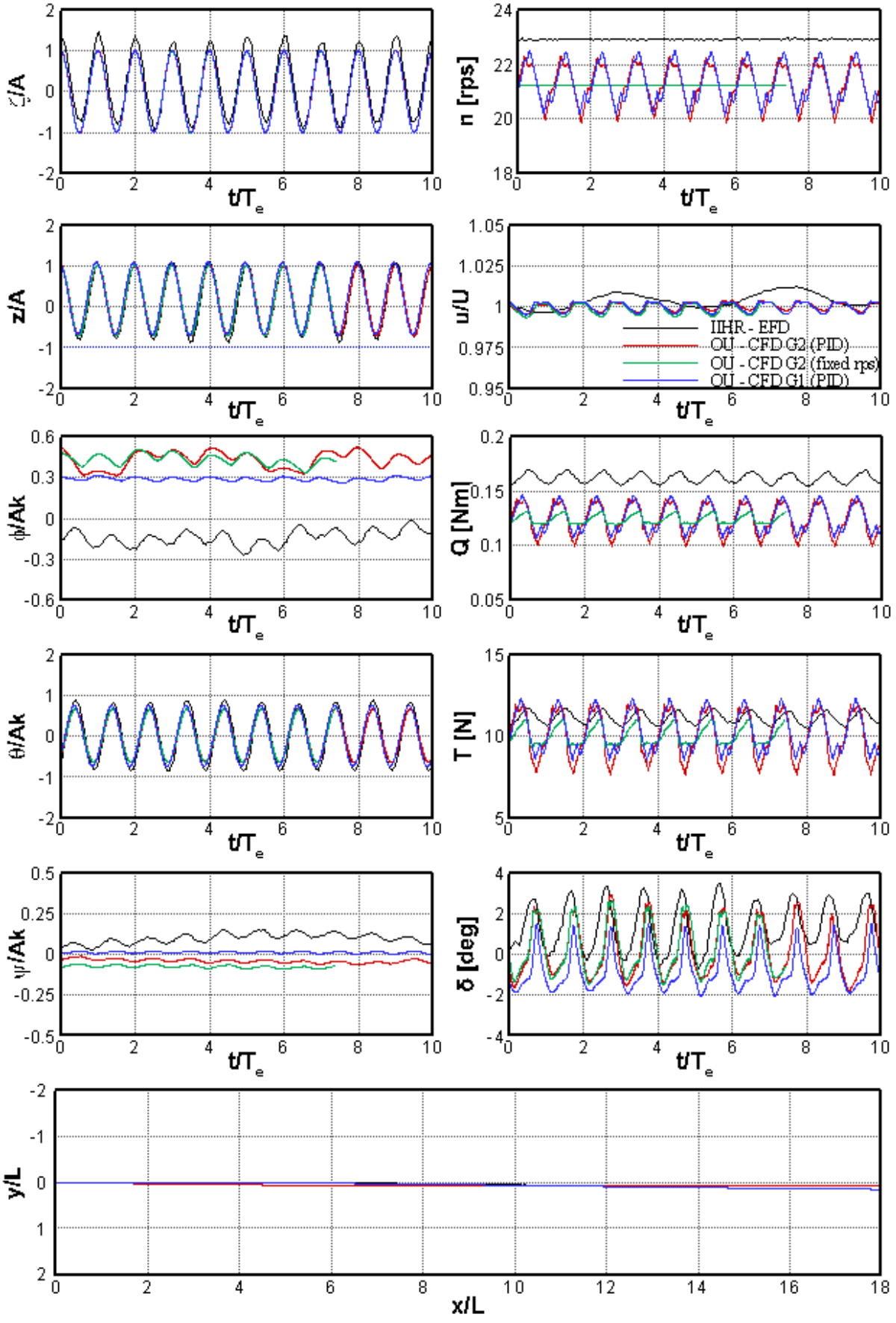

Figure 7.3 Time history comparison for course-keeping simulation at λ/L=1.15.

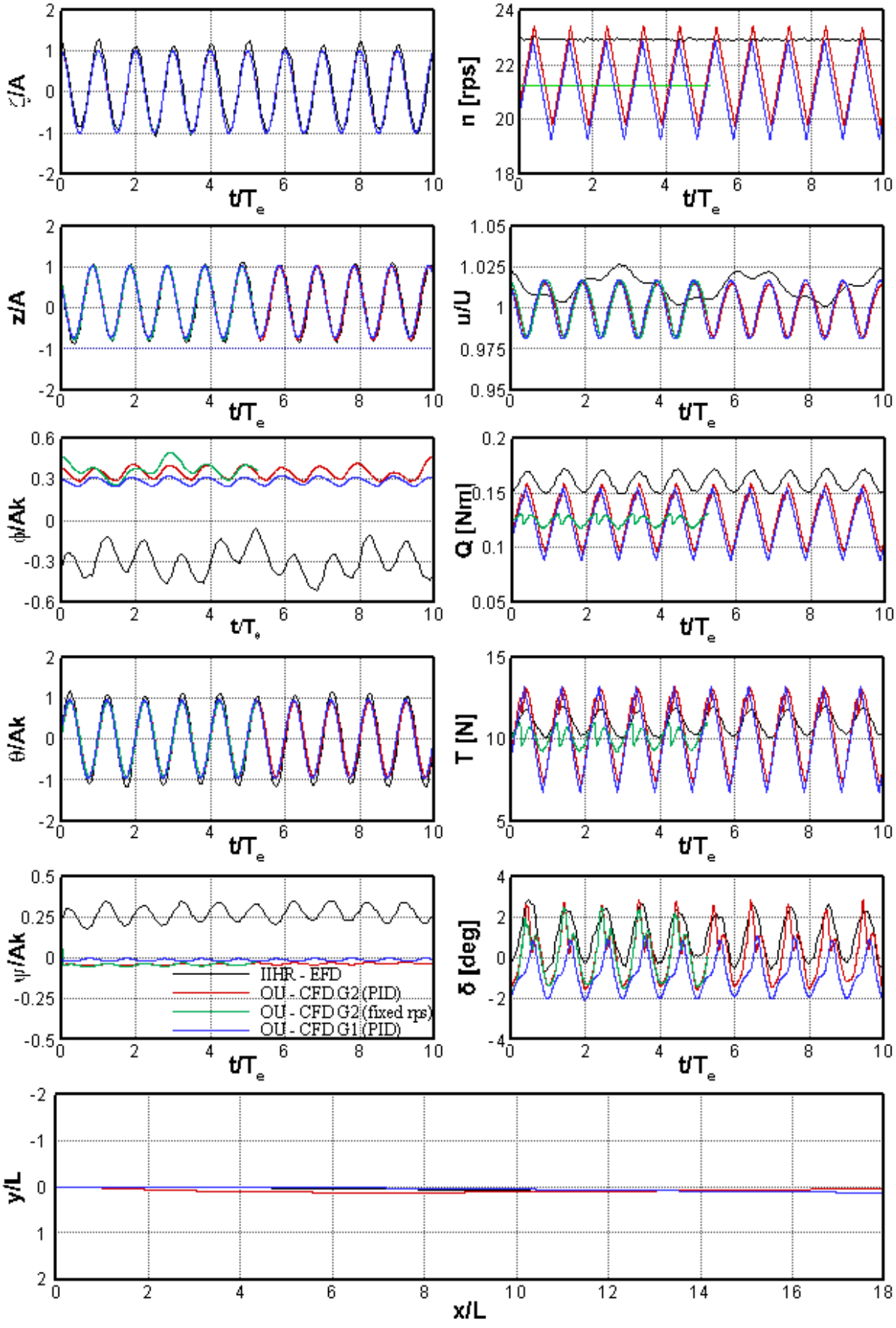

Figure 7.4 Time history comparison for course-keeping simulation at λ/L=1.37.

The computed harmonics from the unsteady time series were compared with experimental results received from several institutes:

OU-Osaka University (Japan) uses a 3.2m model for surge-free tests.

FORCE-Force Technology (Denmark) uses a 6.07m model for captive tests.

IIHR-The University of Iowa (USA) uses 2.7m for free-running tests.

Figure 7.5 shows the comparison of CFD and EFD results of non-dimensional zeroth and first harmonic amplitude of heave and pitch in head waves. The results were non-dimensionalised using A and k. CFD predicted the trend well for 0th and 1st harmonic of heave and pitch. The zeroth harmonic of heave showed a similar trend as was reported in [26, 42]. In the case of zeroth harmonic of pitch, the added resistance tests of OU and FORCE show a much larger magnitude compared to the course-keeping experiments of IIHR, The Univeristy of Iowa. CFD followed the trend of course-keeping experiments in zeroth harmonic of pitch motions. A slight over-prediction was observed for the 0th harmonic of pitch motion at λ/L=1.37. However, with grid system G1, an obvious under prediction of zeroth harmonic of heave is observed at λ/L= 1.00 and 1.15.

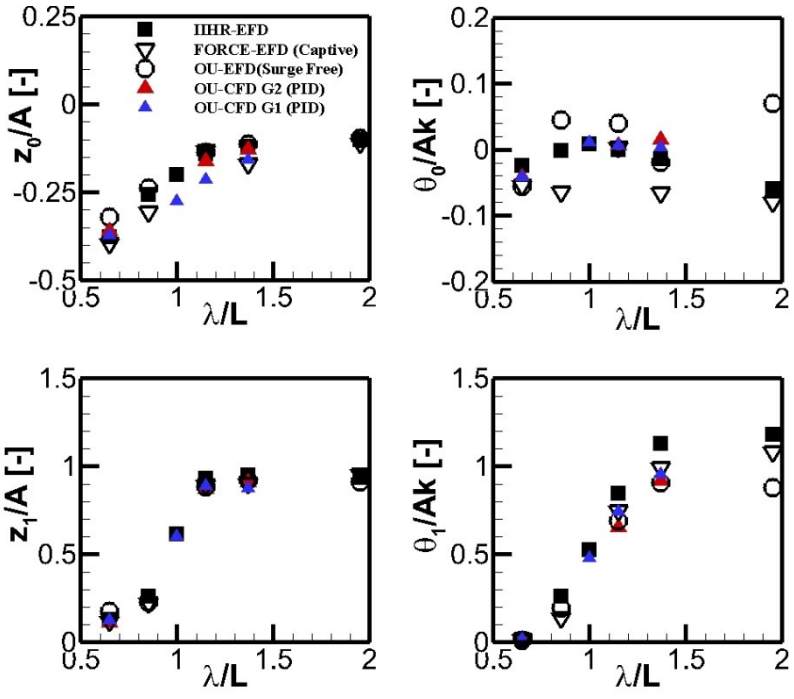

Figure 7.5: Harmonic amplitude of heave and pitch in head waves with varying λ/L

In 1st harmonic of pitch and heave motion, the added resistance tests of OU and FORCE and course-keeping experiment of IIHR, The University of Iowa follow the same

trend. The resonance condition at λ/L=1.15 for 1st harmonic was predicted satisfactorily. In short waves, ship motions (z/A and θ/Ak) were very small and nearly zero. With the increase of λ/L, both z/A and θ/Ak increased to around 1. In longer wavelengths, the ship moved vertically as wave amplitude and pitched as wave slope, establishing the fact that ship motions relative to the incident wave were small. The averaged error percentage over the wavelengths for 1st harmonic of heave and pitch motion for grid G1 was around 4%. In the case of grid system G2, however, the error percentage for 1st harmonic of heave and pitch motion was around 10%. As reported in [42], the error percentage for 1st harmonic of heave motion using the BF model and fully discretized propeller (DP) was 29% and 14% respectively. However, for the 1st harmonic of pitch motion, the reported error percentage was 13% and 6% for the BF propeller and fully discretized propeller (DP) respectively.

The propulsive performance was further analysed by comparing the predicted propulsion coefficients, as shown in Figure 7.6. The thrust (K_T) and torque coefficients (K_Q) are given by Equation 5.6. The trends of K_T and K_Q predicted by CFD matched well with the experimental results. Both the coefficients were larger than the calm water due to the added resistance. The resonance condition at λ/L=1.15 was again reflected in the zeroth harmonic of thrust and torque coefficient. The slope of the zeroth harmonic of K_T and K_Q is steeper in the short waves than in the long waves. The error percentage of zeroth harmonic of thrust and torque coefficient was around 9% for grid system G1. Grid system G2 reported 5.5% and 10.2% error for zeroth harmonic of K_T and K_Q. In the case of the 1st harmonic of both coefficients, however, the percentage errors were very high. This could be attributed to the fluctuating propeller revolutions permitted in the CFD case but fixed in the EFD case.

Figure 7.7 shows the comparison of CFD and EFD data of the first harmonic amplitude of yaw and rudder angle in head waves. The rudder angle was expressed in degrees whereas the heading angle was non-dimensionalised using A and k. The trends matched fairly well using grid system G2. The resonance condition was again reflected in the harmonic of the rudder angle. However, grid system G1 failed to capture the resonance condition. As was pointed in calm water studies, the grid system G1 is fairly a coarse grid compared to G2. More resolution at the stern is required to better resolve the hull-propeller-rudder interaction. For the heading angle, the values were suppressed to near zero by the rudder controller at all wavelengths for both the grid system.

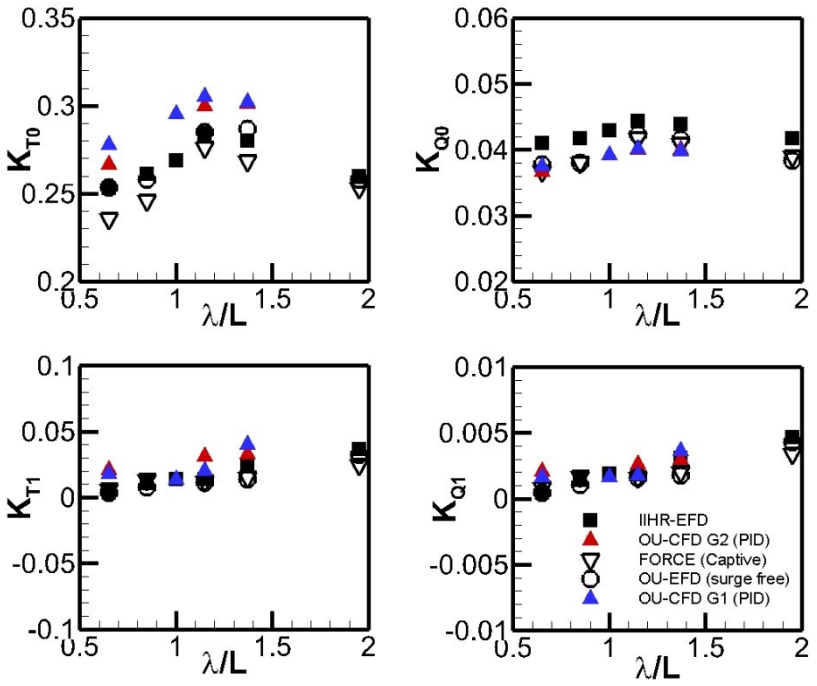

Figure 7.6: Harmonic amplitude of thrust and torque coefficients in head waves with varying λ/L

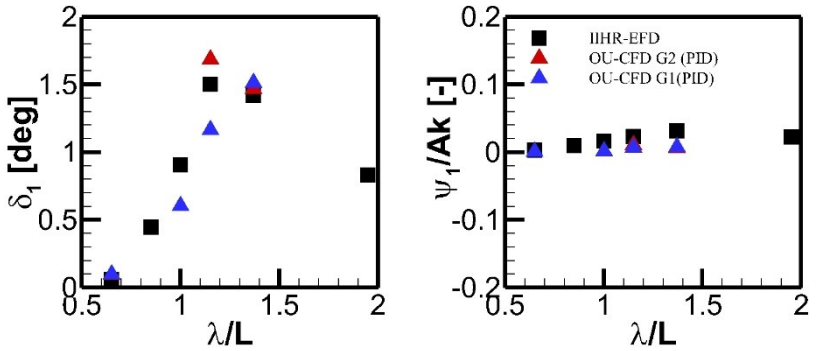

Figure 7.7: Harmonic amplitude of rudder and yaw angle in head waves with varying λ/L.

7.1.3. *Local Flow Predictions*

The local flow downstream of the rudder in grid system G2 and G1 (x/L=1.025) at λ/L=0.65, 1.15, and 1.37 was compared with OU S-PIV measurements and presented in Figures 7.8, 7.9, and 7.10 respectively. Four typical time instances in one wave period for each wavelength were chosen to analyse the hydrodynamic performance of the ship in head waves. Since the OU S-PIV measurements were conducted in carriage coordinate, large motion responses were reflected in both EFD and CFD results. The flow pattern for λ/L=0.65 (see Figure 7.8) was similar to calm water due to small vertical motions, as reported earlier. As

the λ/L increased, the vertical motions increased, which led to the propeller wake move up and down (see Figures 7.9 and 7.10). Higher velocities were reported in waves compared to calm water. The CFD under-predicted the velocity magnitudes due to an insufficient number of grids near the stern. As reported earlier the phase difference between EFD and CFD was reasonably small, and the velocity profile also reflected the same.

The wave boundary condition was only applied to the inlet for grid system G2, causing reflections being generated into the solution at specific time frames. However, simulations with grid system G1 were conducted using wave boundary condition at inlet, outlet and side boundaries. This restricted any backflow/reflection to the solution with grid system G1. Additionally, the domain size was larger in grid system G1 compared to G2. Flow solution with grid system G2 reported some anomalies but no such cases were reported with grid system G1. Improvement of the overset grid topology is required in grid system G2.

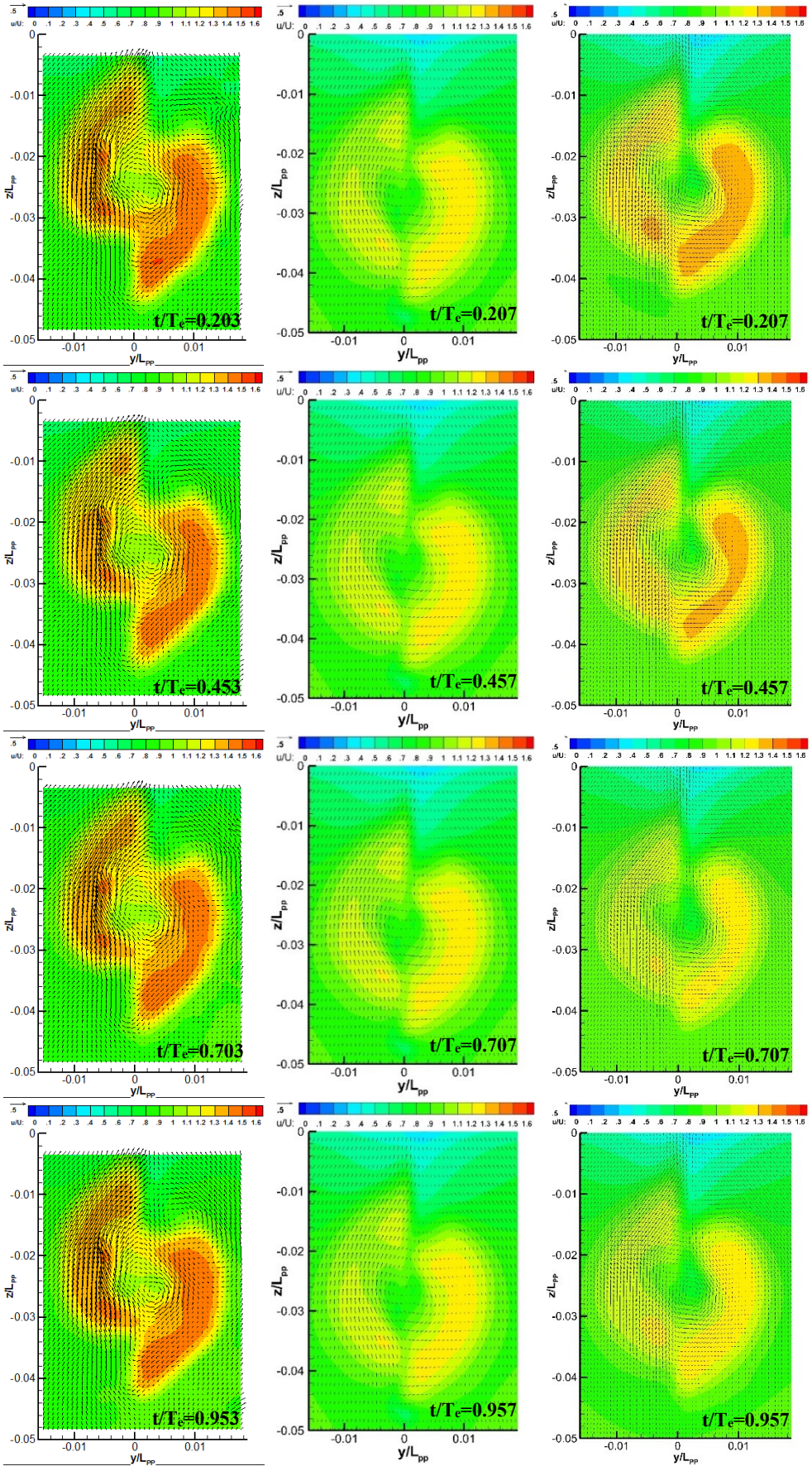

Figure 7.08: Local flow comparison behind rudder (x/L=1.025) for course-keeping simulation at λ/L=0.65 (Left) OU S-PIV (Mid) OU-CFD G2 (PID) (Right) OU-CFD G1 (PID).

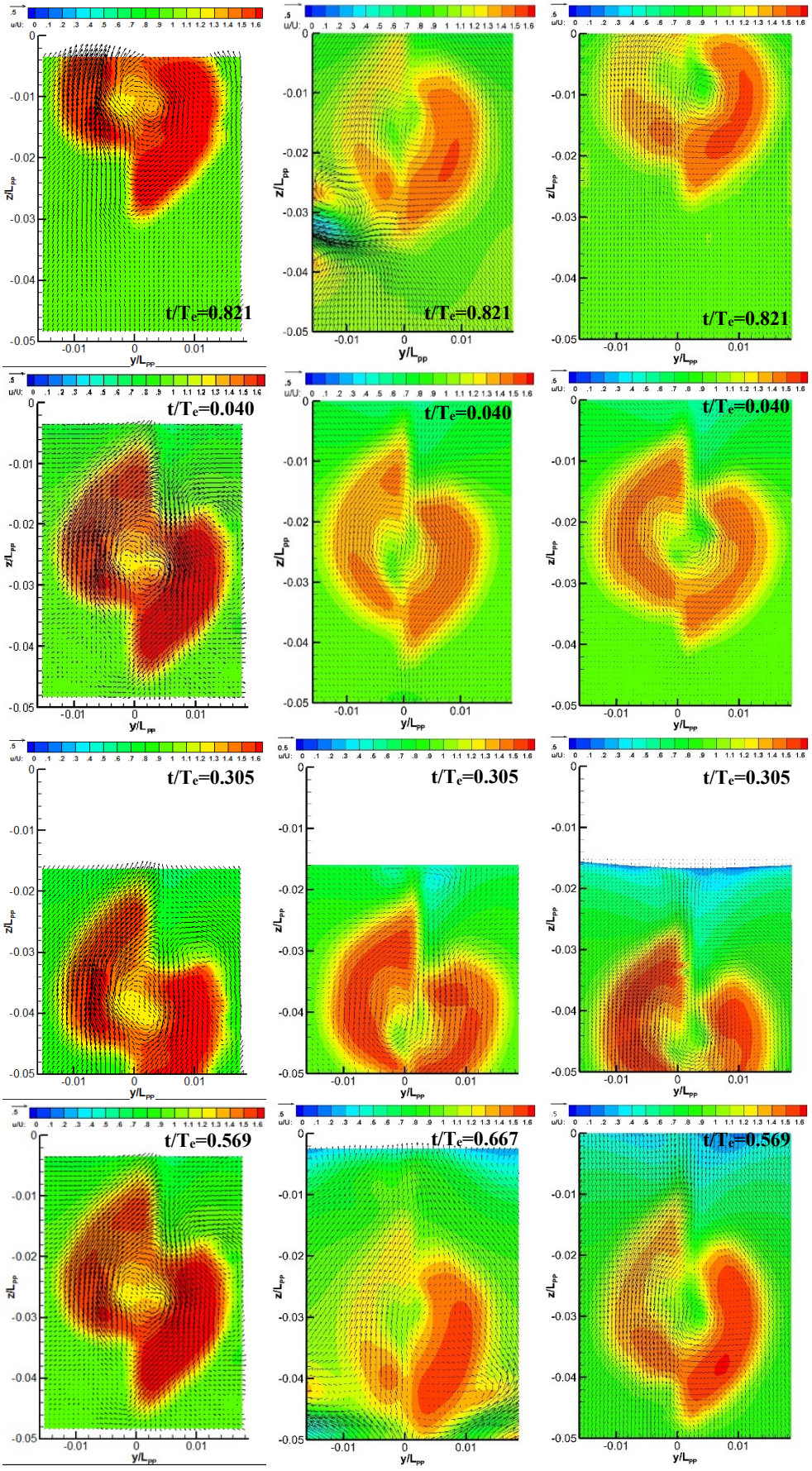

Figure 7.09: Local flow comparison behind rudder (x/L=1.025) for course-keeping simulation at λ/L=1.15. (Left) OU S-PIV (Mid) OU-CFD G2 (PID) (Right) OU-CFD G1 (PID)

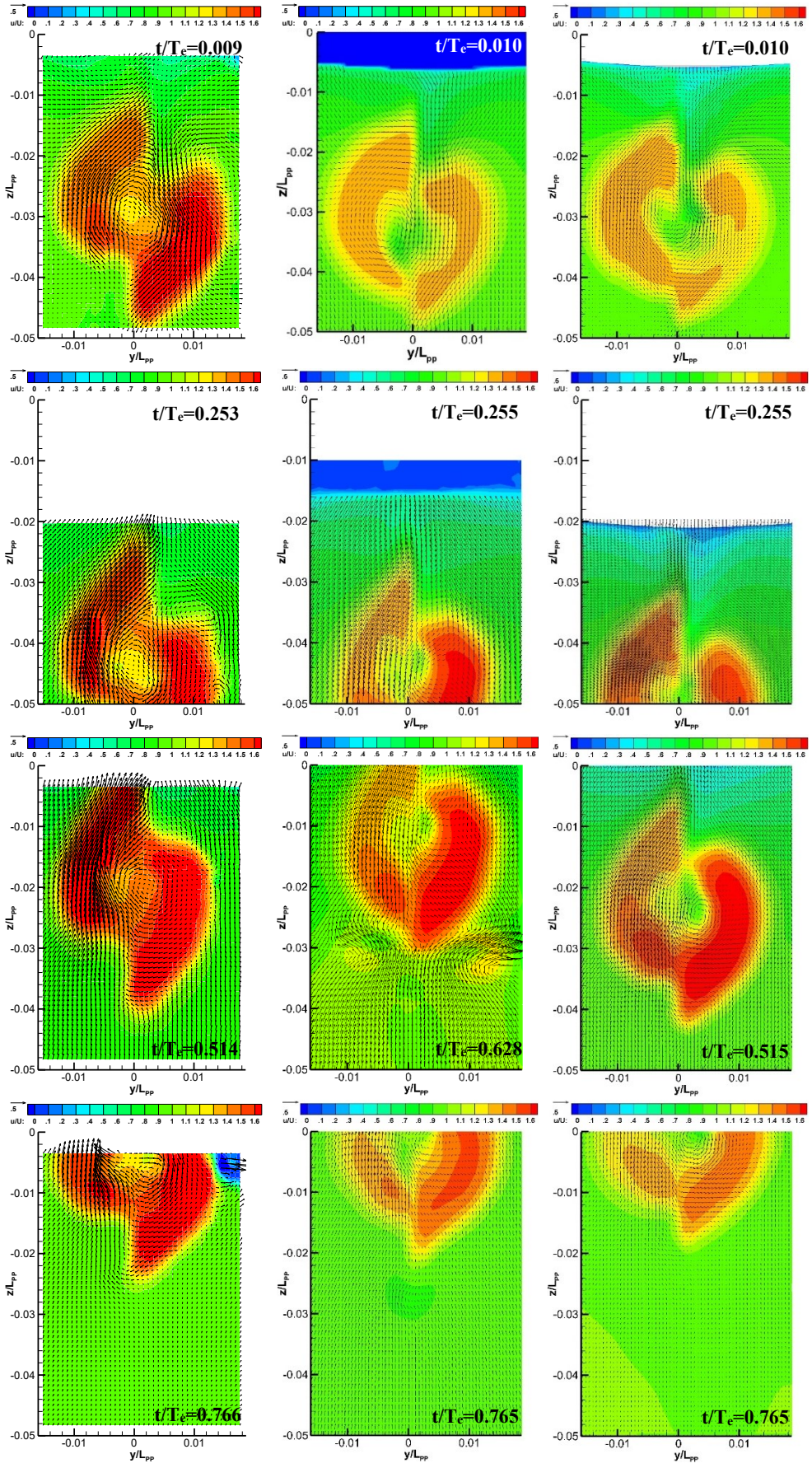

Figure 7.10: Local flow comparison behind rudder (*x/L*=1.025) for course-keeping simulation at λ/L=1.37. (Left) OU S-PIV (Mid) OU-CFD G2 (PID) (Right) OU-CFD G1 (PID)

CHAPTER 8

CONCLUSIONS

8.1. SUMMARY

The direct simulations of a free-running maneuvering ship in both unrestricted calm water and head waves, using CFDShip-IOWA V4.5 coupled with OU propeller model was studied. A fully appended KCS model with moving rudder (semi-balanced horn rudder and modified spade rudder) and Osaka University propeller model was employed for the validation study. This study was one of the first attempts to use the RANS solver coupled with the OU body force propeller model in free-running simulations with a moving rudder. 6DOF motions were solved with dynamic overset grids with parent/child hierarchy in a rough free surface environment. Feedback controllers were used on propeller revolutions and rudder angle to simulate a free-running ship under course-keeping control. The results were validated with available experimental data from various institutes to understand and regulate the possible modelling and numerical errors in the simulations. An explicit comparison with other propeller models, namely the axisymmetric body force propeller model, and fully discretized propeller, was also undertaken to understand the efficiency of the adopted propeller model. The complex hull-propeller-rudder interaction of a maneuvering ship was studied by analyzing the flow fields. Based on the aforementioned analyses, all points of findings are summarized as follows:

(a) Self-propulsion simulation with rudder controls in calm water was the first simulation case. The time evolution of motions, PID controls, and propeller forces compared well with the experimental data. The propeller rotational speed was underestimated by 4.2% and the thrust generated by the propeller was under-predicted by 2.4% with a modified spade rudder. Using a semi-balanced horn rudder, the propeller rotational speed was underestimated by 4.5% and the thrust generated by the propeller was under-predicted by 0.76%. The percentage deviation for both the rudder systems was within acceptable limits of CFD prediction capabilities found in the literature.

(b) The need for a neutral rudder angle to maintain straight-ahead course due to the difference in pressure on either side of the rudder generated by asymmetric propeller flow

was explained using the flow field measurement. The underestimation of the required neutral rudder angle could be attributed to the simplification of the rudder shape. The hull-propeller-rudder interaction was discussed and compared well with OU-PIV measurements. However, the semi-balanced horn rudder was unable to predict the same owing to a weaker resolution of the grid system.

(c) The comparison between simulations with a spade rudder and experiments was satisfactory for the zigzag ±20°/20° maneuver for motion and motion rates. Whereas for ±10°/10° the comparison match well in certain criteria and differ in others. This happens because the early fluctuations of self-propulsion simulations encroach the ±10°/10° zigzag maneuver whereas for ±20°/20° the fluctuations settle down with time. Similar observations were also made for computations using a semi-balanced hon rudder. The second overshoot for all the zigzag maneuver simulations using a semi-balanced horn rudder showed a higher error percentage compared to the first overshoot. This was caused due to the numerical dissipation brought in due to coarse grids. The study again highlighted the need for a fine grid to resolve the hull-propeller rudder interaction. Further studies are required

(d) The turning circle maneuver using modified spade rudder was under-predicted for ±35° rudder angle due to the over-prediction of the rudder force. On using a lesser rudder angle, the prediction improved. The under-prediction resulted from the simplification of rudder geometry. Using a semi-balanced horn rudder showed an over prediction of the maneuver. This was similar to other studies on maneuvering using horn rudder found in the literature.

(e) Due to the presence of horn fixed to the hull, the predicted tactical diameter using a semi-balanced horn rudder was higher compared to the spade rudder as the angle of attack to the movable rudder changes. The percentage increase of tactical diameter was 20% in portside turning and 15% in starboard turning when compared against rudder angle of 30°.

(f) Dynamic maneuvers result in complex flow especially inflow and wake of the propeller. The flow field of the zigzag 20°/20° maneuver using simplified rudder was analyzed. The evolution of the boundary layer was observed. The high-speed wake of the propeller reached the free surface further away from the low velocity of ship wake extending to the free surface. The hull-propeller-rudder region is highly turbulent. The turbulence is initially produced by the ship's boundary layer and at the aft aggravated by the propeller action followed by the rudder angle deflection. A higher grid resolution is required to produce a more detailed flow field capable of resolving the turbulence of different scales.

(g) In summary, it was highlighted that a low fidelity model (such as the OU propeller model and BF model) was capable of handling standard maneuvers, in calm water, provided the resolution of the grid near the rudder was good. Although the grid system with horn rudder used in computations was coarser compared to the grid setup used in computations with the BF model [42], the integral parameters fared well with the experiments.

(h) Free-running, self-propulsion under course-keeping control in four head wave conditions was simulated. The applicability of the approach was indicated by the good agreement of the predicted trajectory for all the cases. The amplitude of motions compared well but there existed a difference in phase due to temporal and spatial discretization. The deviation of predicted propeller revolutions from experiments was about 6-7.5%.

(i) Zeroth and First harmonics based on the unsteady time series of motions were weighed against data from various institutes. The results matched well both quantitatively and qualitatively. The resonance condition in simulations and experiments was observed at $\lambda/L=1.15$. The error percentage averaged over the wavelength for 1st harmonics heave and pitch motion using spade rudder and semi-balanced horn rudder was 10% and 4%. Fully discretized propeller and BF propeller read much higher percentage error [42].

The main conclusion of the work presented herein was that the designed CFD method (CFDShip-IOWA coupled with the OU propeller model) is capable of handling free-running ships under course-keeping simulations in calm water and waves. Due to the inherent assumptions in the OU propeller model, the method is capable of capturing the hull-propeller-rudder interaction efficiently. This approach took less time for a maneuvering simulation as opposed to the fully discretized propeller, without compromising significantly on the propeller performance. Though the general forecast of motions and other parameters was promising, comparison errors for some variables were still significant. The approach is useful in the early design stages.

8.2. FUTURE WORK

In the context of this work, the general forecast of motions was promising and quantitative values of maneuvering characteristic was reasonable. But for some quantities, comparison errors with the experimental data have not yet achieved a negligible level. The modelling errors still pose a problem requiring finer resolution at the stern. The evident complex turbulent flow of different scales in the hull-propeller-rudder region during maneuvering

requires further investigation to understand the complex flow mechanism and judge the adequacy of the RANS solver. Our perspective is to extend the potential of our method to more complex simulations such as maneuvering in waves. Verification studies would also be performed for course-keeping and maneuvering cases to better understand the dependency of the grid on the simulated results.

REFERENCES

[1] ITTC, the Manoeuvring Committee: "Final Report and Recommendations to the 25th ITTC." Proceedings of the 25th ITTC, 2008.

[2] ITTC, the Manoeuvring Committee: "Final Report and Recommendations to the 26th ITTC." Proceedings of the 26th ITTC, 2011.

[3] Kim, W.J., Van, D.H. and Kim, D.H., "Measurement of flows around modern commercial ship models," Experiments in Fluids, Vol. 31, 2001, pp.567-578.

[4] Araki, M., Sadat-Hosseini, H., Sanada, Y., Tanimoto, K., Umeda, N. and Stern, F., "Estimating maneuvering coefficients using system identification methods with experimental, system based, and CFD free running trial data," Ocean Engineering, Vol.51, 2012, pp.63–84.

[5] Sanada, Y., Tanimoto, K., Takagi, K., Gui, L., Toda, Y. and Stern, F., "Trajectories for ONR Tumblehome maneuvering in calm water and waves," Ocean Engineering, Vol.72, 2013, pp.45–65.

[6] Ohmori. T., "Finite-Volume Simulation of Flows about a Ship in Maneuvering Motion," Journal of Marine Science and Technology, 1998.

[7] Turnock, S.R., Phillips, A.B. and Furlong, M., "URANS simulations of static drift and dynamic manoeuvres of the KVLCC2 tanker," Proceedings of workshop on verification and validation of ship manoeuvring simulation methods, Denmark, 2008.

[8] Toxopeus, S., "Viscous-Flow Calculations for KVLCC2 in Deep and Shallow Water," Proceedings of the International Conference on Computational Methods in Marine Engineering, MARINE, Lisbon, Portugal, 2011.

[9] Toxopeus, S., Simonsen C.D., Guilmineau E., Visonneau, M., and Stern, F., "Viscous-Flow Calculations for KVLCC2 in Manoeuvring Motion in Deep and Shallow Water," NATO AVT-189 Specialists Meeting on Assessment of Stability and Control Prediction Methods for NATO Air and Sea Vehicles, Portsdown West, UK, 2011.

[10] Zou, L., Larsson, L. and Orych, M., "Verification and validation of CFD predictions for a manoeuvring tanker," Journal of Hydrodynamics, Vol. 22, No. 5, supplement 1, 2010, pp. 438-445.

[11] Zou, L. and Larsson, L., "A V&V Study Based on Resistance Submissions to the Gothenburg 2010 Workshop on Numerical Ship Hydrodynamics," Chapter in a book published by Springer, title: Numerical Ship Hydrodynamics – An Assessment of the Gothenburg 2010 Workshop (Eds. Larsson, L., Stern, F., and Visonneau, M.) (partly presented at 14th Numerical Towing Tank Symposium, NuTTS2011, Poole, UK), 2012.

[12] Carrica, P.M., Castro, A.M. and Stern, F., "Self-propulsion computations using a speed controller and a discretized propeller with dynamic overset grids," Journal of Marine Science Technology, Vol.15, No.2, 2010, pp.316–330.

[13] Castro A. M., Carrica, P. M. and Stern, F., "Full Scale Self-Propulsion Computations Using Discretized Propeller for The KRISO Container Ship KCS," Journal of Computers & Fluids, Vol.51, 2011, pp.35-47.

[14] Carrica, P.M., Farzad, I., Hyman, M., Bhushan, S. and Stern, F., "Turn and zigzag maneuvers of a surface combatant using a URANS approach with dynamic overset grids," Journal of Marine Science Technology, Vol.18, No.2, 2013, pp.166–181.

[15] Mofidi, A. and Carrica, P.M., "Simulations of zigzag maneuvers for a container ship with direct moving rudder and propeller," Journal of Computers and Fluids, Vol.96, 2014, pp.191-203.

[16] Shen, Z., Wan, D.C. and Carrica, P.M., "Dynamic overset grids in OpenFOAM with application to KCS self-propulsion and maneuvering," Ocean Engineering, Vol.108, 2015, pp.287–306.

[17] Wang, J., Zhao, W. and Wan, D.C., "Free Maneuvering Simulation of ONR Tumblehome Using Overset Grid Method in naoe-FOAM-SJTU Solver," Proceedings of the 31th Symposium on Naval Hydrodynamics, 11-16 Sep. 2016, Monterey, California, USA.

[18] Wang, J., Zou, L. and Wan, D.,"CFD simulations of free running ship under course-keeping control," Ocean Engineering, Vol.141, 2017, pp.450-464.

[19] Tokyo Workshop on CFD in Ship Hydrodynamics, 2015.
http://www.t2015.nmri.go.jp/kcs_gc.html

[20] Sanada, Y., Kim D.H., Sadat-Hosseini, H., Toda, Y., Simonsen, C. and Stern F., "Experiment and numerical simulations for KCS added powering in regular waves with variable heading," Proceedings of the 32nd Symposium of Naval Hydrodynamics, 5-10 Aug. 2018, Hamburg, Germany.

[21] Sanada, Y., Ito S., Toda, Y. and Stern F., "Added powering measurement of KRISO container ship maneuvering in regular variable heading waves," The 30th American Towing Tank Conference, Oct. 2017, West Bethesda, Maryland, USA.

[22] Wu, P.C., Hossain, M., Kawakami, N., Tamaki, K., Kyaw, H., Matsumoto, A. and Toda, Y., "EFD and CFD Study of Forces, Ship Motions and Flow Field for KRISO Container Ship Model in Waves," Proceedings of the 32nd Symposium of Naval Hydrodynamics, 5-10 Aug. 2018, Hamburg, Germany.

[23] Carrica, P. M., Fu, H. and Stern, F., "Computations of Self-Propulsion Free to Sink and Trim and of Motions in Head Waves of the KRISO Container Ship (KCS) Model," Applied Ocean Research, Vol.33, No. 4, 2011, pp.309-320.

[24] Simonsen, C.D., Otzen, J.F., Joncquez S. and Stern, F., "EFD and CFD for KCS Heaving and Pitching in Regular Head Waves," Journal of Marine Science and Technology, Vol.18, No. 4, 2013, pp.435-459.

[25] Sadat-Hosseini, H., Wu, P. C., Carrica, P. M., Kim, H., Toda Y. and Stern, F., "CFD V&V of added resistance of KVLCC2 with fixed and free surge conditions for short and long head waves," Journal of Ocean Engineering, Vol.59, 2013, pp.240–273.

[26] Sadat-Hosseini, H., Sanada, Y., Stocker, M., Stern, F., Toxopeus, S.L., Castiglione, T., Simonsen, C. and Otzen, J., "KCS added resistance for variable heading," Proceedings of Tokyo 2015, A Workshop on CFD in Ship Hydrodynamics, 2-4 Dec. 2015, National Maritime Research Institute (NMRI), Tokyo, Japan.

[27] Simonsen, C.D. and Stern, F.: "RANS maneuvering simulations of ESSO Osaka with rudder and a body-force propeller." *Journal of Ship research*, Vol. 49, No.2, pp. 98-120, 2005.

[27] Sadat-Hosseini, H., Wu P.C. and Stern F.,"CFD simulations of KVLCC2 maneuvering with different propeller modeling," Proceedings of the Workshop on Verification and Validation of Ship Maneuvering Simulation Methods, 2014, Lyngby, Denmark.

[28] Tokgoz, E., Win, Y.N., Kuroda, K. and Toda, Y., "A New Method to Predict the Propeller Body-force Distribution for Modeling the Propeller in Viscous CFD Code without Potential Flow Code," Proceedings of the Japan Society of Naval Architects and Ocean Engineers, Vol.19, 2014, pp.1-7.

[29] Wu, P.C., Tokgoz, E., Okawa, H. and Toda, Y., "Computational and experiment of propeller performance and flow field around self-propelled model ship in regular head waves," Proceedings of the 31st Symposium on Naval Hydrodynamics, 11-16 Sep. 2016, Monterey, California, USA.

[30] Wu, P.C., Hossain, M., Kawakami, N., Tamaki, K., Kyaw, H., Matsumoto, A. and Toda, Y., "EFD and CFD Study of Forces, Ship Motions and Flow Field for KRISO Container Ship Model in Waves," Proceedings of the 32nd Symposium of Naval Hydrodynamics, 5-10 Aug. 2018, Hamburg, Germany.

[31] Paterson, E. G., Robert V. W. and Stern, F., "General-purpose parallel unsteady RANS ship hydrodynamics code: CFDSHIP-IOWA," Technical Report, No.432, 2003, IIHR—Hydroscience & Engineering, The University of Iowa, Iowa city, Iowa, USA.

[32] Xing, T., Carrica, P. and Stern, F., "Computational towing tank procedures for single run curves of resistance and propulsion," Journal of Fluids Engineering, Vol.130, No. 10, 2008, pp.101-102.

[33] Carrica, P. M., Wilson, R. V., Noack, R., Xing, T., Kandasamy, M., Shao, J., Sakamoto, N. and Stern, F., "A Dynamic Overset, Single-Phase Level Set Approach for Viscous Ship Flows and Large Amplitude Motions and Maneuvering," Proceedings of the 26th Symposium on Naval Hydrodynamics, 17-22 Sept. 2006, Rome, Italy.

[34] Menter, F.R., "Two-Equation eddy viscosity turbulence models for engineering applications," Journal of American Institute of Aeronautics and Astronautics, Vol. 32, No.8, 1994, pp.269-289.

[35] Carrica, P. M., Wilson, R. V., and Stern, F., "An unsteady single-phase level set method for viscous free surface flows," International Journal for Numerical Methods in Fluids, Vol.53, 2006, pp.229-256.

[36] Boger, D.A., and Dreyer, J.J., "Prediction of hydrodynamic forces and moments for underwater vehicles using overset grids," Proceedings of the 44th AIAA Aerospace Sciences Meeting, AIAA paper 2006-1148, 9–12 Jan. 2006, Reno, NV, USA.

[37] Hasegawa, H., Wu, P.C. and Toda, Y., "Development of blade-rotating body force propeller model in RANS code for open water and behind-hull condition," Proceedings of the 6th World Maritime Technology Conference, 4-7 Dec., 2018, Shanghai, China.

[38] Stern, F., Kim, H.T., Zhang, D.H., Toda, Y., Kerwin, J. and Jessup, S., "Computation of viscous flow around propeller-body configurations: Series 60 CB=0.6 ship model," Journal of Ship Research, Vol.38, No.2, 1994, pp.137-157.

[39] Tokgoz, E., Wu, P.C., Okawa, H., Tamaki, K., and Toda, Y., "Computation and SPIV measurement of the flow-field around self-propelled ship in waves using body force model," Proceedings of the Japan Society of Naval Architects and Ocean Engineers, Vol.20, 2015, pp.255-258.

[40] SIMMAN Workshop, 2019.
http://www.simman2019.kr/contents/test_case_3.2.php.

[41] Pointwise, Gridgen, 2010.
http://www.pointwise.com/

[42] Kim, Dong-Hwan. "URANS V&V for KCS free running course keeping and maneuvering simulations in calm water and regular head/oblique waves." PhD (Doctor of Philosophy) thesis, University of Iowa, 2019.

[43] Weymouth, G., Wilson, R., Stern, F., "RANS CFD Predictions of Pitch and Heave Motions in Head Seas," Journal of Ship Research, Vol. 49, 2005, pp. 80-97.

[44] Noack, R.W., "Resolution Appropriate Overset Grid Assembly for Structured and Unstructured Grids." Proceedings of 16th AIAA Computational Fluid Dynamics Conference, Orlando, FL, AIAA, 2003, pp 2003- 4123.

[45] Noack, R.W., "A Direct Cut Approach for Overset Hole Cutting." Proceedings of the 18th AIAA Computational Fluid Dynamics Conference, Miami, FL, AIAA, 2007, pp 2007-3835.

[46] International Maritime Organization, "Standards for ship manoeuverability." Resolution MSC. 137(76), 2002.

LIST OF PUBLICATIONS

PAPERS:

1 RoyChoudhury, S., Kawamoto, K., Wu, PC., Sanada Y. and Toda, Y., "Course-Keeping of KRISO Container Ship in Calm Water and Head Waves", Proceedings of the 33rd Symposium on Naval Hydrodynamics, *U.S. Office of Naval Research and Osaka University* (**2021**).

2 RoyChoudhury, S., Wu, PC., Sanada Y. and Toda, Y., "Computational Fluid Dynamics study on KRISO Container Ship Maneuvering in Calm Water", Proceedings of the Twenty-ninth International Ocean and Polar Engineering Conference, ISOPE (**2019**).

CURRICULUM VITAE

EDUCATION

2018 - Present **Doctoral Course, Naval Architecture and Ocean Engineering**

Osaka University – Suita, Japan

Adviser: Prof. Yasuyuki Toda

Areas of research: Computational fluid dynamics, ship hydrodynamics.

Computational fluid dynamics study on ship maneuvering in calm water and waves

2016 - 2018 **Master of Science, Naval Architecture and Ocean Engineering**

Osaka University – Suita, Japan

Adviser: Prof. Yasuyuki Toda

2012 - 2014 **Master of Technology**

Indian Institute of Technology – Kharagpur, India

2008 - 2012 **Bachelor of Technology**

Meghnad Saha Institute of Technology – Kolkata, India

WORK EXPERIENCE

2014 – 2016 **Senior Engineer**

Forward Design Group, Mazagon Dock Limited, India

2016 **Assistant Manager**,

Forward Design Group, Mazagon Dock Shipbuilders Limited, India